Development of Density Reduced Mo-Si-B Alloys

Dissertation

zur Erlangung des akademischen Grades

Doktoringenieurin

(Dr.-Ing.)

von M.Sc. Julia Becker

geboren am 07.12.1989 in Schönebeck (Elbe)

genehmigt durch die Fakultät für Maschinenbau

der Otto-von-Guericke-Universität Magdeburg

Gutachter:

Prof. Dr.-Ing. habil. Manja Krüger

Prof. Dr.-Ing. Birgit Skrotzki

Promotionskolloquium am 18.12.2019

Kurzfassung

Hinsichtlich der Schonung von Ressourcen und der Verringerung von Umweltbelastungen ist die Steigerung des Wirkungsgrades von Turbinen im Kraftwerks- und Triebwerksbereich ein an Bedeutung zunehmender Forschungsschwerpunkt. Insbesondere ternäre Mo-Si-B-Legierungen, deren Mikrostruktur aus einer kontinuierlichen Mo-Mischkristallmatrix mit homogen verteilten intermetallischen Phasen (Mo_3Si und Mo_5SiB_2) bestehen, bieten eine ausgewogene Kombination der Hoch- und Raumtemperatureigenschaften. Jedoch stellt die verhältnismäßig hohe Dichte ($> 9 \frac{g}{cm^3}$) dieser Legierungsklasse einen entscheidenden Nachteil bei der Verwendung als Turbinenschaufel dar. Mit dem Ziel der Dichteoptimierung beschäftigt sich diese Arbeit mit Vanadium als potentiellen Legierungspartner in Mo-basierten Legierungen. Um zunächst den Beitrag von V auf die Mo-Mischkristallphase zu ermitteln, wurden Mo-5X ($X = Ti, V, Zr$) Legierungen hergestellt und mittels RT-Mikrohärtemessungen, Dreipunktbiege- sowie Druckversuchen (bis $1100\,°C$) bewertet. Zusätzlich konnten quantitative Werte für die Mischkristallverfestigung nach dem Ansatz von Labusch angegeben werden. Die Untersuchungen der binären Systeme bestätigten, dass Vanadium im Vergleich zu Titan und Zirkonium ein wettbewerbsfähiger Legierungspartner ist, da es sich positiv auf die Festigkeit und Duktilität von Mo-basislegierungen auswirkt. Darauf aufbauend wurden potentielle Mo-V-Si-B Materialien untersucht, die eine um bis zu $20\,\%$ reduzierte Dichte im Vergleich zur Referenzlegierung Mo-9Si-8B aufwiesen. Zunächst wurden mechanisch legierte und wärmebehandelte Mo-XV-9Si-8B ($X = Ti, V, Zr$) Pulver hergestellt, um die Löslichkeit von Vanadium in den beteiligten Phasen zu untersuchen. XRD Messungen zeigten, dass sich Vanadium in allen drei Phasen, dem Mo-Mischkristall sowie den intermetallischen Phasen Mo_3Si und Mo_5SiB_2 löst. Über eine Verfeinerung mittels Rietveld konnte eine Besetzungspräferenz von V innerhalb der T2 Phase beobachtet werden. Mit Hilfe von Rechnungen nach der Dichtefunktionaltheorie konnte eine Erklärung für dieses Phänomen formuliert werden. Eine Bestimmung der thermomechanischen Eigenschaften erfolgte schließlich an gesinterten (FAST) sowie lichtbogengeschmolzenen (Arc) Proben der Legierungszusammensetzung Mo-40V-9Si-8B. Dreipunktbiegeversuche an gekerbten Proben sowie Druckkriechversuche zeigten eine hohe Bruchzähigkeit und akzeptable Kriechfestigkeit dieses neuartigen Legierungssystems. Darüber hinaus wurde der Einfluss kleinerer Zugaben von Fe auf die Oxidationsbeständigkeit durch zyklische Oxidationstests untersucht.

Abstract

Improving the efficiency of turbines for power plants and aircraft engines is an increasingly important research subject. Ternary Mo-Si-B alloys, consisting of a molybdenum solid solution (Mo_{ss}) phase and two intermetallic phases Mo_5SiB_2 (T2) and Mo_3Si, are able to combine balanced room temperature fracture toughness, high temperature creep strength and good oxidation performance. However, the high density ($> 9 \, \frac{g}{cm^3}$) of this class of alloys is a drawback when used as a turbine blade material. Therefore, the present thesis deals with vanadium as a potential alloying partner for density optimized Mo-based alloys. In order to identify the role of vanadium in terms of strengthening the solid solution phase, different Mo-5X ($X = Ti, V, Zr$) alloys were produced via arc melting and evaluated by means of RT microhardness measurements, three-point bending as well as compression tests up to elevated temperatures (1100 °C). Additionally, quantitative values for solid solution hardening were determined by the approach of Labusch. Those initial characterization of the binary systems confirmed vanadium to be a competitive alloying partner compared with Ti and Zr, due to its positive effect on the strength and the ductility of Mo-based alloys at the same time. In a next step, potential Mo-V-Si-B materials which provide a reduced density by about 20 % as compared with the reference alloy Mo-9Si-8B were investigated. Different alloy compositions Mo-XV-Si-8B ($X = 10, 20, 30, 40$ at.%) were produced by powder metallurgy, including mechanically alloying and a thermal treatment, to observe the effects of V as a solute in the respective phases. X-ray diffraction showed that V can entirely be solved in the Mo_{ss} phase as well as in the Mo_3Si and Mo_5SiB_2 phases. From Rietveld refinements the preferred V sites in the lattices of the present phases were derived and could be explained by density functional theory calculations. The thermomechanical characterization was carried out on sintered (FAST) and arc-melted Mo-40V-9Si-8B alloys. Three point-bending with notched samples as well as compressive creep tests reveal a high fracture toughness and acceptable creep strength of this new type of alloys. Furthermore, the effect of minor additions of Fe on the oxidation resistance was investigated by cyclic oxidation tests.

Contents

Figures

Tables

Abbreviations and Symbols

Abbreviations

RT	Room temperature
HT	High temperature
BDTT	Brittle-to-ductile transition temperature
TT	Thermal treatment
GA	Gas atomization
PM	Powder metallurgy
MA	Mechanical alloying
CIP	Cold isostatic pressing
HIP	Hot isostatic pressing
FAST	Field assisted sintering technology
FIB	Focused ion beam
DS	Directional solidification
SLM	Selctive laser melting
LMD	Laser metal deposition
NBO	Non-bridging-oxygen
DC	Direct current
SEM	Scanning electron microscopy
SE	Secondary electrons
BSE	Backscattered electrons
EDM	Electrical discharge machining
Arc	Arc-melting
ICP-OES	Inductively coupled plasma optical emission spectroscopy
OPS	Oxide-polishing-suspension
EDS	Energy dispersive X-ray spectroscopy

EBSD	Electron backscatter diffraction	
XRD	X-ray diffraction analysis	
LEBM	Linear elastic fracture mechanics	
OM	Optical microscope	
DFT	Density functional theory	
SQS	Special quasirandom structures	
GPW	Gaussian plane wave method	
GGA	Generalized gradient approximation	
TB-LMTO-ASA	Tight-binding, linear muffin-tin orbitals with the atomic spheres approximation	
DOS	Density-of-states	
(I)COHP	(Integrals) Crystal orbital Hamilton population	
TM	Transition metal	
IP	Intermetallic phases	

Symbols

η_{therm}	Thermal efficiency	[-]
$T_{\mathrm{min/max}}$	Minimum or maximum temperature in combustion chamber	[°C]
R_e	Total critical stress for dislocation movement	[GPa]
T_{M}	Melting point temperature	[°C]
σ_0	Peierls stress	[GPa]
σ_{WH}	Stress for work hardening	[GPa]
σ_{SS}	Stress for solid solution hardening	[GPa]
σ_{GS}	Stress for grain size effect	[GPa]
σ_{PH}	Stress for particle hardening	[GPa]
M	Taylor factor	[-]
G	Shear modulus	[GPa]
c	Solute fraction of alloying atoms	[at.%]
ε_L	Size-/ shear modulus effect	[-]
η	Shear modulus misfit	[-]
δ	Atomic size misfit	[-]
M_{b}	Bending moment	[Nm]

l_s	Bearing distance	[mm]
σ_b	Bending stress	[MPa]
W	Section modulus	[Nm]
b_s	Sample width	[mm]
h_s	Sample height	[mm]
ε_f	Outer fiber strain	[%]
f	Measured deflection	[mm]
ε	Strain	[%]
ε_0	Time independent strain	[%]
$\dot{\varepsilon}$	Strain rate	[s^{-1}]
$\dot{\varepsilon}_\text{II}$	Secondary creep rate	[s^{-1}]
B	Constant for power-law creep	[-]
σ	Stress	[GPa]
n	Stress or creep exponent	[-]
Q	Activation energy for creep processes	$\left[\frac{\text{kJ}}{\text{mol}}\right]$
R	Ideal gas constant	$\left[\frac{\text{J}}{\text{mol K}}\right]$
T	Temperature	[°C]
m_x	Mass fraction	[-]
A_x	Atomic mass of respective element	[u]
X_x	Atomic fraction of respective element	[-]
$\bar{N}$	Number of intersections	[-]
L	Measuring length	[μm]
$\bar{N}_\text{L}$	Average number of grains per line	[-]
$\bar{d}$	Average grain size	[μm]
θ	Diffraction angle	[°]
λ	Wave length	[m]
d_hkl	Interplanar spacing	[Å]
E_F	Fermi level	[eV]
F_i	Indentation load	[N]
F_b	Bending load	[N]
A_HV	Projected indentation area	[mm^2]
d_HV	Pyramid's diagonal length	[mm]
K_I	Stress intensity factor (I - opening modus)	[MPa$\sqrt{\text{m}}$]

K_{Ic}	Critical stress intensity factor/ fracture toughness	[MPa$\sqrt{\text{m}}$]
F_{f}	Fracture load	[MN]
B	Sample width	[m]
D	Sample depth	[m]
S_1	Support span	[m]
α	Relative notch depth	[-]
Y^*	Stress intensity shape factor	[-]
a	lattice parameter	[Å]

1 Motivation and objective

"The Hotter the Engine, the Better"

John H. Perepezko [1]

This citation is the title of an article by Perepezko et al. [1] and describes in a few but precise words the aim and efforts of research on structural materials for turbine engines in the last decades. Particularly, in terms of preserving resources and reducing environmental impacts, improving the efficiency of aircraft engines or stationary gas turbines for the power generation industry is increasingly focused. The fact that materials for those applications have to withstand extreme environmental conditions is illustrated by the following example of a GP7200 engine [2] in Figure 1.1. In general this state-of-the-art aircraft engine can be separated into four main parts: the fan module, the compressor (subdivided into the low- and high-pressure compressor), the combustion chamber and the turbine (also subdivided into low- and high-pressure turbine). Depending on the particular loads of the individual engine parts, different material classes are considered. A basic overview on the alloys adapted to the technical requirements is given by Smarsly [3]. The present work specifically deals with the high-pressure turbine in which a slight increase of operating temperatures
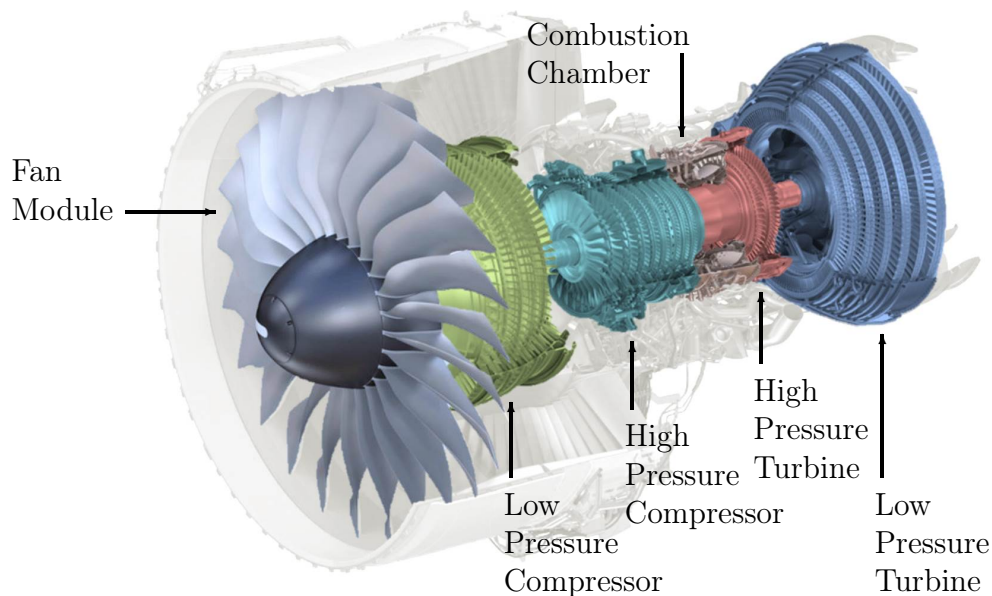
Figure 1.1: A closer look under the hood of the GP7200 engine representing its main sections [2].

would already lead to a significant improvement of the efficiency according to Equation 1.1, which represents the principle of thermal efficiency [4].

$$\eta_{\mathrm{therm}} = 1 - \frac{T_{\mathrm{min}}}{T_{\mathrm{max}}}.$$ (1.1)

Increasing the temperature in the combustion chamber (T_{max}) and thus the gas inlet temperature will lead to an efficiency gain which in turn reduces the fuel consumption. So, according to that, the high-pressure turbine blades are the most critical components, due to high thermal loading and stresses caused by temperature hot-spots and gradients between the airfoil and root. Additionally, the high pressures and mechanical stresses caused by the gas stream as well as rotational forces induce creep activation mechanisms resulting in deformation of turbine blades during their service time. Over the last 60 years, leading materials for those applications are continuously improved Ni-based superalloys [5, 6] currently used as single-crystals (Figure 1.2) in aircraft engines representing the state-of-the-art turbine blade material.

Figure 1.2 represents that commonly used Ni-based superalloys, working close to their melting point, are reaching their limits on maximum operating temperatures [1]. Therefore, despite of complex cooling systems and coatings, the turbine's efficiency cannot be substantially increased any more [7]. So it is necessary to develop new high temperature materials able to withstand higher operating temperatures going beyond the capability of state-of-the-art Ni-based superalloys. This demand for novel high-performance materials
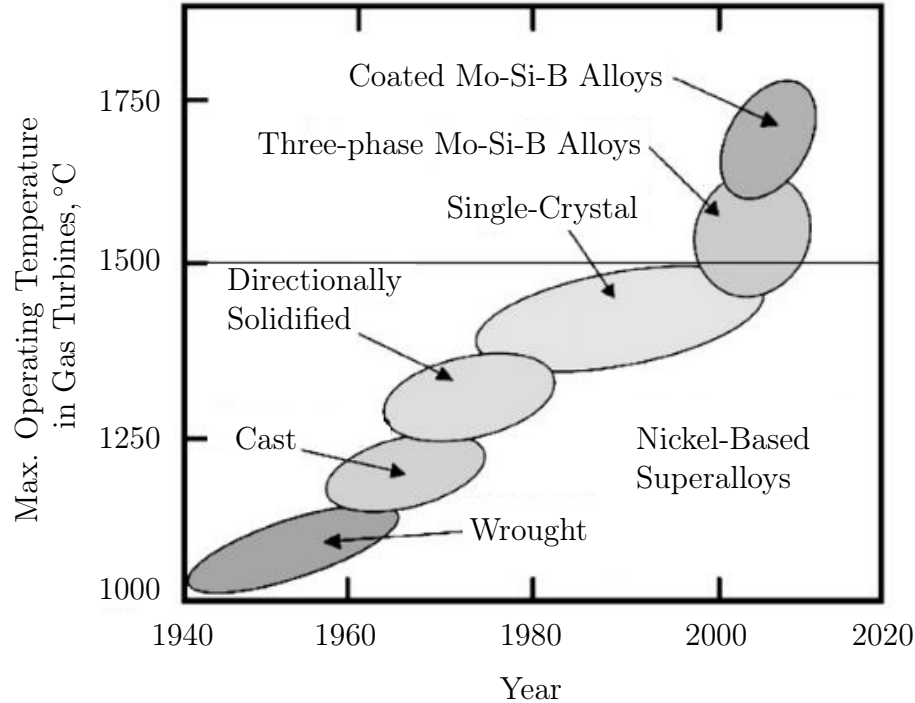
Figure 1.2: Development of turbine materials adapted for rising operating temperatures, where the application limit of Ni-based superalloys is marked by the straight line [7].

with increased melting points leads to new approaches using refractory or high-melting metal alloys, often alloyed with Si and/or B. These Me-Si-B (Me = metal) alloys form strengthening silicides and borides which improve their creep performance and oxidation resistance. Multiphase alloying systems like Mo-Si-B [1, 8, 9], Nb-Si(-B) [10, 11], and V-Si-B [12, 13] are promising candidates for future high temperature applications.

According to the melting point criterion after Fleischer [14], a high melting temperature often brings a high modulus of elasticity and thus has a positive effect on the dimensional stability of components under complex thermal loading. Additionally, there is an inverse proportionality between the melting temperature and the coefficient of thermal expansion, whereby refractory materials, in particular under thermo-cyclic loading show a favorable behavior [15]. Thus, due to the high melting point of Mo ($T_{M(Mo)} \sim 2600\,°C$ [16]) the Mo-based alloys provide the highest melting point of the ternary systems investigated so far and therefore offer the highest potential for such high temperature applications.

However, in this case, the advantage of a high melting point ($\sim 2400\,°C$ for PM Mo-9Si-8B) comes along with a high density ($9.58\,\frac{g}{cm^3}$ for PM Mo-9Si-8B [17]) which is a drawback for the flying applications. Particularly, when applied in rotating gas turbines, a reduction of the density would lead to a decreased moment of inertia and thus to a significant increase in efficiency [18]. Additionally, the turbine itself would become more lightweight, resulting in less fuel consumption and a reduced amount of exhaust emissions. So, density optimized Mo-Si-B alloys are of central scientific interest.

The scope of the present work is to reduce the density of Mo-rich Mo-Si-B alloys located within the "Berczik triangle" [19, 20] offering balanced microstructure property relation. An optimized composition in terms of microstructural constituents is given by a continuous Mo_{ss} phase with finely distributed intermetallic particles. In order to obtain a balance between the high temperature (creep and oxidation resistance) and room temperature properties (fracture toughness), the amount of Mo_{ss} should be around 50 % [17]. Thus, this phase is a decisive component of the alloying system investigated.

The major aim is to find additional lightweight alloying elements for an effective density reduction and strengthening of Mo_{ss} phase and, at the same time, without decreasing the fracture toughness. So, first investigations will focus on promising alloying elements like Ti, Zr and V evaluating their potential in terms of density reduction and solubility in the Mo phase as well as their impact on solid solution strengthening. Those considerations are discussed in Chapter 4.1. In the second step, the advantageous features of additional alloying elements observed for the binary systems are transferred on alloying concepts for ternary Mo-Si-B alloys, where especially the effect of V will be investigated. Therefore initial studies will be carried out on mechanically alloyed and thermally treated Mo-9Si-8B powders with varying V concentrations (10, 20, 30, 40 at.%). In Chapter 4.2, a detailed comparison of microstructures is described and finally allows an assessment of the influence of V on the properties of a Mo-9Si-8B alloy. Additional X-ray diffraction analysis enables the identification of participating phases which will be further refined using Rietveld method. The effects of such V alloying on the mechanical properties of Mo-9Si-8B, will be determined on field assisted sintered (FAST) and arc-melted (Arc) Mo-40V-9Si-8B alloys, both featuring a density reduction of around 17 %. Those ternary alloys are tested in terms of room temperature (RT) fracture toughness, brittle-to-ductile-transition temperature (BDTT) and high temperature (HT) creep resistance. The mechanical properties of the present alloys in comparison with other developed or currently used materials will be

subject of Chapter 4.4. Finally the effect of V on the oxidation properties of Mo-9Si-8B during cyclic oxidation tests between 800 °C and 1150 °C are interpreted in Chapter 4.5, which also introduces methods for improving the oxidation resistance.

The presented results will be critically discussed in order to evaluate the potential of V as alloying partner in Mo-Si-B alloys. Thus, this work should provide a further and important contribution for understanding the properties of Mo-Si-B alloys in combination to relatively new V-Si-B alloys and therefore closes the gap between both alloying systems. Chapter 5 summarizes the most important points and presents some interesting future prospects required for further work.

2 Mo-alloys for high temperature applications

2.1 Multiphase Mo-Si-B alloys

Multi-phase Mo-based alloys are of particular scientific interest as potential materials in aerospace engines and power generating industry. During the last decades research focuses on Mo silicides, since they combine excellent creep and acceptable oxidation resistance at ultra-high temperatures [21–24]. Beneficial properties are also known for Mo-borides which exhibit high melting points, elevated thermal and chemical stability as well as a high hardness and mechanical stiffness [25–27]. Since a mere addition of either Si or B is not profitable due to an increased brittleness especially concerning the Mo-Si system [28, 29], those binary compositions are not suitable for structural applications at high temperatures. According to the superior goal of creating a material combining creep and oxidation resistance at high temperatures with an acceptable room temperature (RT) crack tolerance and deformation potential, the following considerations focus on multiphase Mo-Si-B systems. The first isothermal section of the ternary phase diagram at 1600 °C was proposed in the mid-fifties by Nowotny et al. [30] and later modified by Perepezko and co-workers [31, 32] but also by Ha et al. [33] for the isothermal section at 1800 °C.

Based on the ternary Mo-Si-B phase diagram of Nowotny et al. [30], different research groups concentrated on two main compositional regions distinguished in Figure 2.1. The first system, highlighted in green, was characterized by Akinc and co-workers [34–39] and reveals a three-phase field composed of the binary intermetallic phases Mo_3Si and Mo_5Si_3 (T1) and the ternary intermetallic phase Mo_5SiB_2 (T2). Investigations show that alloys taken from the "Akinc triangle" exhibit excellent oxidation resistance. In this regard boron was identified as the decisive element for the formation of an protective SiO_2-B_2O_3 layer on the materials' surface. With a solubility range of 24 at.% – 27.5 at.% B [40], Mo_5SiB_2 serves as a reservoir for boron and is therefore a very important component in such alloys. In order to ensure a protective and self-healing oxide layer a relatively high boron concentration is required which reduces the viscosity of the SiO_2-B_2O_3 layer and thus supports the healing of quality degrading constituents (like pores or cracks) by viscous flowing [37].

Due to the compound of intermetallic phases with density values between $8.24\,\frac{g}{cm^3}$ for Mo_5Si_3 and $8.98\,\frac{g}{cm^3}$ for Mo_3Si, alloys taken from the "Akinc triangle" offer a comparably low density which represents an attractive feature for potential applications as turbine materials. However, the pure intermetallic character of these alloys provides a very high brittle-to-ductile transition temperature (BDTT) and low fracture toughness [41]. Thus,
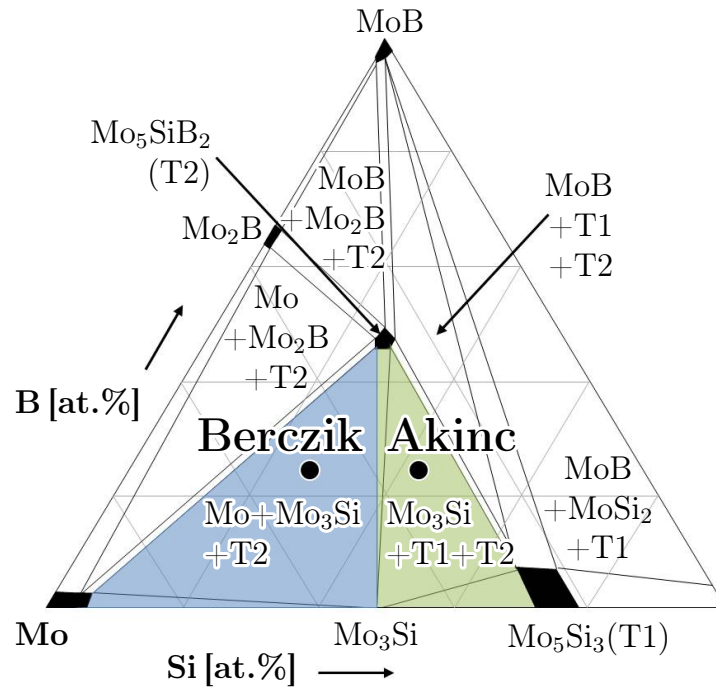
Figure 2.1: Isothermal section of the ternary Mo-Si-B system at 1600 °C [30, 32] for the Mo-rich compositions representing two main "triangles" investigated by Berczik et al. [19, 20] and Akinc et al. [34–39].

within this ternary phase field, the superior goal of an acceptable fracture toughness at room temperature cannot be achieved.

The second phase field was defined by Berczik et al. [19, 20] and is therefore called the "Berczik triangle", highlighted in blue in Figure 2.1 which is located between the Mo_{ss} phase and the intermetallic phases Mo_3Si and Mo_5SiB_2. Hence, due to the properties of corresponding phases, summarized in Table 2.1, the alloys taken from this compositional region exhibit promising characteristics for focused applications as turbine blade materials. The three-phase microstructure offers a wide stability range up to high temperatures of around 1800 °C [33] which features a positive effect on the creep resistance. In contrast to the Akinc approach such alloy compositions may have a comparatively reduced oxidation resistance, but provide an essential advantage: the ductile Mo_{ss} phase.

This microstructural component enables, depending on its volume fraction and distribution, a significant improve of the room and high temperature fracture toughness [42, 43]. It is well known that an increasing amount of Mo_{ss} phase in multi-phase alloys results in an improved fracture toughness [44]. In order to decrease the BDTT, a high volume fraction of continuously formed Mo_{ss} phase would be required while in terms of improving the oxidation and creep resistance a higher amount of intermetallic phases would be beneficial. Those microstructural constructs have been described by Schneibel [45] making a schematic classification of the competing requirements for optimum oxidation resistance, fracture toughness, and creep strength.

Table 2.1: Physical and mechanical properties of the Mo_{ss} phase and the intermetallic phases Mo_3Si and Mo_5SiB_2 [28, 41, 42, 46–51].

	Mo_{ss}	Mo_3Si	Mo_5SiB_2
Crystal structure	bcc (A2)	cubic (A15)	tetragonal (D8$_1$)
Melting point, °C	2623	2025	2160–2200
Density, $\frac{g}{cm^3}$	10.21	8.98	8.76
Young's modulus, GPa	324	295	383
BDTT, °C	< RT (high purity)	1400	1500
K_{Ic}, $MPa\sqrt{m}$	24	3	1.5–2
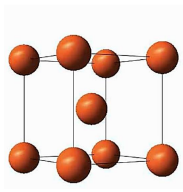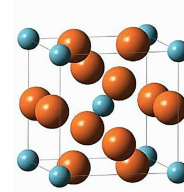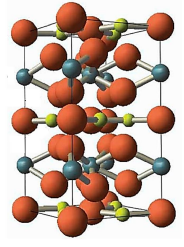
In general the microstructure property relations can be divided into two major groups:

I. Alloys having a large volume fraction of continuous **Mo_{ss} matrix** with embedded intermetallic particles and a relatively coarse microstructure. This combination of microstructural constituents provides a **high fracture toughness** due the ductile Mo_{ss} matrix strengthened by second phase hardening mechanism. However, taking into account the reduced amount of intermetallic phases, those alloy compositions suffer from poor oxidation and creep resistance.

II. Alloys providing an **intermetallic matrix** with small or near zero volume fraction of discontinuous Mo_{ss} phase. In case of a coarse-grained microstructure, a low fraction of ductile Mo_{ss} phase would not reduce the **creep resistance**. With regard to the oxidation performance the Mo_{ss} phase should be formed as small particles, less effecting the **oxidation resistance** than coarse Mo_{ss} phase regions.

So, designing an alloy in the region of the "Berczik triangle" always requires the challenge to find a compromise between the "weak" and "strong" microstructural features and thus, the resulting properties. Therefore, it has to be taken into account that the alloy composition as well as the manufacturing technique have an essential influence on the microstructure evolution.

Review of processing routes for Mo-Si-B alloys

The approach of an optimized microstructure was investigated by Berczik et al. [19, 20] who pointed out, that a microstructure consisting of an continuously formed Mo_{ss} matrix with homogeneously distributed intermetallic particles shows ideal properties.

In order to create such a microstructure, Berczik and co-workers [19, 20] used the gas atomization (GA) process with helium which is a splat quenching technique where a liquid is ejected through a fine nozzle and sprayed into a gas-filled vessel. Due to the high cooling rates, the powder particles solidify in a non-equilibrium state, forming a supersaturated Mo_{ss} powder. A subsequent thermal treatment during compaction then supported the formation of the desired microstructure. The resulting Mo-8.9Si-7.7B alloy exhibited a BDTT of around $500\,°C$ and additionally provided an acceptable oxidation resistance.

Major disadvantages of this procedure are high costs of the helium gas but also extreme process parameters like high pre-heating and very low cooling temperatures. Hence, there was an effort by Jéhanno et al. [52] trying to substitute helium by argon during GA of the Mo-8.9Si-7.7B alloy. However, the argon gas was not able to generate as high cooling rates as helium which results in a classical solidification of primary Mo_{ss} particles surrounded by the intermetallic phases. After consolidation via hot isostatic pressing (HIP) this alloy shows a coarse phase distribution and an intermetallic matrix resulting in an unfavorable BDTT of around $1150\,°C$.

This example illustrates the efforts to develop alternative processing routes. In the last years, several other production methods for different types of Mo-Si-B-X alloys have been established. An overview is given in the following Figure 2.2. The respective processing routes were classified and ranked according to their suitability for the production of an optimized microstructure according to Berczik.

In general the processing routes can be subdivided into four main groups: the ingot metallurgy (IM), the directional solidification (DS), the powder metallurgy (PM), and a recent technology, the additive manufacturing (AM). The first mentioned class is one of the oldest methods for metallic alloys production. Before casting, this process starts with melting the chemical elements together to convert them in to a homogenized liquid. This may be quiet difficult in case of strongly differing melting temperatures. Nevertheless, a certain control of the process parameters allows an active impact on the resulting microstructure. The arc-melting (Arc), which is described in detail in Chapter 3.1.2 on page 30, was proven to be a beneficial processing route for refractory alloys as it is able to reach maximum temperatures up to $3500\,°C$ [53]. Due to the conventional solidification path, the resulting microstructures are rather coarse, sometimes featuring large Mo_{ss} dendrites and mostly an intermetallic matrix [45, 51, 54, 55]. A representative microstructure is illustrated in Figure 2.2, showing the microstructure of a cast and annealed Mo-12Si-8.5B (at.%) [54]. Often, those alloys provide low values for fracture toughness between $7\,MPa\sqrt{m}$ and $12\,MPa\sqrt{m}$ as well as a high BDTT $>1000\,°C$ due to their typical solidification path by primary solidification of (large) Mo_{ss} islands and secondary solidification of the silicides or eutectic constituents [48, 54, 55].

A further development of ingot metallurgy is represented by the directional solidification (DS). A special feature to improve the BDTT is a lamellar arrangement of the phases, as it occurs during directional solidification (DS) of eutectic alloys. First investigations on

Processing Routes for Mo-Si-B-X Alloys

AIM: optimized microstructure (MS), according to Berczik, resulting in a balance between high temperature creep resistance (CR), high temperature oxidation resistance (OR) and room temperature fracture toughness (FT)

Ingot Metallurgy (IM) via arc-melting (Arc)

Mo-12.5Si-8.5B

10 μm

CR,OR   FT
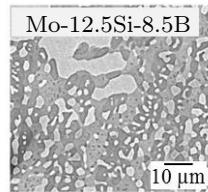
+ quick and easy fabrication of various alloy compositions
+ high melting points achieved
− often rather coarse microstructure
− disequilibrium condition after rapid solidification

Directional Solidification (DS) via zone melting (ZM)

growth direction →
Mo-17.5Si-8B

100 μm

CR,OR   FT
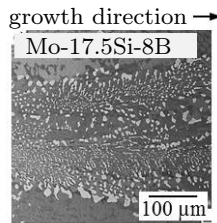
+ eutectic composition results in beneficial lamellar microstructure
+ defined microstructure by process parameters
− exact eutectic composition needed

Powder Metallurgy (PM) via cold isostatic pressing (CIP), sintering, hot isostatic pressing (HIP) or field assisted sintering technique (FAST)

Preliminary powders: Gas atomization (GA), Mechanical alloying (MA) Surface modified particles (SMP)

MA and CIP-sinter-HIP
Mo-9Si-8B

10 μm

CR,OR   FT
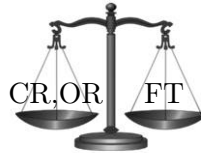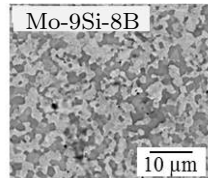
+ able to create an optimized MS according to Berczik
+ defined MS by process parameters
− multi-step near-net-shape process
− embrittlement due to oxygen contamination

Additive Manufacturing (AM) via selective laser melting (SLM) or laser metal deposition (LMD)

Mo-13.5Si-7.5B

5 μm

CR,OR   FT?
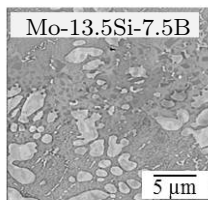
+ one-step near-net-shape process
+ beneficial eutectic regions
+ defined MS by process parameters
− rather coarse Mo_{ss} regions
− insufficient FT expected due to inhomogeneous MS and intermetallic matrix (not tested so far)

Figure 2.2: Processing routes for Mo-Si-B-X alloys including representative microstructures of IM Mo-12.5Si-8.5B [54], DS Mo-17.5-8B [56], PM Mo-9Si-8B [57], AM Mo-13.5Si-7.5B [58].

this method were carried out by Manson et al. [59,60] working on alloys consisting of a eutectic $MoSi_2$-Mo_5Si_3 composition. A variation of solidification velocities from $25 - 210\,\frac{mm}{h}$ resulted in a lamellar crystal morphology parallel to the growth direction. They found a decreased lamellar spacing to be beneficial in terms of creep behavior at $\geq 1300\,°C$. Other

multiphase zone melting (ZM) Mo-Si-B alloys were investigated by Ito et al. [61] as well as Wang and co-workers [62] reporting the appearance of a coarse microstructure with large Mo_{ss} regions resulting in a poor oxidation resistance. However, this could be improved by increasing the solidification rate to refine the microstructure. A similar context was given by a special comparison between an industrial PM route and an alternative ZM processing [63].

The elongation of the microstructure parallel to the growth direction was achieved for three-phase alloys having the composition Mo-9Si-15B [64]. Due to its high amount of intermetallic phases the three-point bending strength at 871 °C reaches very similar values as an ultra-fine-grained PM alloy Mo-6Si-5B [63]. So, these initial results show the potential of a well-aligned zone molten microstructure which also has advantageous effects on the creep performance. The impact of well-aligned arrangements of a three-phase microstructure on the creep performance was reported by Hasemann et al. [22, 56] investigating two near-eutectic alloys having the composition Mo-17.5Si-8B and Mo-17.5Si-10B. The creep properties were found to be outstanding compared to other Mo-Si-B alloys, even at temperatures above 1100 °C. This can be attributed to the directional solidified microstructure shown in Figure 2.2 illustrating a relatively high amount of intermetallic phases and eutectic colonies.

A very suitable approach to achieve the desired microstructure is the processing route via powder metallurgy (PM). An integral part of this manufacturing technique are the preliminary powders which can be prepared by gas atomization (GA), mechanical alloying (MA) or by surface modification. The most suitable way used for this thesis is represented by mechanical alloying which is detailed described in Chapter 3.1.1. This method enables a mixing of elements on the atomic scale forming a supersaturated solid solution.

A subsequent consolidation of powders can either be realized by a procedure including cold isostatic pressing (CIP), sintering and hot isostatic pressing (HIP) or using the field assisted sintering technology (FAST). Both routes offer the opportunity of consolidating the powders wide below their melting temperatures which makes this procedure favorable for processing of refractory metals [65]. Reaching operating temperatures of around 1500 °C these multi-step production routes lead to the formation of precipitations out of the supersaturated solid solution. Furthermore, the process parameters during mechanical alloying like powder-to-ball ratio or milling times are easy to modify and help to achieve a defined distribution of intermetallic phases. In addition to that, the alloy composition is a decisive criterion to obtain an optimized microstructure.

The key conditions to create the favorable continuously distributed Mo_{ss} phase were profoundly investigated by Krüger and co-workers [57]. Following the Berczik's approach it was found that a PM Mo-9Si-8B alloy exhibits an optimized property profile. Therefore the powder composition was mechanically alloyed in a planetary ball mill for 20 h forming the supersaturated Mo_{ss}. After a preliminary thermal treatment for 1 h at 1000 °C the existence of intermetallic phases Mo_3Si and Mo_5SiB_2 was already confirmed by X-ray diffraction measurements (XRD). Furthermore, the as-milled powders were consolidated via a CIP-sinter-HIP process resulting in finely distributed intermetallic particles embedded in a Mo_{ss} matrix. The continuous formation of the Mo_{ss} was investigated by Hassomeris et al. and confirmed using FIB tomography [66]. The achieved representative microstructure for the PM Mo-9Si-8B [57, 67] alloy is illustrated in Figure 2.2. This alloy combines an extended fracture toughness of 12.7 MPa$\sqrt{m}$ and a BDTT of around 950 °C [17]. Therefore,

a balanced combination of 50 % Mo_{ss} phase and 50 % intermetallic phases was found to be beneficial in order to combine the advantageous properties.

The fine-grained microstructure is beneficial in terms of oxidation resistance but unfavorable for creep due to grain boundary sliding. An additional thermal treatment may help to enhance the creep resistance by grain growth [21]. Outstanding creep properties can also be achieved by Mo-Si-B alloys having an intermetallic matrix. In this case the alloy with an amount of silicides > 50 % can be mechanically alloyed and consolidated, resulting in a microstructure comparable to that of PM Mo-13Si-12B reported by Krüger et al. [57]. This alloy composition additionally exhibits a good oxidation resistance due to the increased Si and B concentrations, but suffers from poor fracture toughness around $6\,MPa\sqrt{m}$ [17].

Another approach to design Mo-Si-B alloys with higher silicide concentrations, without forming an intermetallic matrix, was investigated by Schneibel [68] and Kruzic [69] who focused on surface-modified particles compacted via HIP. In a first step, ground powders of composition Mo-20Si-10B were vacuum-annealed which resulted in a loss of Si, and consequently a Mo solid solution layer, at the particle surfaces. Subsequent fabrication via HIP produced a microstructure of coarse silicide particles bonded by a nearly continuous Mo_{ss} matrix with a volume fraction in the order of 38 % [68]. As a result, those alloys had superior fracture toughness properties ($15\,MPa\sqrt{m}$). However, the best values were achieved, when increasing the amount of Mo_{ss} up to 49 % [45, 68].

The most critical issue of the PM route is the contamination with oxygen during MA reaching values between 1500 wppm and 3500 wppm [57, 70] depending on the milling time. In order to avoid a high oxygen contamination the handling and milling, as well as the consolidation of powders has to be carried out under inert atmospheres. Otherwise, even small amounts of oxygen can cause brittle intergranular fracture of pure Mo [71] at room temperature and thus, an embrittlement and increase of BDTT of PM Mo-Si-B alloys.

In a very recent approach, the multi-step PM route was replaced by a one-step process via additive manufacturing. It is a kind of combination of PM and IM route consolidating the pre-alloyed or mixed powders by an laser melting technology. Initial results were shown by Hagiara et al. [72] having first succeeded in fabricating $MoSi_2$ samples via selective laser melting (SLM) and clarified the criteria for the fabrication and control of the crystallographic texture. Additive manufacturing by SLM was also used to produce a Mo rich Mo-Si-B alloy which results in a typical Mo_{ss} dendritic microstructure with Mo_5Si_3 and Mo_5SiB_2 phases in the interdendritic regions [73]. The resulting SLM Mo-8.5Si-5.6B provides an indentation fracture toughness around $12\,MPa\sqrt{m}$ which could also be increased up to $18\,MPa\sqrt{m}$ by alloying with La_2O_3. The toughening is attributed to crack trapping (intrinsic toughening mechanism) by the presence of high volume fractions of ductile Mo_{ss} phase additional extrinsic toughening from oxide particles.

Another approach for additive manufacturing was presented by Schmelzer and co-workers [58] using an laser metal deposition (LMD) method for printing pre-alloyed near-eutectic Mo-13.5Si-7.5B powders. For this purpose, a powder was successfully produced via Ar GA of non-pre-alloyed solid raw materials. The consolidation via LMD produced dense volumes. The resulting microstructure shown in Figure 2.2 consists of primarily solidified Mo_{ss} phases, binary Mo_3Si-Mo_5SiB_2 and ternary Mo_{ss}-Mo_3Si-Mo_5SiB_2 regions, which are presumed to have excellent creep properties [56].

Finally, the mechanically alloying and consolidation via FAST is the most promising manufacturing technique to create a balanced microstructure of 50 vol.% continuous Mo_{ss}

phase with 50 vol.% of embedded intermetallic (Mo_3Si and Mo_5SiB_2) particles. However, the arc-melting also represents an advantageous technique due to a fast and easy production of a large number of various alloys. Thus, those two processing routes were selected for alloy fabrication in the present thesis and are described in detail in Chapter 3.1.1 – 3.1.2. The present work focuses on the reference alloy composition Mo-9Si-8B due to its advantageous microstructure after PM. In the following, the main objectives of reducing the density of that alloy composition, without having a negative impact on its mechanical properties will be pursued. Useful approaches for density reduction are presented in the next section.

2.2 Approaches for density reduction by micro- and macroalloying

In addition to the manufacturing technique, the alloy composition also has a significant influence on the resulting microstructure and characteristic properties. The addition of the elements Si and B in Mo alloys not only leads to the formation of second phases, but also a fractional amount is dissolved in the Mo_{ss} phase, and therefore, affects the fracture toughness, ductility and strength of this microstructural constituent and, of course, the density of alloys. So, prior research of Sturm et al. [28] on Mo-$(0.34-3.34\,\text{at.\%})$ Si solid solutions imply that Si additions caused pronounced solid solution strengthening but also significant embrittlement of the Mo_{ss} phase, i.e. the fracture toughness decreased from about $24\,\text{MPa}\sqrt{\text{m}}$ for pure Mo to about $4\,\text{MPa}\sqrt{\text{m}}$ for a Mo alloy with 3.34 at.% Si. Furthermore, it is well known that the oxygen concentration ($\sim 50\,\text{wt.ppm}$) [71] in the Mo_{ss} phase contributes to further embrittlement [74].
Considering the fact that a high proportion of Mo_{ss} (about 50 %) phase is needed to create an alloy with balanced ambient and high temperature properties, the relevance of this phase becomes apparent. Its characteristics have a significant influence on the resulting properties of the Mo-Si-B alloys. If the potential of an ideal Si and B concentration has been exhausted, the addition of lightweight alloying elements by micro- (< 1–$2\,\text{at.\%}$) or macroalloying ($> 2\,\text{at.\%}$) can be used for further optimization of the mechanical properties as well as a density reduction of ternary Mo-Si-B alloys.

Suitable refractory alloying partners and their effects on Mo_{ss} and binary systems

Lightweight alloying elements like Al, Ti or Zr can contribute to the density reduction of Mo-based alloys. However, according to Northcott [74], the solubility of Al in Mo at room temperature is negligible, so no significant increase in neither the strength nor the ductility of the Mo solid solution can be expected [75, 76]. Thus, a high mutual miscibility of the alloying partners is decisive. Sakidja et al. [32] reported that alloying elements of the refractory metals family (IV, V and VI group of the periodic table of the elements) offer the highest potential for targeted property improvement. According to that, the elements Nb, Cr, Zr, V and Ti are promising alloying partners with regard to the density

reduction of Mo-based alloys. In Table 2.2, those elements were evaluated concerning their density [77] compared to pure Mo as well as their solubility in the Mo_{ss} phase (according to the binary phase diagrams illustrated in the Appendix on page 85 ff.) [78,79] and difference of atomic radii. For an effective solid solution hardening, a huge miscibility range and widely differing atomic radii are favorable, resulting in a significant lattice distortion [80]. A closer look at Table 2.2, demonstrates that the elements Nb and Cr are rather unfavorable for the targeted objective. Obviously, their density is smaller as compared with Mo, but especially for Nb the density difference is too small to cause an effective weight reduction in spite of a high solubility in Mo. Even if Cr would cause a comparably higher density reduction, the miscibility gap in the binary Mo-Cr system represents an unfavorable feature. More promising alloying elements are Zr, V and Ti (phase diagrams shown in the Appendix on page 85 ff.) due to their much smaller density compared with Mo. According to computational calculations by Geller and co-workers [81], Ti and Zr even have a ductilizing effect on Mo. In terms of Zr, this might be due to the gettering effect for oxygen.

The addition of 1 at.% Zr to the base alloy composition Mo-1.5Si led to a fourfold increase of strength and, simultaneously, to an increase of ductility even at room temperature. There are different reasons that could be made responsible for these improvements: (I) the reduction of grain size during powder metallurgical processing reducing the overall concentration of interstitial impurities at grain boundaries [74] (II) the formation of ZrO_2 nanoparticles, by which Zr cations getter the detrimental oxygen and affect the strength by particle-strengthening, (III) the reduction of Si segregation to grain boundaries alleviating grain boundary embrittlement [29, 82]. However, the solubility of Zr in Mo at room temperature is quite low, i.e. < 1 at.% according to the phase diagram [79] illustrated in the Appendix on page 86; higher alloying additions lead to the formation of the secondary phase Mo_2Zr. Microstructural investigations by Mousa et al. [83] showed the additional Mo_2Zr and $MoZr_2$ nano-phase formation in a Mo-1.5Si-1Zr alloy which might contribute to an extra strengthening beyond the effect of the ZrO_2 nanoparticles, which was reported by several authors [29, 84, 85].

The solubility range of Ti and V in Mo is very large, in case of V the generally available

Table 2.2: Evaluation of suitable lightweight alloying elements to Mo, based on density, solubility and atomic radii difference [77–79].

	Density, $\frac{g}{cm^3}$	Solubility in Mo_{ss}	Atomic radii difference, %
Mo	10.22	Host lattice	0
Nb	8.57	Completely	$+4$
Cr	7.19	Miscibility gap at $T < 880\,°C$	-8
Zr	6.51	Up to $10\,\%$ at $1880\,°C$, At higher concentrations $Mo + Mo_2Zr$	$+15$
V	6.09	Completely	-4
Ti	4.54	Soluble up to $10\,\%$ at RT	$+7$

phase diagram shows complete solubility. However, a more recent Mo-V-phase diagram (Appendix, page 87) from FactSage [86] indicates a miscibility gap, which has not been proven so far. However, these systems are worth to investigate in terms of the effects of solute atoms on the mechanical properties of the solid solution phase.

Fan et al. [87] found Ti to be beneficial for an improved tensile strength of Mo-(0.3...1.0 wt.%) alloys. Those findings were confirmed by Olds and Rengstorff [88] pointing out the positive effect of Ti additions on the tensile strength and ductility of ingots. This phenomenon was replied by Hiraoka et al. [89] using tensile tests for demonstrating the positive effect of Ti on the fracture strength on powder metallurgically processed Mo alloys. Further tensile tests on those alloys containing 0.2–1.98 at.% Ti carried out at lower temperatures (173–363 K) [90] showed that Ti addition increases both intergranular and transgranular fracture strengths. The evaluation of the critical stress and temperature (representing low-temperature strength and ductility of the material) indicates that the ductility of Mo was improved and the BDTT was decreased by adding Ti. Studies of Inoue et al. [91] revealed that increasing Ti concentrations up to 2.97 at.% improve the hardness due to solid solution strengthening. The effect of higher Ti concentrations in Mo_{ss} was not investigated yet and is, therefore, an important part of the present study.

Hiraoka et al. [92] found out that apart from Zr and Ti the addition of V leads to an increase of yield and fracture strength in Mo alloys as well. Northcott [74] also referred to V as alloying element which increases the hardness, tensile strength and improves the creep properties of Mo. Geller et al. [81] performed a computational screening for identifying ductilizing additives to Mo by means of Rice-Thomson-parameters. Although elemental V is predicted to be ductile its ductilizing potential for Mo is minimal compared to other elements like Ti and Zr. Hence, it appears that the ductility of the pure additive does not necessarily correlate with its effect in bcc Mo alloys. However, combinations of minor V additions ($\sim 0.19...1.87$ at.%) and B ($\sim 0.03...0.06$ at.%) were proven to enhance ductility and strength in Mo alloys [92]. Even V-Si alloys reported by Hasemann et al. [93] providing a five times higher plastic strain as compared to Mo-Si alloys indicate a potential ductilizing effect of V.

This review demonstrates that Ti, Zr and V are promising candidates for the improvement of properties of Mo-base alloys. However, no systematic investigations were carried out so far regarding the influence of higher concentrations of alloying additions beyond the results described above on the microstructures and the mechanical properties of binary Mo alloys from room temperature up to possible application temperatures of 1100 °C.

Effect of alloying on ternary Mo-Si-B alloys

The findings from the binary alloy systems were helpful in oder to understand the potential of different alloying elements on Mo. However, for practical applications, the multinary systems are of higher importance and therefore discussed in this section. As explained before, Nb and Cr are rather unfavorable for focused density reduction, however, their impact on Mo-Si-B alloys had been investigated with another focus.

Jéhanno and co-workers [21] reported the creep properties of an Mo-2.7Nb-8.9Si-7.7B alloy where Nb was added for solid solution strengthening of the Mo matrix. As can be seen in
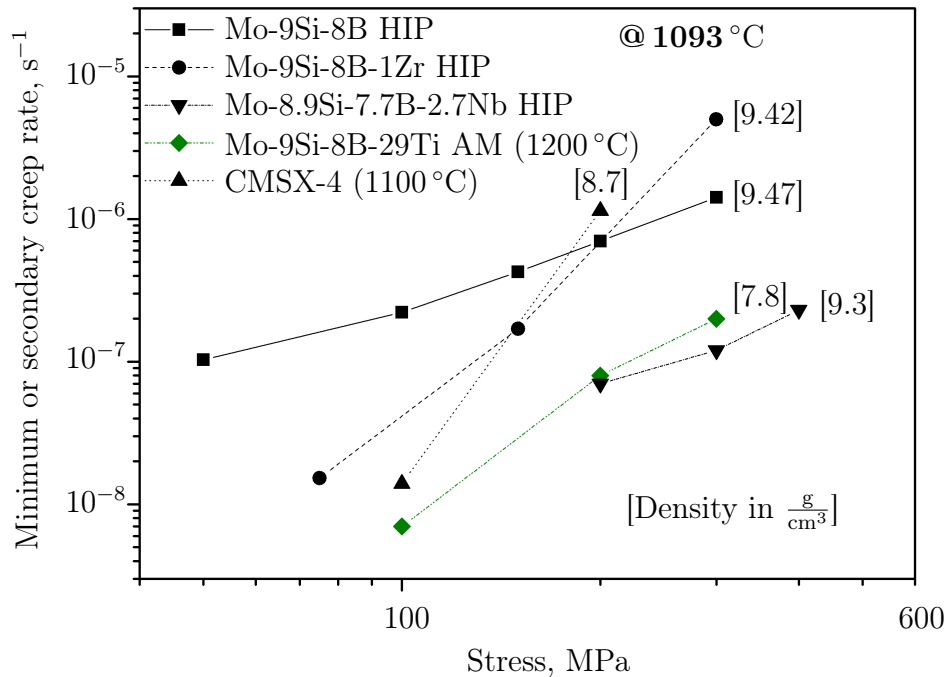
Figure 2.3: Creep properties of Mo-9Si-8B alloys, partly with additional alloying elements, presented in comparison with the single-crystalline nickel-based superalloy CMSX-4 [21, 67, 70, 96].

Figure 2.3 Nb provides a positive effect on the creep resistance, which was also observed by Schneibel [94] for partial substitution of Mo with Nb at temperatures ranging from 1200 °C to 1400 °C. The comparably good creep performance of the Mo-8.9Si-7.7B-2.7Nb (Figure 2.3) alloy is due to its intermetallic matrix and coarser grain sizes due to arc-melting. However, the effect of minor Nb additions on the density reduction was comparably low. Further studies by Behrani et al. [95] concentrate on Nb-Mo-Si-B alloys characterizing a Mo-42.6Nb-12.3Si-1.1B (wt.%) for closing the gap between Mo-Si-B and Nb-Si-B systems. The results show that Nb-containing alloys proved to be not as oxidation-resistant as Mo-Si-B alloys.

In contrast, Burk and co-workers [97] found macroalloying with Cr (> 25 at.%) to be beneficial in terms of improving the oxidation properties of a Mo-9Si-8B alloy in the temperature region around 750 °C. In terms of density reduction, Cr was used by Sakidja et al. [98] for the substitution of Mo in a Mo-35Cr-10Si-20B alloy. Even if the half of Mo was substituted by Cr, a density of $8.5 \frac{\mathrm{g}}{\mathrm{cm}^3}$ was achieved. Hence, alloying with Cr would neither help to induce an effective weight loss regarding the favored PM Mo-9Si-8B alloy ($\rho = 9.47 \pm 0.05 \frac{\mathrm{g}}{\mathrm{cm}^3}$ [99, 100]) nor to undercut the density of of current Ni-based super alloys (e.g. $\rho = 8.7 \frac{\mathrm{g}}{\mathrm{cm}^3}$ for CMSX-4 [5]).

The alloying elements Zr and Ti show more promising potential in terms of featuring the mechanical properties of ternary Mo-9Si-8B alloys including a density reduction and were therefore reported by several authors. According to Figure 2.3 small additions of Zr affect the creep properties positively. Due to the small miscibility range the initial studies were
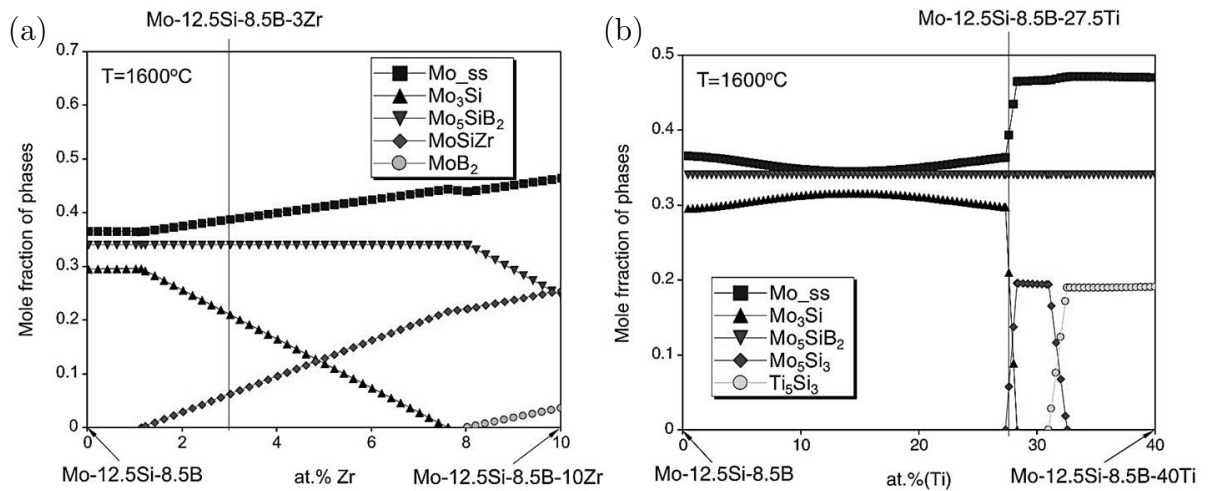
Figure 2.4: Calculated mole fractions of phases as a function of (a) Zr and (b) Ti concentration at $1600\,^{\circ}$C for $x_{Si} = 12.5$ and $x_B = 8.5$ (at.%) [102].

performed with Mo-9Si-8B alloys containing $0.5\,$at.% $-1\,$at.% Zr. The investigations show both, an increase of strength by around $600\,$MPa at temperatures up to $950\,^{\circ}$C and decreased BDTT by more than $150\,$K compared to the reference alloy [101]. Although possessing a very fine microstructure the Mo-Si-B-Zr alloys provide a creep resistance comparable to state-of-the-art Ni-based single-crystal alloys [70]. According to Figure 2.4 (a), higher Zr concentrations $>1\,$at.% led to an increase of MoSiZr phase and simultaneously decrease of Mo_3Si within the initial phase equilibrium composed of Mo_{ss}-Mo_3Si-Mo_5SiB_2. From $8\,$at.% to a maximum of $10\,$at.%, the phase composition was extended by MoB_2 and therefore replaced the Mo_3Si phase [102]. Other results reported by Hochmuth and co-workers [100] showed that Mo-9Si-8B alloys with 1, 2 and $4\,$at.% form ZrO_2 particles instead of SiO_2. They state that the creep rates degrade for higher zirconium contents due to larger Mo_2Zr and $MoZr_2$ particles.

Despite the limited density reduction, Zr can be considered as a very effective alloying element to Mo-Si-B alloys in terms of improving the mechanical properties. This was also reported by Krüger et al. [103] showing that mechanical alloying in addition to the Zr effect reduces the BDTT by more than $150\,^{\circ}$C and improves the indentation fracture toughness up to $20\,$MPa$\sqrt{m}$ as well as the plastic deformability ($0.8\,\%$) of Mo-9Si-8B-1Zr alloys. This is due to the evolution of a continuous Mo_{ss} phase by optimized PM processing combined with the "cleaning effect" of the Mo_{ss} by ZrO_2 formation as well as crack deflection at the Mo_{ss}/ZrO_2 interfaces. The strength up to $1400\,^{\circ}$C was reported to be higher for the silicide matrix materials as compared to the alloy having a Mo_{ss} matrix. So, the high-temperature deformability was mainly driven by the distribution of the comparatively weak Mo_{ss} phase for which the strengthening effect of Zr was no more effective at $T > 1200\,^{\circ}$C.

Recent research on Mo_{ss}-molybdenum silicide/ boride materials is focused on alloys with lower densities, e.g. incorporating the $Mo(Ti)_5Si_3$ phase [104]. According to the calculations of Yang et al. [102], illustrated in Figure 2.4 (b), it was found that the phase factions of Mo_{ss}, Mo_3Si and Mo_5SiB_2 in Mo-Si-B(-Ti) remain approximately constant up to additions of maximum $27\,$at.% Ti, afterwards a sudden change in phase equilibria occurs. Yang et al. [102], Azim et al. [105] as well as Schliephake and co-workers [96] pointed out

that Ti concentrations above 27 at.% cause a strong decrease of Mo(Ti)$_3$Si phase fraction (see Figure 2.4 (b)) which is then converted to the more oxidation resistant Mo(Ti)$_5$Si$_3$ phase [32]. However, an isothermal section of Mo-Si-Ti-8B phase diagram at 1600 °C [106] illustrates that the phase region Mo$_{ss}$ + T1 + T2 is very small and therefore difficult to reproduce, which often leads to the formation of Ti(Mo)$_5$Si$_3$ phase instead of Mo(Ti)$_5$Si$_3$ phase.

Hence, investigations on a Mo-12.5Si-8B-27.5Ti alloy [96, 106] showed that beside the Mo(Ti)$_3$Si and T2 phase the Ti(Mo)$_5$Si$_3$ phase is additionally formed resulting in a decreased fraction of Mo(Ti)$_{ss}$ phase (38 %). For a Mo-9Si-8B material alloyed with 29 at.% Ti the fraction of Mo(Ti)$_{ss}$ phase is twice as high. Beside the density reduction, this alloy (Figure 2.3) features extraordinary creep properties due to the solid solution strengthening of Mo$_{ss}$ by Ti as well as particle hardening via Ti(Mo)$_5$Si$_3$ particles [106]. Unfortunately, in this case the Mo(Ti)$_5$Si$_3$ phase which primarily was meant to improve the creep and oxidation properties was completely replaced by Ti(Mo)$_5$Si$_3$ [96]. So, the approach of alloying with Ti represents a very profitable way with respect to density reduction and additionally improving the high temperature properties. However, with regard to the objective of the present thesis the limited solubility as well as the phase shifting represent limiting aspects for the production of a balanced microstructure according to Berczik [19, 20].

Concerning this aspect, V as another lightweight element with a density of 6.1 $\frac{g}{cm^3}$ was identified as a potential alloying partner that can be entirely solved in the Mo$_{ss}$ phase, according to the binary Mo-V phase diagram [79]. Based on the scheme of alloying strategy reported by Sakidja et al. [32], V is known as a BCC, T2 and A15 stabilizer which makes it favorable for substitution in a Mo-9Si-8B alloy without phase shifting. Additionally, thermodynamic calculations [12], already showed that V alloys with Si and B additions form similar phases in the V-rich portion of the V-Si-B system as compared with ternary Mo-Si-B alloys. In the present work, substitution of V into the microstructure of Mo-9Si-8B leading to a Mo$_{ss}$-(Mo,V)$_3$Si-(Mo,V)$_5$SiB$_2$ alloy will be analyzed. Finally, a characterization of PM and Arc processed Mo-XV-9Si-8B alloys concerning their room and high temperature properties compared with other Mo-Si-B materials enables an assessment of the suitability of V as beneficial component in Mo-Si-B systems.

2.3 Deformation and strengthening of Mo-based alloys - from ambient up to elevated temperatures

A materials' characterization always should reflect the relevant properties for the focused application. Especially, Mo-Si-B alloys as structural materials for turbine blades, should provide a balance between room temperature toughness and high temperature strength as well as oxidation resistance. In particular the mechanical properties are significantly effected by plastic deformation in a wide temperature range caused by dislocation movement within the crystal lattice [107]. There are several ways to impede this movement by means of hardening mechanisms and therefore to control the strength and ductility of

the materials. Under real conditions those strengthening mechanisms do not only occur individually but also combined and therefore affect the mechanical properties of the entire material.

So, in pure single crystals, the lattice friction stress (σ_0 the minimum required stress for moving dislocations; also called Peierls stress τ_0) as well as solid solution atoms (solid solution hardening σ_{SS}) contribute to the macroscopic strength. Moreover, in polycrystalline alloys, grain boundaries (grain size effect σ_{GS} after Hall-Petch) as well as phase boundaries (e.g. particle hardening σ_{PH}) and dislocations caused by plastic pre-deformation (work hardening σ_{WH}) additionally impede the free movement of dislocations [80]. So, taking all these mechanisms into account, their sum, shown in Equation 2.1, represents the total critical stress for dislocation movement.

$$R_e = \sigma_0 + \sigma_{WH} + \sigma_{SS} + \sigma_{GS} + \sigma_{PH} \tag{2.1}$$

In general, it has to be considered that the strength and ductility behave contrarily, so often there is a decrease of ductility when applying the hardening mechanisms. This fact explains the characteristic properties of Mo-Si-B alloys. In contrast to pure Mo reaching a room temperature plastic strain up to 20 % [74], the ternary system is affected by several impacts. On the one hand the deformability is limited due to the interstitially dissolved foreign atoms [71, 74, 88, 108] as well as forming a substitutional solid solution [28]. On the other hand, the high amount of intermetallic phases having a low crystal symmetry (like many ceramics), contribute to the room temperature brittleness. Due to the comparable low packing density, the Peierls stress may exceed the fracture stress, before dislocation movement can occur [107].

The chemical element V is well known for its ductilizing potential and is therefore not only beneficial for density reduction of Mo-Si-B alloys but also favorable in terms of mechanical properties. According to Northcott [74], its high solubility in Mo also features a high solid solution strengthening effect improving the hardness of Mo solid solutions, illustrated in Figure 2.5. In order to discuss the mechanical properties of V-added Mo alloys, the different hardening mechanisms, have to be considered.

The following Table 2.3 represents an overview on the main principles of hardening mechanisms. Detailed descriptions, including further equations for estimating the individual impacts, were given by Bürgel [15], Rösler [80] and others [107, 109, 110]. Out of these mechanisms, the calculation of solid solution hardening is a very useful way to assess the direct impact of V on the mechanical properties of Mo-based alloys and is therefore described more detailed in this work.

Characterization at ambient temperatures - solid solution hardening

The solid solution hardening was shown to be very effective in Mo-Si alloys [74]. Dissolving of Si in the Mo lattice leads to a strengthening effect based on differing atomic radii. In case of Mo-Si, a substitutional solid solution is formed, fulfilling the requirement of an absolute value for difference of atomic radii less than 15 %. Otherwise, if there is a higher difference within the atomic radii, an interstitial solid solution is formed more likely, e.g.

as shown for B in Mo_{ss} [114].

Compared with the interstitial atoms, the substitutional atoms affect dominant lattice distortion and are therefore more effective for impeding dislocation movement. According to that, various interactions with dislocations occur:

I. The parelastic interaction (lattice parameter effect) describing the lattice distortion due to the integration of foreign atoms in the host lattice. The resulting elastic deformation is caused by differing atomic radii leading to tensile (for smaller atomic radii compared to host lattice) or compression (for higher atomic radii compared to host lattice) stresses.

II. The dielastic interaction (shear modulus effect) is based on the direct proportionality between the shear modulus and the dislocation energy. The dissolved atoms in the solid solution may cause another shear modulus than the matrix (host lattice) which affects the total dislocation energy.

III. The chemical interaction (Suzuki effect) points out that the stacking fault energy depends on the chemical composition and so, usually decreases with increasing concentration of foreign atoms [107].

Based on those interactions it was possible to assess the impact of different alloying elements on the solid solution hardening in Mo-5X (X = Ti, Zr, V at.%) alloys. The corresponding results helped to evaluate the potential of V as alloying element in Mo-based alloys compared to typical lightweight elements like Ti and Zr.

Well-known models for solid solution hardening were proposed by Fleischer [115] for alloying additions of $c \leq 0.1$ at.% and Labusch [116]. The model of Labusch is used for alloys with $c \geq 2.5$ at.% alloying addition and is therefore suitable for the calculations on the present
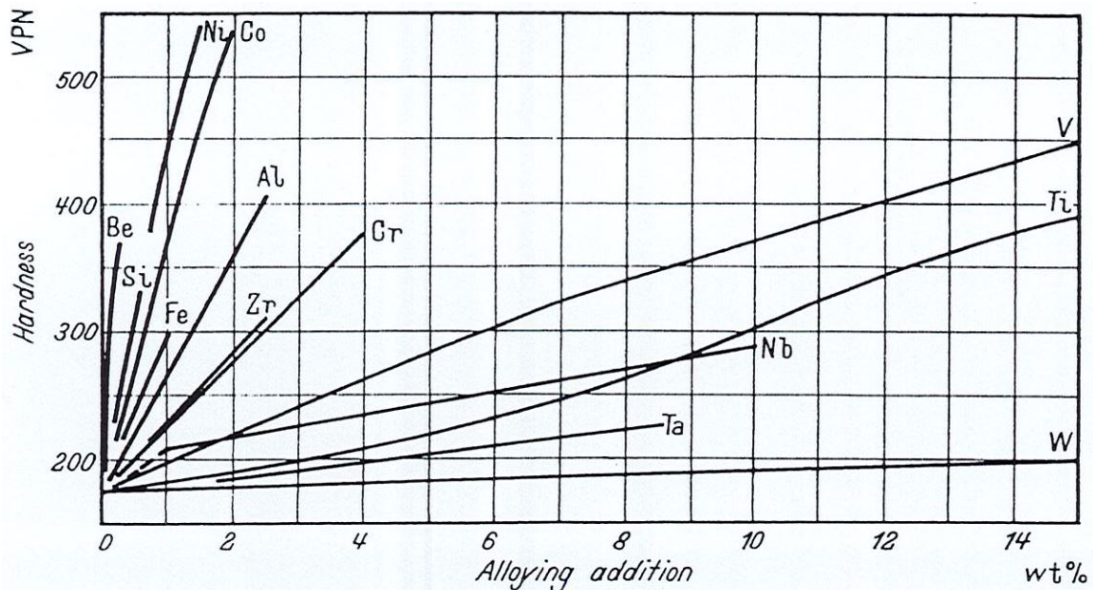
Figure 2.5: Influence of various alloying elements on the hardness of as-cast Mo-alloys [74].

Table 2.3: Hardening mechanisms in Mo-Si-B alloys [15, 28, 29, 57, 74, 80, 107, 109–113].

Key principle of hardening mechanism	Temperature (T) dependence
Work Hardening (σ_{WH}): Dislocations (around $\rho = 10^{12}\,\text{m}^{-2}$ in polycrystalline alloys) after production process e.g. arc-melting. During processing e.g. via mechanical alloying, additional dislocations (up to $\rho = 10^{16}\,\text{m}^{-2}$) formed on phase- or grain boundaries (Principle of Frank-Read source). The contibituion of WH depends on dislocation density (ρ), according to: $\sigma_{\text{WH}} = kMGb\sqrt{\rho}$	$< 0.4\,T_{\text{M}}$: High strength but increasing embrittlement with increasing dislocation density $> 0.4\,T_{\text{M}}$: Decreasing effect due to recovery and recrystallization e.g. via thermal treatment or high application temperatures
Solid Solution Hardening (σ_{SS}): Lattice distortion due to inclusion of foreign atoms. The impact essentially depends on: the difference of atomic radii determining the type of solid solution (interstitial or substitutional) as well as the concentration (c) of foreign atoms according to: $\sigma_{\text{SS}} \sim c^n$, with n ~ 0.5	$< 0.4\,T_{\text{M}}$: Increased strength and significant embrittlement $> 0.4\,T_{\text{M}}$: Impact decreases with increasing T
Grain Size Effect (σ_{GS}): Grain boundaries acting as barriers for dislocation movement e.g. in fine-grained PM Mo-9Si-8B, which leads to dislocation pile-up until critical stress activates sliding system of the neighboring grain. The impact depends on the grain size (d) according to the Hall-Petch theory: $\sigma_{\text{GS}} = \frac{k_{HP}}{\sqrt{d}}$	$< 0.4\,T_{\text{M}}$: High strength without decrease of ductility $> 0.4\,T_{\text{M}}$: Decrease of strength, coarser microstructure required e.g. for creep resistance
Particle Hardening (σ_{PH}): Particles or precipitates as lattice mismatches compared to matrix lattice, e.g. La_2O_3,Y_2O_3 doped PM Mo-Si-B alloys or precipitation hardening during thermal treatment of supersaturated Mo(Si,B) solid solutions. Phase boundaries can appear coherent, incoherent or partially coherent. According to their obstacle effect, the particles can be cut or bypassed (Orowan): $\tau_{\text{cutting}} = k\sqrt{f_V r}$ or $\tau_{\text{Orowan}} = k'\frac{\sqrt{f_V}}{r}$. So, the impact depends on the Particle radius (r) and their volume fraction (f_V).	$< 0.4\,T_{\text{M}}$: High strength $> 0.4\,T_{\text{M}}$: Very effective due to thermal stability of particles
Second Phase Strengthening: Intermetallic phases (IP) as silicides and borides in Mo-Si-B alloys occurring in different morphologies, e.g. lamellar or penetrating structure, affect the mechanical properties directly via their volume fractions and distribution.	$< 0.4\,T_{\text{M}}$: High strength, embrittlement with increasing fractions IP or silicide matrix $> 0.4\,T_{\text{M}}$: High strength due to thermal stability of IP

Mo$_{ss}$ alloys. For the purpose of this discussion, an equation compiled by Vöhringer [117] is used, which has been shown to work well for solid solution strengthening contribution in copper:

$$\sigma_{\mathrm{SS}} = M \left(\frac{G}{550} \right) \varepsilon_L^{\frac{4}{3}} c^{\frac{2}{3}} \tag{2.2}$$

where $M = 3.1$ is the Taylor factor, G the shear modulus of Mo with 130 GPa [16], c the solute fraction in at.%, and ε_{L} is:

$$\varepsilon_L = \sqrt{\eta'^2 + (\alpha_{\mathrm{d}} \, \delta)^2} \tag{2.3}$$

with $\alpha_{\mathrm{d}} = 15$ (for simultaneously occurring screw- and edge dislocations), the shear modulus misfit η and atomic size misfit δ given by:

$$\eta' = \frac{\eta}{1 + \frac{1}{\eta}} \tag{2.4}$$

where η is defined as:

$$\eta = \left(\frac{1}{G} \right) \left(\frac{dG}{dc} \right) \tag{2.5}$$

and

$$\delta = \left(\frac{1}{a} \right) \left(\frac{da}{dc} \right) \tag{2.6}$$

with a, the lattice parameter.

In order to get the contribution of solid solution hardening on the microhardness value, first the relevance of other hardening mechanisms, termed in the generalized Equation 2.1, needed to be discussed. According to Equation 2.1 the particle hardening (σ_{PH}) can be neglected when focusing on processes in pure Mo solid solutions.

As a minimum parameter of stress, the lattice friction has to be overcome in order to induce sliding processes. The resistance against dislocation sliding through an ideal or defect-free lattice is called Peierls-Nabarro stress (or short: Peierls stress) [15]. Significant values for this kind of stress are mainly assumed for bcc metals, like for Mo$_{ss}$ at room temperature. Estimating the Peierls stress of pure Mo by using highly idealized models resulted in values ranging from $\sigma_0 \approx 1.95 - 6.5$ GPa [118, 119]. While these models can explain the sliding behavior, their predicted magnitude for Peierls stress is overestimated by a factor of about three when compared to experimental yield stresses [120]. So, under real conditions, point defects like vacancies exist leading to a reduction of Peierls stress. The performance of microhardness measurements on pure Mo$_{ss}$ devoted a value of 2.6 GPa. It was then assumed, that the hardness of the present Mo-X (X = Ti, Zr, V) solid solutions is caused by additional hardening mechanisms, according to Table 2.3, when subtracting the hardness value of pure Mo.

The work hardening is a parameter resulting from the production process and the accompanied dislocation structure. It plays a major role for highly deformed alloys, e.g. cold worked or mechanically alloyed materials, as explained in Table 2.3. Hence, the arc-melting and subsequent cooling process used for the alloys production induced residual stresses, which were reduced by a thermal treatment at 1400 °C for 24 h. Therefore, it was assumed that the remaining dislocation density is in the same order of magnitude for all Mo$_{ss}$ alloys

investigated, due to their similar processing.

The influence of the grain size calculated by the Hall-Petch theory [121, 122] can be neglected for those alloys because the Vickers indents were set within comparably large grains so that the grain boundaries may not affect the hardness values significantly. According to these assumptions the impact of the individual solid solution effects of the selected solutes can be assessed by the microhardness results.

Characteristics at elevated temperatures - brittle-to-ductile-transition

When characterizing Mo-Si-B alloys, not only the hardening mechanisms but also the high volume fractions of intermetallic phases provide strong impacts on the mechanical properties at room temperature. As mentioned before, the intermetallic phases typically offer a brittle behavior as well as poor room temperature fracture toughness for this class of alloys, while the Mo_{ss} is the only ductile and comparatively tough phase in this alloy system.

The assessment of fracture toughness at room temperature, detailed described in Chapter 3.6.2 on page 36, leads to a further question regarding the materials' failure: Is there a chance to influence the brittleness by using metallurgical and metal physical strategies? In general, the yield strength at room temperature can not be achieved, since sudden fracture occurs before plastic deformation, indicating brittle fracture behavior, according to [107]. At elevated temperatures, thermal activated plastic deformation processes begin and lead to a transition from brittle to ductile deformation behavior. In order to distinguish those two deformation states there is a clear transitional zone in between those regions, the so-called brittle-to-ductile transition, which is not a material constant, however, but depends on the respective stress condition and the loading rate [80].

In the present thesis the brittle-to-ductile transition temperature (BDTT) was chosen as a representative value which was determined by three-point bending tests up to $1100\,^\circ\text{C}$.

Mechanical properties at high temperatures - creep performance

Designing an alloy for high temperature application means to create a material which is able to withstand considerable loads for extended periods of time. Thus, the resistance to creep deformation is an important aspect that has to be considered for use in turbine blades. According to Figure 2.6, stressing a component with constant load at elevated temperatures of at least $0.4\,T_\text{M}$ results in an increase of strain over time until materials' failure occurs by rupture. The following schemata illustrate (a) a constant load creep curve and (b) the variation of strain rate over time, both presenting the three stages of creep. Those creep curves can be subdivided into three main regimes, starting with (I) the transient or primary creep stage. Initially an instantaneous and time-independent strain ε_0 occurs leading to materials' transient creep response. This behavior is illustrated by the decreasing strain rate $\dot{\varepsilon}$ with time reaching a minimum and going over to (II) the steady-state or secondary creep stage. The secondary stadium can persist for a substantial

period of time and is important for the lifespan of the material. Finally the creep rate increases in the (III) third or tertiary creep stage which ends relatively soon in materials' failure.

The material behavior in the primary phase is based on strain hardening due to the formation and interaction of dislocations. The nearly constant creep rate in the steady-state is caused by a dynamic balance between hardening and softening process in the lattice. If a critical stress level and/or temperature is reached, this balance can get lost and the accelerating creep strain of the tertiary stage becomes gradually dominant. Simultaneously, several microstructure changes like localized necking or the formation of microvoids lead to crack formation and growth and thus to materials' failure at the end of tertiary creep stage.

For technical application the strain rate $\dot{\varepsilon}_{\mathrm{II}}$ of secondary creep state is of special importance. The evaluation of secondary creep rate is based on the so called the Norton's creep law [80]:

$$\dot{\varepsilon}_{\mathrm{II}} = B\,\sigma^n\,\exp(-\frac{Q}{R\,T}) \tag{2.7}$$

where B is a constant, σ the applied stress, n the stress exponent and Q the characteristic activation energy for creep process. In this context, R the ideal gas constant ($8.31\,\frac{\mathrm{J}}{\mathrm{mol\,K}}$) [123] and T the temperature are also decisive physical entities. The stress exponent is of particular importance giving information on the dominant creep mechanism in the material investigated. Using a typical Norton-plot containing the double logarithmic representation of minimum creep rate and the constant applied stress, helps to determine the creep exponent graphically. Out of the graphic illustration of $\log\dot{\varepsilon}_{\mathrm{II}} = f(\log\sigma)$, the stress exponent can be found as the slope:

$$n = \frac{\Delta\log\dot{\varepsilon}_{\mathrm{II}}}{\Delta\log\sigma} \tag{2.8}$$
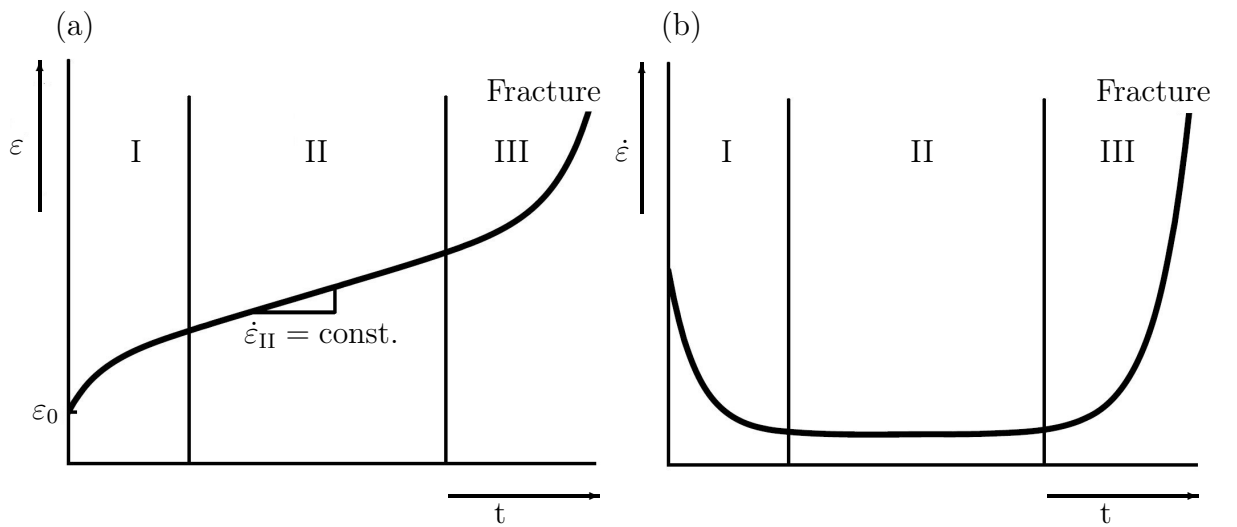
Figure 2.6: A schematic of (a) constant load creep curve and (b) strain rate plot versus time [80].

The creep exponent in a range of $3-8$ describes dislocation controlled creep, where vacancies enable a diffusion-controlled climbing of edge dislocations to overcome obstacles for dislocation movement. This creep mechanism dominates at elevated and high temperatures due to high vacancy concentrations. Typical creep curves of Mo-Si-B alloys usually show creep exponents of $3-8$ [22, 124], which means that for these ternary alloys predominantly dislocation controlled creep can be assumed. There are additional mechanisms that can also contribute to creep deformation. One of them is the diffusional creep (for $n \sim 1$ [15]) which is caused by a vacancy gradient between grain boundaries under tensile stresses and those ones undergoing compression. The vacancy migration may occur either as volume diffusion (Nabarro-Herring creep) at higher temperatures or along the grain boundaries (Coble creep) at lower temperatures. A third mechanism is the grain boundary sliding which contributes to creep deformation at very small grain sizes. The typical stress exponent for sliding of grains against each other is between 2 and 3 [80].

The activation energy Q of a creep process was calculated from the graphical representation of $\log \dot{\varepsilon}_{\mathrm{II}} = f(\frac{1}{\mathrm{T}})$, as described in [125].

$$Q = \frac{\Delta \log \dot{\varepsilon}_{\mathrm{II}}}{0.052 \Delta \frac{1}{\mathrm{T}}} \tag{2.9}$$

2.4 Oxidation behavior of Mo-Si-B alloys

Another significant feature that should be in balance with the mechanical properties is the oxidation behavior. Molybdenum suffers from poor oxidation resistance due to the formation and evaporation of MoO_3 at temperatures between $500\,^{\circ}\mathrm{C}$ and $800\,^{\circ}\mathrm{C}$ [23]. The addition of Si and B to Mo leads to the formation of intermetallic phases which enhance the oxidation resistance significantly. Working as a main reservoir for Si and B, those intermetallic phases oxidize at higher temperatures to a SiO_2-B_2O_3 glass layer which protects Mo alloys from further oxidation [112]. Especially SiO_2 is responsible for the good oxidation performance at temperatures above $1000\,^{\circ}\mathrm{C}$. The boron addition is important since B_2O_3 decreases the viscosity of the glass and helps to cover the materials' surface more quickly with a protective glass layer [126]. There are two main approaches for the oxidation/passivation performance of Mo-Si-B alloys which evaluate the role of viscosity and corresponding oxygen diffusion.

The model according to Parthasarathy et al. [23], points out, that diffusion is one of the main factors for damage. A summary of the oxidation mechanisms for Mo-Si-B alloys is illustrated in Figure 2.7. In the temperature range from $500\,^{\circ}\mathrm{C}$ to $600\,^{\circ}\mathrm{C}$, molybdenum trioxide (MoO_3) is formed and deposited as a layer on the materials' surface which leads to an increase of weight. At the same time, a SiO_2-B_2O_3 glass layer is formed, which impedes the oxygen diffusion to the base material, so that there is only a slight mass gain. At around $700\,^{\circ}\mathrm{C}$ a significant mass loss is observed due to the high porosity of the glass layer resulting in a loss of protective effect. The consequence is an almost complete damage of the material where only residues of the borosilicate glass layer remain which is also known as "pesting". According to this model, a continuous protective glass layer is build at temperatures above $800\,^{\circ}\mathrm{C}$. However, its viscosity is too low, due to an insufficient boron

|	500 °C - 600 °C	700 ± 50 °C	800 °C	900 - 1300 °C
Scale	B-Si-Mo-O	B-Si-O porous	B-Si-O	B-Lean Si-O
MoO_3	small loss	evaporates	transient evaporation and permeates out	transient evaporation
O_2	diffuses to the interface	diffuses to the interface	diffuses to the interface	diffuses to the interface
B_2O_3			begins to evaporate	evaporation at surface
				Mo, B diffuses out
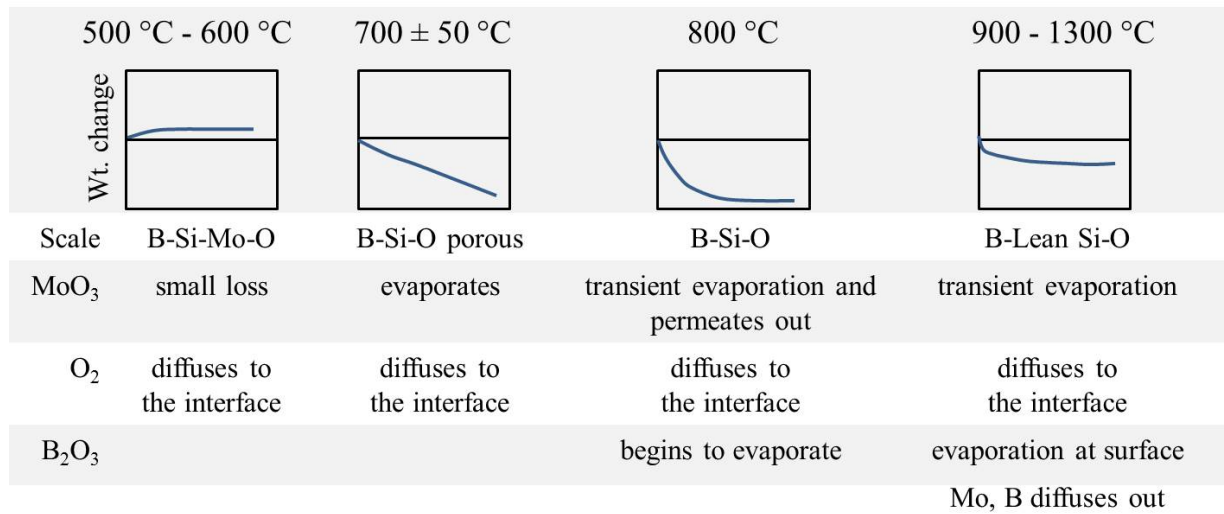
Figure 2.7: Oxidation mechanism map of Mo-Si-B alloys according to Parthasarathy [23].

amount, in order to hinder the permeation of MoO_3.

At temperatures above 1000 °C a continuous, protective and self-healing borosilicate glass layer is formed, which prevents from MoO_3 formation and volatilization. Hence, the low viscosity of the SiO_2 scale by fluxing with B_2O_3 is beneficial for a rapid surface coverage. However, soon after its formation B_2O_3 starts evaporating and therefore leads to a B-lean highly viscous glass scale with low oxygen diffusivity.

Another perspective was reported by Meyer et al. [37] investigating the passivation behavior of Mo-Si-B alloys. According to the scheme in Figure 2.8, two kinds of layers are distinguished: (A) a low viscosity scale forms initially with large pores and a large pore fraction and (B) a composition that initially forms a low porosity, high viscosity scale.

If the layer structure is coarse, the MoO_3 volatilizes at a temperature of approximately 800 °C, leaving a network of borosilicate glass with voids on the order of 10 mm in diameter which allow fast oxygen transport to the interface. This results in an increased partial pressure ($P_{O_2} \sim 20$ KPa) of oxygen and therefore volatilization of MoO_3 and SiO_2 so that rapid oxidation occurs. This process continues until viscous flow improves the filling of pores and forms a coherent oxide layer. After that, the only path for oxygen transport to the interface is by diffusion through the borosilicate layer, leading to a much smaller partial pressure of oxygen in the interface ($P_{O_2} \sim 5 \times 10^{-11}$ Pa). In case (B), a lower porous scale provides a better initial oxidation behavior, since the volatilizing MoO_3 leaves finer pores (0.1 µm) behind. The resulting porous borosilicate glass offers a much slower rate for oxygen transport to the interface providing a smaller partial pressure of oxygen (compared to case (A) at 800 °C). However, at 1000 °C viscous flow does not occur so that the oxygen diffusion kinetics remain relatively constant.

Thus, after Parthasarathy et al. [23], an increase of viscosity should lead to the prevention of pesting at 800 °C, whereas according to Meyer and co-workers [37], the viscosity should be further reduced in order to fill the pores. Middlemas [127] indicated that these assumptions only seem to contradict each other. Instead, a specific adjustment of the boron content (or in the further sense of viscosity) is necessary to obtain a protective glass layer.

Additionally, the oxidation processes in Mo-Si-B alloys strongly depend on the type and

volume fraction of intermetallic phases since the Mo_5SiB_2 phase is known to have a superior oxidation resistance compared to Mo_3Si [55]. Their homogeneous distribution and microstructural size also critically influence the oxidation behavior as well [128]. Therefore, microstructural inhomogeneities such as large Mo_{ss} particles or dendrites which typically result from ingot metallurgical processes should be avoided.

Since vanadium provides a high affinity for oxygen [129], its alloying to Mo-Si-B compounds might have a negative effect on their oxidation properties. Especially the formation of vanadium pentoxide (V_2O_5) is a critical aspect due to the network modifying effect which was reported by several authors.

Experiments by Mekki and co-workers [130] showed that small amounts of V_2O_5 in SiO_2-Na_2O glasses increase the count of non-bridging-oxygen (NBO) and thus reduces the layer viscosity. Further studies indicated that the function of V_2O_5 strongly depends on the concentration in the oxide layer. For example, at concentrations above 10% in P_2O_5-K_2O glasses, it acts as a network former rather than a network modifier [131].

Furthermore, Williams and Akinc [132] investigated the oxidation behavior of $V_5Si_3(B_{0.5})$ pointing out that the formed V_2O_5 starts melting at a temperature of approximately $700\,^\circ C$ and accumulating in open pores. As a result, the pores were not effectively filled, leading to unhindered oxygen diffusion to the base material. Additionally, it was mentioned that V_2O_5 leads to the formation of crystalline cristobalite within the glass scale forming a porous layer which reduces the oxidation resistance. This corresponds to studies carried out by Pércio et al. [133] pointing out that V_2O_5 in Li_2O-BaO-SiO_2 glasses acts as a strong nucleating agent and promotes devitrification.
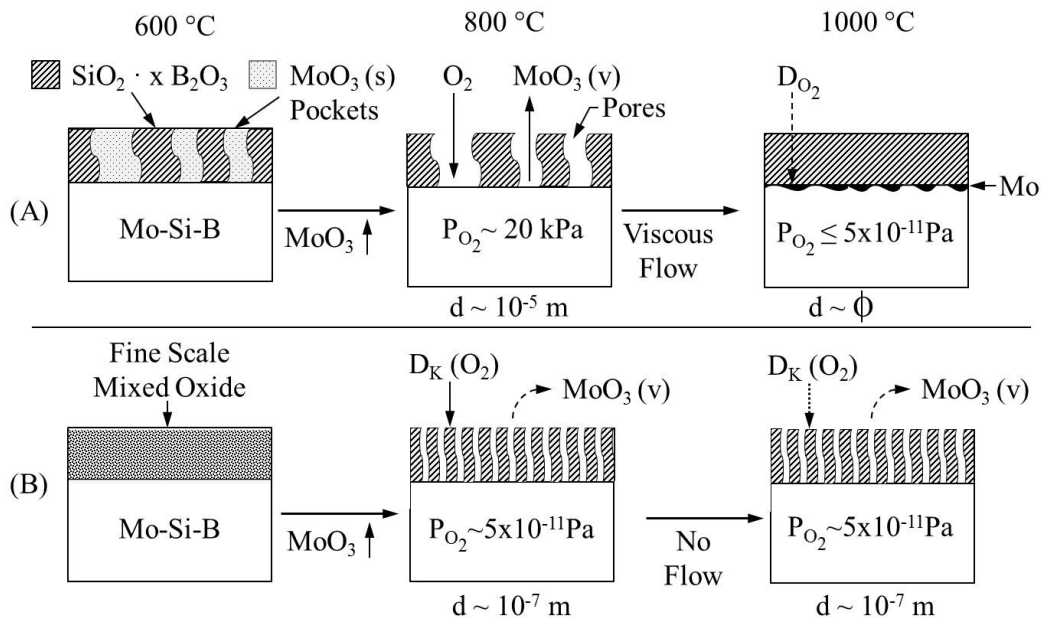
Figure 2.8: Schematic of oxidation process according to Meyer et al. [37] (A) for formation of porous (low density), low viscosity scale and (B) for formation of lower porosity, high viscosity scale, D_{O_2}: diffusion controlled oxygen transport, $D_K(O_2)$: oxygen transport by Knudsen diffusion or a similar process.

Studies by Sossaman et al. [134] and Kumar et al. [135] already confirmed the positive effect of Fe on the oxidation performance of Mo-Si-B alloys. Basically, Sossamann and co-workers assumed that substitution of Mo by $0.05\,\text{wt.\%}$–$1.35\,\text{wt.\%}$ Fe in a Mo-2Si-1B alloy results in a network modifying effect which offers a clear increase of NBO's. Out of the enhanced fluidity of borosilica, an oxidation kinetics model was developed for Mo-Si-B alloys with Fe additions that can be extended to other oxidation-resistant refractory metal systems.

Beside the formation of NBO's, Kumar and co-workers [135] reported another effect of Fe where minor additions of Fe refined the microstructures of $Mo_{76-x}Si_{14}B_{10}Fe_x$ ($x = 0, 0.5, 1\,\text{at.\%}$). Additionally, the inclusion of Fe in the A15 phase increased the amount of Si available for phase formation and lead to an increase ($9\,\%$) of the A15 phase. This caused an improved formation of silicate glass on the materials' surface and thus prevented the loss of material in the critical oxidation phase (around $800\,°\text{C}$).

3 Materials and methods

3.1 Alloy preparation

3.1.1 Powder metallurgy

As explained in Chapter 2.1 different processing routes can be used to prepare Mo-Si-B alloys with varying microstructures. The powder metallurgy is an ideal manufacturing technique for refractory metals which provides very homogeneous microstructures in the laboratory scale but also in larger scales. The step of mechanical alloying (MA) at ambient temperatures provides an energy-efficient process which allows to combine elements with low and high melting points [65]. First the powders have to be weighed in to their mass fractions respectively which were determined after following Equation 3.1 [136].

$$m_{\mathrm{x}} = \frac{A_{\mathrm{x}}\, X_{\mathrm{x}}}{\sum_{i=1}^{n} A_i\, X_i} \tag{3.1}$$

For this purpose, Mo (purity $99.95\,\%$), V ($> 99.9\,\%$) Si and B powders (both $99.9\,\%$) were weighed and mixed under protective argon atmosphere. The next step of mechanical alloying was performed in a planetary ball mill (Retsch® PM 400, Haan, Germany - Figure 3.1 (a), which provides an efficient energy transfer compared to other usual milling components (e.g. attritor or vibratory mill). Due to the superposition of centrifugal and Coriolis force this mechanical alloying process is also called the high-energy milling involving various states of motion like rolling (cascade movement), falling (cataract movement- Figure 3.1 (b) and the centrifuging of balls [137]. The impact of balls and additional friction during the cataract movement generate the highest energy transfer and were therefore the leading mechanisms for mechanically alloying. Affecting a repetitive breaking and rewelding of powder particles, this process results in a homogenization on atomic level.

Therefore the powder mixtures were filled in grinding tools including stainless-steel balls ($d = 10\,\mathrm{mm}$) at powder-to-ball ratio of $1:14$. The closed grinding tools were then fixed within the planetary ball mill which works with a rotational speed of 200 rpm for 30 h. These parameters have already been well studied and established for Mo-Si-B alloys [17] so that they could be transferred for the present Mo-V-Si-B System.

As a result of this process a V, Si and B supersaturated Mo solid solution was formed. Finally, in order to eliminate the pre-induced stresses and induce phase transformations, a thermal treatment was carried out. In ceramic boats the loose powders were annealed at $1300\,^{\circ}\mathrm{C}$ for $5\,\mathrm{h}$ under argon atmosphere.
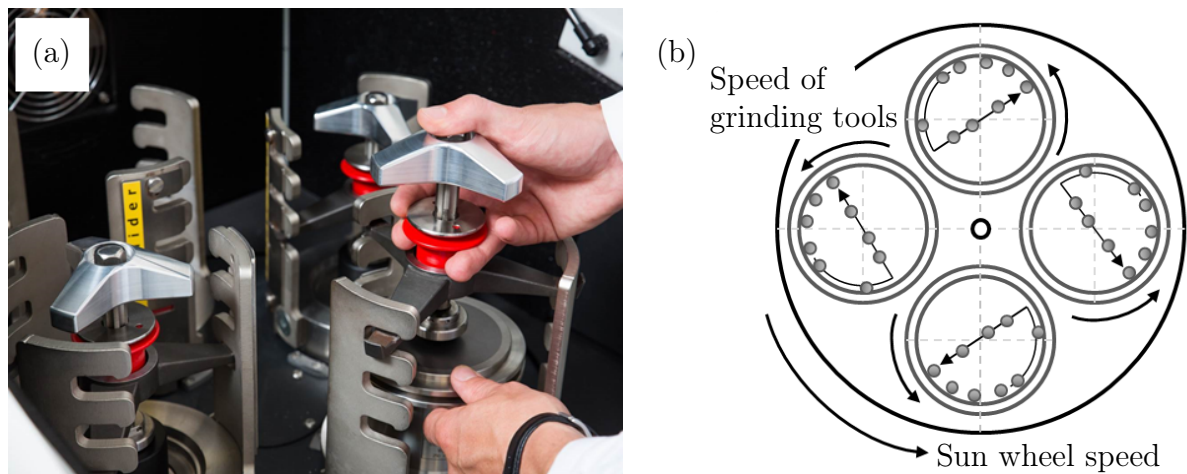
Figure 3.1: Planetary ball mill (a) while fixing of grinding tools (IWF, Otto-von-Guericke-University Magdeburg) and (b) schematic of cataract movement during milling process according to [65].

Field assisted sintering technology (FAST)

The analysis of the thermally treated powders provides a first impression for the resulting microstructures. In order to understand the micro-macro-interactions of the present alloying system, the characterization of macroscopic properties is also very important.

To investigate the effects of vanadium alloying on the mechanical properties of Mo-9Si-8B, mechanically alloyed Mo-40V-9Si-8B powder was chosen for processing via the field assisted sintering technology (FAST) to achieve bulk Mo-40V-9Si-8B material. This procedure was provided by the Karlsruhe Institute of Technology (KIT), Karlsruhe, Germany.

As shown in Figure 3.2, the mechanically alloyed powder filled into a graphite die and punch unit, was directly heated using a direct current (DC) via the Joule effect. Passing the pulsed electric current through the graphite die results in a partial heating and formation of electric field at the grain boundaries. Thus sintering necks are formed resulting in fusion of the particles [138]. Additionally, the simultaneous application of a uniaxial mechanical pressure enhances densification. Another advantage is the comparatively short process time in relation to the hot isostatical pressing (HIP) in which the heating occurs from the outer areas of the sample. In contrast, the uniform heat distribution during FAST ensures a homogeneous as well as fine-grained microstructure making this technology also suitable for larger sample geometries.

Heating rate of 100 $\frac{K}{min}$ and holding times of 15 min at 1100 °C and 1500 °C were used for processing. The whole process was performed under vacuum ($P < 10$ Pa) and uniaxial pressure of 50 MPa. Samples for examination by scanning electron microscopy (SEM) and thermomechanical investigations were prepared from the sintered buttons (diameter 30 mm, height 9 mm) by electrical discharge machining (EDM). A part of these samples were thermally treated at 1600 °C for 10 h (at KIT) in order to create a coarser microstructure which is supposed to be beneficial in terms of creep resistance.
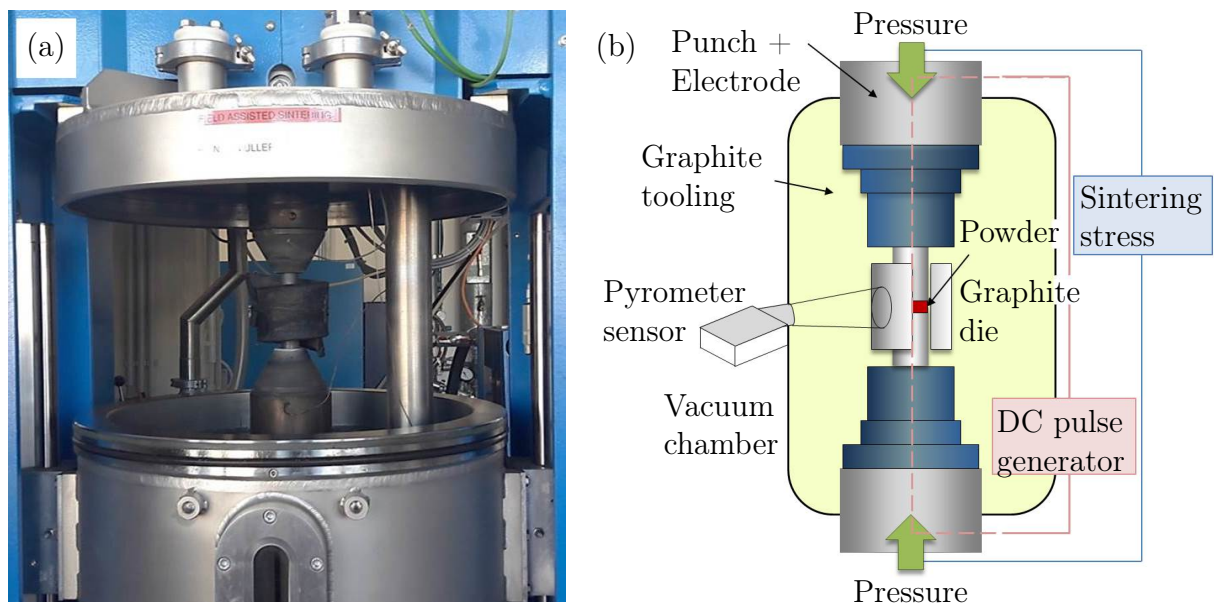
Figure 3.2: Experimental setup for field assisted sintering technology (FAST) at the Karlsruhe Institute of Technology (KIT), Karlsruhe, Germany (a) structure of the manufacturing plant (b) schematic structure according to [138].

3.1.2 Arc-melting

In contrast to the phase formation out of the supersaturated solid solution, the ingot metallurgical processing forms phases during solidification out of the melt. Reaching high melting points for present refractory alloys the ingot metallurgy by arc-melting (Arc) is a suitable technique which is predestined to produce samples on a laboratory scale. It is a comparably easy way to produce a large number of different alloy compositions by using only small badges of raw material. A huge advantage for this kind of ingot metallurgy is the easy handling. In principal the arc-melter consists of a furnace chamber attached to a power supply system, a vacuum pump and gas supply system. The process starts with the evacuation of the chamber and purging several times with a low pressure Ar atmosphere. As shown in Figure 3.3, in order to start, the raw materials were placed inside the furnace chamber on a water-chilled copper crucible. Melting was then carried out via the arc ignited by a tungsten cathode which is controlled by a manipulator. Prior to each melting step a pure zirconium sample was melted to remove residual oxygen.

Usually 2.5 g samples were molten to investigate the microstructures and chemical compositions but also to prepare specimen with dimensions of 2 mm x 2 mm x 3.5 mm for creep and oxidation tests by EDM. To receive samples for fracture three-point bending tests, buttons of minimum 15 g were used for extensive materials characterization.

The binary Mo-5X (X = Ti, V, Zr) as well as the Mo-V-Si-B alloys were fabricated via conventional arc-melting of metal sheets in argon atmosphere employing a Buehler AM0.5 arc-melter. For the second mentioned alloy systems, the pure metal sheets with purities of 99.95 % for Mo, 99.9 % for V as well as Si and 99.5 % for B were cut into flakes and mixed to obtain the target alloy composition. After flipping and remelting five times the samples
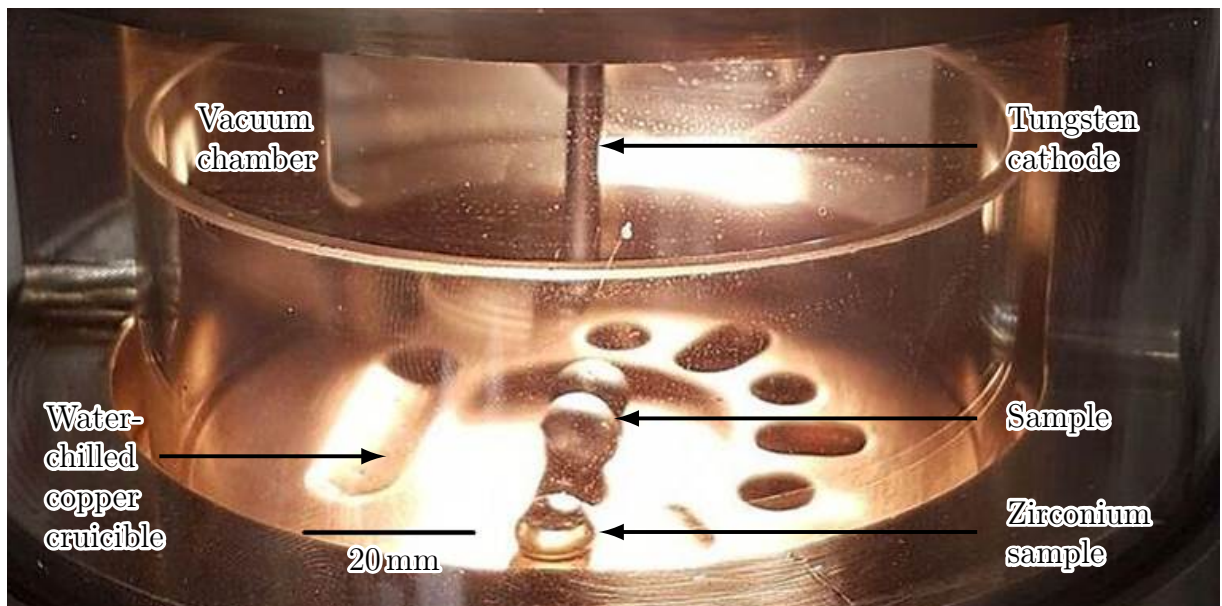
Figure 3.3: Experimental Setup for Arc-Melting (IWF, Otto-von-Guericke-University Magdeburg).

solidify typically drop-shaped. The technique for 15 g buttons production as well as for inductively coupled plasma optical emission spectroscopy (ICP-OES) to verify the chemical composition was provided by Forschungszentrum Jülich, Jülich, Germany. The high cooling rates of the arc-melting process generate disequilibria conditions during consolidation. Therefore, the ingots were subsequently homogenized in an argon atmosphere (tube furnace HTM Reetz GmbH Typ Losic) for 24 h at 1400 °C. Finally the samples were prepared using EDM .

3.2 Metallographic preparation and microstructure characterization

The density is a decisive reference value for the alloys studied here. So first of all, before metallographic preparation, the density of compact specimen was determined using Archimedian method. For this purpose, the weight was first measured in air and then in water using a hydrostatic balance (Satorius Cubis®, Satorius AG, Germany). Subsequently, the volume and, in turn, the density of the sample were calculated via its displacement. Analyzing the microstructure is very essential for understanding the materials' behavior. Therefore different preparation techniques and analytical methods can be used, depending on the dimension of microstructural constituent. A first impression of microstructure can be obtained using an optical microscope offering a maximum of 2000 times magnification and a limit of resolution to 1 μm. After getting a first orientation regarding microstructural constituents a higher resolution range is needed to observe the microstructure more detailed. The scanning electron microscopy offers expanded opportunities to investigate the micro-

and submicrostructure of materials.

The preparation starts with embedding the loose powders or the compact samples cut by EDM either in a hot mounting polymer (Struers PolyFast) or cold harden epoxy (Technovit 4071, Heraeus Kulzer, Germany). After subsequently wet-grinding using 500, 800, and 1200 grit SiC paper, the specimen were finished by polishing with a $3\,\mu m$ and $1\,\mu m$ diamond suspension as well as a collodial silica suspension (OPS with NH_3 and H_2O_2 additions). If necessary the samples were etched using a solution made of $20\,ml$ hydrofluoric acid (HF - $40\,\%$), $20\,ml$ nitric acid (HNO_3 - $65\,\%$) and $50\,ml$ sulfuric acid (H_2SO_4- $95\,\%$). This etching solution particularly affects the intermetallic phases creating a clear contrast to the Mo solid solution phase.

Scanning electron microscopy

The microstructure observations were conducted by using a scanning electron microscope (SEM - FEI ESEM XL30 FEG) equipped with EDS (energy dispersive X-ray spectroscopy). The SEM offers two kinds of contrasting modes. In the secondary electron (SE) contrast the electrons are emitted from a very thin surface layer and are easily depicted by a collector field due to their low energy ($E_{SE} < 200$ eV) [139]. Their emission has a high signal-to-noise ratio which makes it predestined for imaging surface topologies. So the SE contrast was used to depict fracture surfaces of specimen after three-point bending. The backscattered electrons (BSE) reveal comparably higher energies which are close to the primary beam energy. The intensity of BSE signal increases with the electron count, resulting in a material contrast image where heavy and light elements are separated via different gray scales [139]. In order to distinguish the individual phases, SEM images for microstructure investigations were typically obtained in the BSE mode with an acceleration voltage of $25\,keV$.

The additional EDS technology allows the analysis of chemical composition of individual microstructural components. Atoms excited by the electron beam emit an element-specific X-ray radiation pattern which is collected simultaneously via a semi-conductive detector, amplified and counted in a multichannel analyzer. After relatively short scanning times a qualitative and quantitative (except e.g. B, C, N and O) evaluation of components is obtained [140].

Investigating very fine microstructures like for alloys produced via FAST, the EDS measurements can be affected by the radius of electron beam and the interaction with surrounding phases which provide inaccurate results for phase analysis. An alternative way for spatially resolved phase analysis can be realized using electron backscatter diffraction (EBSD). This method is based on the inelastic scattering of the electrons hitting the lattice planes at the Bragg's angle. The backscattered electrons describe Kikuchi patterns which provide information about crystal structure, orientation, and stresses. Subsequently evaluation of these patterns and their comparison with databases offers the possibility of phase identification. Additional combination of EBSD with EDS is a powerful tool for phase identification. A direct correlation of the chemical (EDS element mapping) and structural (EBSD mapping) information allows unambiguous identification of the present phases [141]. Electron backscatter diffraction (EBSD) analysis was performed to identify the crystal

structure using a Zeiss Merlin SEM equipped with a Nordlys EBSD camera and Aztec software package (Oxford Instruments) provided by the Forschungszentrum Jülich, Jülich, Germany.

Quantitative microstructure analysis

Using those imaging methods described above, a high-quality evaluation of the microstructures was possible. The assessment of phase distribution and fraction was carried out by using the software ImageJ. This program is able to define the percentage proportion of each phase by distinguishing different gray scales. Since the microstructures do not differ in their longitudinal and transversal direction, the individual area proportions of phases can be interpreted as volume fractions. An evaluation was performed on five images per alloy using a magnification of 1500 x especially for Mo-5Zr and 5000 x for Mo-(V)-Si-B alloys.

The micrographic determination of the apparent grain size was carried out by means of linear intercept method according to DIN EN ISO 643 [142]. For this purpose, several horizontal lines of the same, defined length (L) are positioned on the microstructural image for counting and averaging the number of intersections with the grains ($\bar{N}$). Subsequently, the following Equation 3.2 is used to describe the average number of grains per line.

$$\bar{N}_{\mathrm{L}} = \frac{\bar{N}}{L} \tag{3.2}$$

Finally, the reciprocal value of $\bar{N}_{\mathrm{L}}$ describes the dimension of average grain size ($\bar{d}$).

3.3 X-ray diffraction analysis (XRD) and Rietveld method

In addition to the chemical composition, the structural properties of the phases involved also play a major role for material characterization. This can be realized using the X-ray diffraction analysis (XRD) where the X-ray photons are scattered by the atoms in a periodic lattice. The resulting diffraction pattern can be described by the Braggs' Equation 3.3 [143].

$$sin\,\theta = \frac{\lambda}{2\,d_{\mathrm{hkl}}} \tag{3.3}$$

θ is half the angle between the diffracted beam and the original beam, λ is the wave length of the X-rays and d_{hkl} is the interplanar spacing between the planes that caused constructive interference of the beam. The phase identification was realized via powder X-ray diffraction (XRD) measurements using an X'Pert X-ray diffractometer (PANalytical) with Bragg-Brentano geometry and Co - $K_{\alpha1,2}$ radiation ($\alpha_1 = 1.789$ and $\alpha_2 = 1.793$). Measurements were exclusively performed on powders using the backloading preparation. Especially for the compact specimen from FAST and arc-melter fabrication, samples taken

via EDM were processed into powder using mortar and pestle. In order to get a high quality measurement the usual scanning time took about 8 h. The times per step of 500 s in the scanning range of $20° - 140°$ ensure a high accuracy which qualifies the measurement for quantitative phase analysis using Rietveld method.

Rietveld method

The crystal structure analyses via the Rietveld method for the present alloys were carried out by Dr. rer. nat. Ulf Betke (Otto-von-Guericke-University Magdeburg, Institute of Materials and Joining Technology).

First identification of phases was obtained using the X'Pert HighScore Plus software by PANalytical. A quantitative phase analysis was then performed by means of the Rietveld method using the Topas Academic V5 program package (A.A. Coelho, Topas Academic V5, Coelho Software) and the crystal structures of Mo, Mo_3Si, and Mo_5SiB_2 as starting parameters. The instrumental contribution to the reflection profile was described by the fundamental parameters approach. The X-ray tube emission profile, axial beam divergence, and slit contributions were refined using a Pawley fit to a LaB_6 reference sample diffractogram (10 μm grain size; Sigma-Aldrich, Germany) then fixed in the Rietveld analysis of the respective specimen.

For each sample, Rietveld refinement global background coefficients, the zero-shift error, and one thermal displacement parameter for all atoms in all phases were refined. For each phase, a set of cell parameters, the phase fraction, and a parameter ε_0 describing the microstrain in the respective phase were introduced. For $(Mo,V)_5SiB_2$ phase, the atomic coordinates for the metal site 16 l and the boron atom were refined, whereas all other positions, also for the $(Mo,V)_3Si$ and $(Mo,V)_{ss}$ phases, were consequently fixed. For each phase, mixed occupancy by vanadium and molybdenum was introduced for the respective metal sites. The results of occupancy consideration were visualized using the molecular and crystal structure visualization software Diamond (Crystal Impact GbR, Bonn, Germany). The Mo/V ratio was refined separately for each phase, allowing detailed analysis of its vanadium content. Finally, the alloy composition was recalculated in vol. % using the weight percentage and crystallographic density values obtained by the Rietveld method for each phase. Furthermore the lattice parameters of the alloys investigated were determined.

3.4 Powder characterization

In order to evaluate the quality of specimen sintered via FAST, a characterization of powder in its original state and after mechanical alloying is helpful. The determination of particle sizes is useful to evaluate the mechanical alloying process and if necessary to adjust milling parameters. Therefore the linear intercept method (as explained in Chapter 3.2, page 31) was used to characterize the average particle size. For this purpose, images of embedded, ground and polished powders are used. In contrast of observing whole microstructures, in

this case it is necessary to subtract the distances between the powder particles from the measuring length to obtain the real range. Using this method the grain diameter can be underestimated ($\approx 0.79\,d$) due to preparation [65]. However, in the present thesis this fact is negligible because the particle sizes were only used for comparison of powders with each other.

A more decisive value for a satisfying sintering result is the oxygen concentration. The oxygen impurity concentration of the present alloys was determined via the hot gas extraction technique using a Bruker ON/H-mat286 analyzer which is designed to handle compact samples. Therefore, the milled and thermally treated powders had to be filled into Ni capsules (each with 30 mg powder) under argon atmosphere. Three samples were measured for each alloy composition under helium atmosphere for 45 s to 60 s.

3.5 Density functional theory (DFT) simulation

In order to get a better understanding for the phenomena of crystal site occupations, which resulted from Rietveld refinement, DFT calculations were carried out by Dr. rer. nat. Rachid St. Touzani (Otto-von-Guericke-University Magdeburg, Institute of Materials and Joining Technology).

The density functional theory (DFT) is a many body particle theory where the electron density and not the wave function is used to determine the electronic and energetic properties of atoms, molecules and solid state materials. For this purpose the famous Schrödinger equation is replaced by the Kohn-Sham equation with a suitable exchange correlation functional. This approach is an excellent alternative for mostly not available solutions of the Schrödinger equation [144].

In this work, DFT was used to investigate the occupation of V within the participating phases. Special attention was paid to the crystalline structure of T2 phase $V_y Mo_{5-y} SiB_2$ with $y = 0, 1, 2, 3, 4, 5$.

For $Mo_5 SiB_2$, $VMo_4 SiB_2$, $V_4 MoSiB_2$ and $V_5 SiB_2$ the conventional unit cell as starting model was used, while for $V_2 Mo_3 SiB_2$ and $V_3 Mo_2 SiB_2$ a $2 \times 2 \times 1$ supercell and special quasirandom structures (SQS) to model the 50 % V/50 % Mo occupation on the Wyckoff position 16 l were chosen.

First-principles calculation were carried out with Quickstep [145] as implemented in the CP2K version 5.1 program [146] package for the structural relaxation of the $V_y Mo_{5-y} SiB_2$ ($y = 0, 1, 2, 3, 4, 5$) solution using the Gaussian plane wave method (GPW) [147], for Mo, V, Si, and B the DZVP-MOLOPT-SR-GTH basis set [148] and GTH-pseudopotentials were chosen [149–151].

The kinetic energy cut-off of the plane waves were set to 600 Ha and the structural relaxation were stopped until a total energy convergence of 10^{-8} Ha and a force convergence of $10^{-6}\,\frac{Ha}{a_0}$. The k-mesh was divided by $9 \times 9 \times 5$ for $Mo_5 SiB_2$, $VMo_4 SiB_2$, $V_4 MoSiB_2$ and $V_5 SiB_2$, while for $V_2 Mo_3 SiB_2$ and $V_3 Mo_2 SiB_2$ the k-point grid was $4 \times 4 \times 5$. Exchange and correlation in this DFT-based method were treated with the generalized gradient approximation (GGA) functional as parameterized by Perdew, Burke and Ernzerhof (PBE-GGA) [152].

The chemical bonding analysis was carried out using the tight-binding, linear muffin-tin orbitals with the atomic spheres approximation (TB-LMTO-ASA) [153,154] as implemented in the TB-LMTO 4.7 program. Exchange and correlation were treated with the PW91-GGA functional by Perdew et al. [155]. The k-mesh was chosen to be $15 \times 15 \times 15$ for Mo_5SiB_2, VMo_4SiB_2, V_4MoSiB_2 and V_5SiB_2, while for $V_2Mo_3SiB_2$ and $V_3Mo_2SiB_2$ the k-point grid was $4 \times 4 \times 4$.

The bonding analysis was performed by calculation of the density-of-states (DOS), the crystal orbital Hamilton population (COHP) and its integrals (ICOHP). The ICOHP can be seen as a semi-quantitative bonding energy which measures covalent contribution in solids. Plotting the population shows negative COHPs for antibonding states, positive ones for bonding states and non-bonding states having COHPs of zero. The Fermi level (E_F) was set to 0 eV.

3.6 Mechanical properties

3.6.1 Microhardness testing

Measuring the hardness of a material is an easy and effective way to get a first impression of the mechanical properties at room temperature. Taking into account the small dimensions of samples available, the microhardness testing offers a good potential to determine representative values for microstructure hardness. Microindentation referred to DIN EN ISO 6507 - 1 [156] was conducted by indenting a Vickers pyramid with a force of 0.1 N (HV 0.01) and a hold period of 5 s. The measurements were performed by generating a series of 30 indents set within the material at well-defined intervals to avoid the influence of dislocation pile-up between the indents and grain boundaries as well as neighboring indents. The minimum interval between the center of neighboring indents as well as the distance between indent and grain boundary should be the threefold of indents diagonal length. The indents were performed using the automatic microhardness tester Wilson® VH3300 (Buehler) equipped with the software DiaMet™ for direct and easy evaluation of hardness values. The Vickers hardness is calculated via the projection left by the Vickers indenter having included angles of $136°$ after the following equation

$$HV = 0.102 \, \frac{F_i}{A_{HV}} = 0.102 \, \frac{2 \, F_i \, sin\left(\frac{136°}{2}\right)}{d_{HV}^2} \approx 0.1891 \, \frac{F_i}{d_{HV}^2} \tag{3.4}$$

where F_i is the indentation load and A_{HV} is the projected indent area, which is described by the pyramid's diagonal d_{HV} [156].

3.6.2 Fracture toughness - Notched beam method

Executing a material characterization not only means an evaluation of strength and elongation limit but also to look at the materials' failure. Microstructural inhomogeneities

or defects provoke crack formation which leads to failure due to crack propagation during cyclic loading [80]. Critical aspects concerning the present alloys are high amounts of brittle intermetallic phases with low room temperature fracture toughness ($\sim 2-3\,MPa\sqrt{m}$) [49, 50] and intrinsic stresses after solidification (especially after arc-melting) as well as high porosity after sintering (FAST).

There are three different types of crack deformation: the opening mode, the sliding mode and the tearing mode. While the sliding and tearing mode are less considered here, the opening mode (mode I) describes the crack opening perpendicular to its surface and is therefore the most significant for practical application. Its assessment occurs via the stress intensity factor (K_I), which indicates the intensity of the stress field in the vicinity of a crack tip. It depends on the external load as well as the geometry of the crack and the component. The stress intensity factor at which crack propagation begins and, finally, breakage occurs represents the critical stress intensity factor (K_Ic), which is also known as fracture toughness [157].

In this regard, reliable values can be determined by means of linear elastic fracture mechanics (LEBM). This method applies specifically to notched specimen sharpened by fatigue cracking. For Mo-Si-B alloys, cyclic loading for inducing fatigue cracks is not trivial, since a brittle behavior is assumed due to high amounts of intermetallic phases. Hence, the material's failure can already occur during preparation. Since the brittleness of intermetallic phases corresponds to those of ceramic materials [158], the evaluation of fracture toughness was based on DIN EN ISO 23146 [158], which deals with test methods for fracture toughness of monolithic ceramics.

The experimental procedure was performed by the notch beam method, which was already used for characterization of Mo-Si-B alloys, e.g., by Schneibel et al. [68]. Firstly, the ground and polished bending specimen with dimensions of $2\,mm \times 2\,mm \times 18\,mm$ were provided with an EDM-machined prenotch. The notch geometry exhibited depth of 0.8 mm and width less than $0.2\,mm$, according to the requirements of DIN EN ISO 23146. A "sharp crack" with typical depth of $200\,\mu m$ and tip radius of around $10\,\mu m$ was produced using a self-built cutting device (Figure 3.4 (a)) equipped with a razor blade working with $1\,\mu m$ diamond paste. In order to control the notch depth and tip-radius, the samples (fixed on the monut with epoxy) were examined at defined intervals ($15-20\,min$) using an optical microscope (OM). Fracture toughness measurements were then performed using a minimum number of five samples having similar notch base radius of around $10\,\mu m$. Three-point flexure was realized as shown in Figure 3.4 (b) using a microtest cell (Materials Testing Nano Tomography Version 3.2, Deben) with maximum load of $500\,N$. The tests were performed in air at ambient temperature with load rate of $0.5\,\frac{mm}{min}$ under preloading with $2\,N$. According to standard [158] the fracture toughness was determined as K_Ic value using the following equation:

$$K_\mathrm{Ic} = \frac{F_\mathrm{f}}{B\sqrt{D}}\,\frac{S_1}{D}\,\frac{3\,\sqrt{\alpha}}{2\,(1-\alpha)^{\frac{3}{2}}}\,Y^* \tag{3.5}$$

where F_f is the fracture load in, B is the sample width, D is the sample depth, S_1 is the support span, α is the relative notch depth, and Y^* is the stress intensity shape factor, approximated by:

$$Y^* = 1.964 - 2.837\,\alpha + 13.7714\,\alpha^2 - 23.250\,\alpha^3 + 24.129\,\alpha^4. \tag{3.6}$$
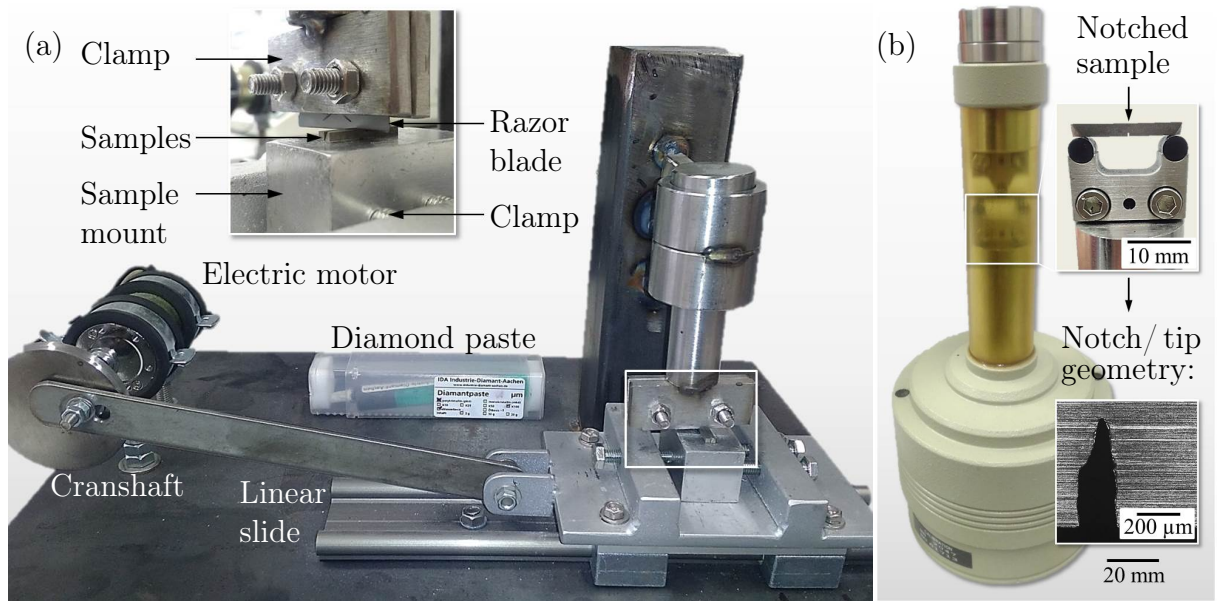
Figure 3.4: Experimental setup (a) for notching of specimen: simple reciprocating machine with moving samples including detail of the clamp for a razor blade and (b) for testing of three-point bending in the microtest cell including detail of the razor notch geometry.

Therefore Y^* is the stress intensity shape factor for three-point flexure using a 15 mm span and sample depth of 2 mm ($\frac{S_1}{D} = 7.5$) [158].

3.6.3 Mechanical testing from RT up to elevated temperatures

The mechanical properties, including bending, compression and creep tests, were conducted using a Zwick/Roell Z100 electromechanical testing machine equipped with a Maytec furnace working in a range from room temperature up to 1200 °C. The high temperature experiments were performed in a flowing Ar/H_2 atmosphere to avoid oxidation. Bending tests were performed in order to determine the brittle-to-ductile transition temperature. Therefore, the specimens with a geometry of 2 mm x 2 mm x 30 mm were placed on a three-point bending device having a bearing span of 25 mm and tested in a regime of 800 °C – 1100 °C with a constant traverse velocity of 0.01 $\frac{mm}{min}$.
The stress profile for those tests is visualized in Figure 3.5. For only identifying the critical temperature, the elastic-beam-theory, which does not consider the plastic strain, can be used for calculation of stresses and elongations of the tensile loaded outside fiber. The maximum bending moment M_b can be calculated by connecting the bending load F_b and bearing distance l_s as shown in the following equation [159].

$$M_b = \frac{F_b \, l_s}{4} \tag{3.7}$$
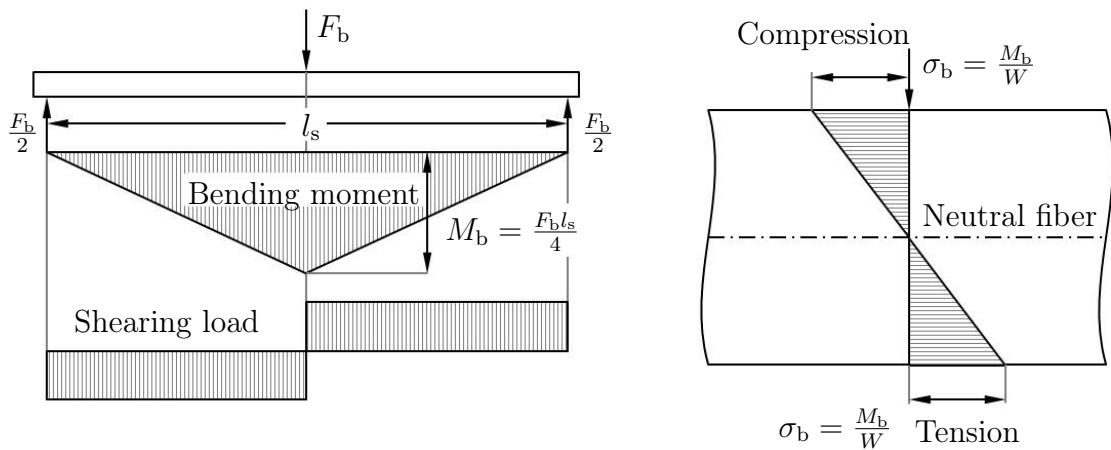
Figure 3.5: Bending test in three-point loading.

The estimation of bending stress results from the quotient of bending modulus M_b and section modulus W including the sample geometry (b_s, h_s).

$$\sigma_b = \frac{M_b}{W} = \frac{3\,F_b\,l_s}{2\,b_s\,h_s^2} \tag{3.8}$$

Additionally the outer fiber strain ε_f results from the following equation establishing the correlation to the measured deflection f [160].

$$\varepsilon_f = \frac{6\,f\,h_s}{l_s^2} \tag{3.9}$$

In order to distinguish the elastic from the plastic behavior, a plastic strain of $0.2\,\%$ was assumed.

Performing uniaxial compression tests is a comparably a classical way to assess material properties at ambient and elevated temperatures. The mechanical behavior was determined by constant displacement tests at a nominal strain rate of $1 \cdot 10^{-4} \text{s}^{-1}$ in uniaxial compression at room temperature (RT), $800\,°C$ and $1100\,°C$. Therefore specimens with dimensions of $2\,\text{mm} \times 2\,\text{mm} \times 3.5\,\text{mm}$ were prepared by EDM. The compressive yield stresses were measured by the $0.2\,\%$ offset method.

In order to asses the creep properties of present alloys, creep tests were performed on rectangular specimens with dimensions of $2\,\text{mm} \times 2\,\text{mm} \times 3.5\,\text{mm}$ at $1093\,°C$ ($\equiv 2000\,°F$ for comparative purposes) under constant applied stress of $50\,\text{MPa}$, $80\,\text{MPa}$, $100\,\text{MPa}$, $150\,\text{MPa}$ and $200\,\text{MPa}$. After attaining a steady secondary creep rate at a particular constant stress level, the stress was increased until a further steady-state was established.

3.7 Cyclic oxidation experiments

With regard to the focused application in high pressure turbines, beside the good creep properties the present alloys also should exhibit an acceptable oxidation resistance at elevated temperatures. Cyclic oxidation tests provide an excellent imitation of real conditions

allowing an assessment of the oxidation behavior. Therefore the exposure of samples in static air at certain temperatures is typically carried out at defined cycles. The exposure times per cycle were 10 min during the initial stage (< 1 h) and were subsequently increased to 1 h cycles up to 20 h, followed by 5 h cycles up to 50 h and 10 h cycles until the final 100 h of total oxidation exposure is reached [23].

Those experimental procedures were performed under static air in a box furnace (Thermconcept HTL04/18) at 800 °C, 1000 °C and 1150 °C. Before starting the oxidation exposure sample's initial weight and dimensions were exactly determined. Their geometry was adopted from the mechanical tests, so in general rectangular specimen with dimensions of 2 mm x 2 mm x 3.5 mm were oxidized.

At the end of each cycle the samples were removed from the furnace, cooled down to room temperature under atmospheric conditions and carefully weight to determine their weight loss after certain exposure times. Afterwards the sample was re-exposed to the particular temperature described above. The specific mass change was carefully measured using an analytical balance with an accuracy of 0.0001 g.

Due to a rapid mass loss during the 1 h cycles, the exposure times were adjusted to 1 h steps up to 5 h, followed by 5 h steps up to 20 h. The reduction of cooling steps therefore should lead to a lower stressing of the sample. Nevertheless, sometimes it was necessary to break up the tests before completing all oxidation steps. Otherwise, progressive sample damage would have made microscopic evaluation difficult or impossible.

In order to gain a better understanding of the oxidation processes, the microstructural features of the oxidized samples were studied via SEM and XRD. Additionally a Zeiss stereomicroscope was used to record the surface condition photographically. The resulting weight change curves were plotted vs. the exposure time and the results for present alloys were compared to other Mo-Si-B alloys described in literature.

4 Experimental results and discussion

Chapter 2 showed that the Mo-Si-B system offers a wide range of opportunities. Especially the combination of elements to get an optimized microstructure with balanced properties is challenging. As explained before, vanadium is a promising element to effectively reduce the density of Mo-Si-B compounds but also in order to benefit the mechanical properties at room temperature and even at high temperatures. The present chapter describes how V affects the properties of binary Mo-based alloys and, in particular, the favored alloy Mo-9Si-8B. It shows the advantages and disadvantages of alloying with V and finally gives an assessment of whether V is actually a promising alloying partner, as initially expected.

4.1 Alloying effects in Mo solid solutions

Since Berczik [19, 20] pointed out the importance of a high volume fraction (around $50\,\%$) of continuous Mo_{ss} phase, which significantly effects the alloys properties, the impact of V on the characteristics of this microstructural constituent is of preliminary interest. Previous research on Mo-Si alloys [28, 29] already demonstrated that dissolving additional elements in the Mo_{ss} phase affects its fracture toughness, ductility and strength as well as the density of Mo alloys.

In the following, the effects of V on the strength and ductility as well as the density of a Mo_{ss} will be assessed and compared to the impact of other alloying partners like Ti and Zr. However, no systematic investigations were carried out so far regarding the influence of higher concentrations of those promising elements (Ti, Zr, V), beyond the results described in Chapter 2.2 (page 12), on the microstructures and mechanical properties of binary Mo alloys from room temperature up to possible application temperatures of $1100\,°C$ e.g. as gas turbine blades.

Therefore, the focus was set on Mo-5X (X = Ti, Zr, V) alloys in terms of solubility of alloying additions in the Mo_{ss} phase and the accompanied solid solution strengthening, the tentative second phase formation, the microhardness and the deformation behavior in the compressive mode between room temperature and $1100\,°C$.

4.1.1 Microstructural features of Mo-5X alloys

The microstructures of the as-cast (via Arc) and thermally treated (TT at 1400 °C for 24 h) Mo-5X alloys were observed via OM and SEM coupled with EDS analysis. According to the phase diagrams (illustrated in the Appendix, page 85 ff.) showing a maximum solubility of about 12 at.% Ti in Mo and complete solubility of V in Mo, the alloys Mo-5Ti and Mo-5V exhibit a single-phase microstructure (Figure 4.1 (a) and (b)). Although the samples were processed in a similar procedure (section 3.1.2) the resulting microstructures differ from each other. A typically coarse microstructure due to ingot metallurgical processing is provided by alloys Mo-5Ti and Mo-5V with an average grain size of 943 µm and 570 µm, respectively (Table 4.1).

Indeed, the Mo-5Zr alloy shows a two-phase microstructure, Figure 4.1 (c) and (d), with the Mo_{ss} phase as the matrix phase and the intermetallic phase Mo_2Zr as finely distributed second phase particles. The phase boundaries in this two-phase alloy limited the grain growth during casting and thermal treatment resulting in a much smaller grain size (~ 176 µm) as compared to Mo-5Ti and Mo-5V. Hence, the Hall-Petch theory [121,122] and second phase hardening have to be considered when discussing the mechanical properties of Mo-5Zr. EDS measurements show that the remaining Zr concentration in the Mo_{ss} phase is 4.1 at.%, while 8.6 vol.% of Mo_2Zr particles were formed (Table 4.1). With a density of
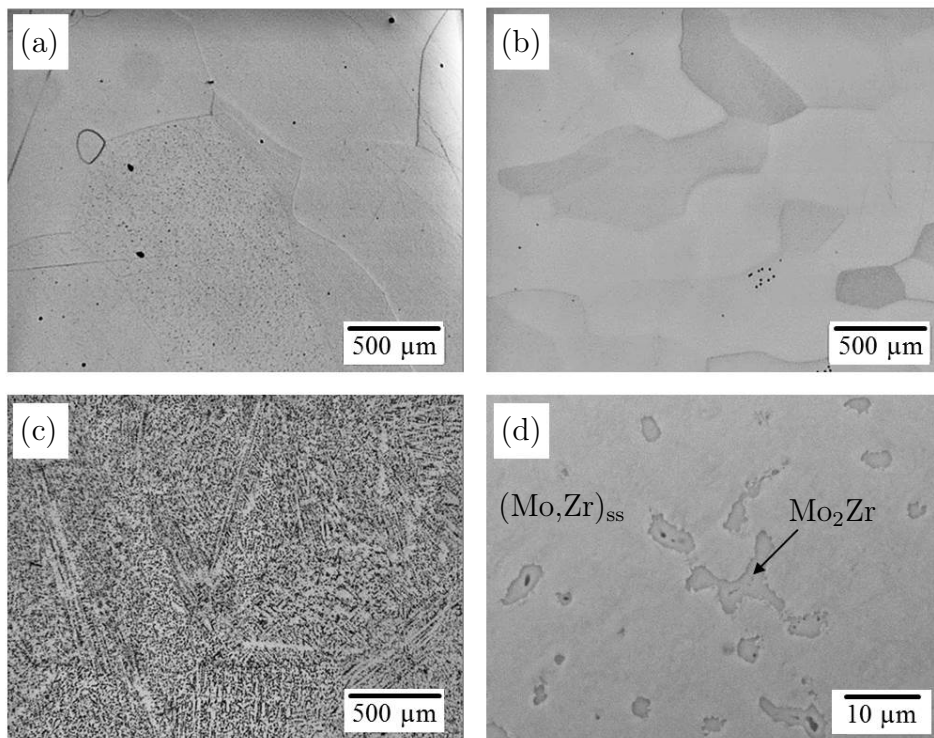

Figure 4.1: OM images of the polished samples of Mo-5X (X = Ti, Zr, V) after casting and annealing (a) Mo-5Ti (b) Mo-5V (c) Mo-5Zr and (d) SEM micrograph of Mo-5Zr [161].

Table 4.1: Microstructural features of Mo-5X (X = Ti, V, Zr) alloys [161].

X	Ti	V	Zr
Calculated density, $\frac{g}{cm^3}$ (pure Mo = $10.21\,\frac{g}{cm^3}$)	9.95	10.01	9.91
Measured density, $\frac{g}{cm^3}$	9.91	10.02	9.95
Average grain size $\pm$ standard deviation, μm	943.4 ± 160	570.7 ± 70	175.8 ± 60
Concentration of alloying element dissolved in Mo$_{ss}$, at.%	5.2	5.7	4.1
Amount of second phases, vol.%	-	-	8.6

$8.63\,\frac{g}{cm^3}$ [161], the phase Mo$_2$Zr contributes to the density reduction of Mo alloys. However, based on the phase diagram presented in the Appendix on page 86, lower concentrations of dissolved Zr in the Mo$_{ss}$ phase would be expected. This might be due to a not completely achieved equilibrium state of the alloys after the annealing process or to ambiguous solubility ranges in the phase diagram at lower temperatures. The XRD pattern in Figure 4.2 (a) illustrates the presence of the Mo$_{ss}$ phase in all alloys. Surprisingly, Mo$_2$Zr was not clearly detected in the two-phase alloy Mo-5Zr. The representation of XRD data in Figure 4.2 (b) shows shifting of the Mo$_{ss}$ diffraction reflexes with respect to the angle position of pure Mo, which indicates changes in the lattice parameters. In order to quantify the lattice parameter, Rietveld analysis and the approach by Vegard's law [162] were used. However, the boundary condition for the application of Vegard's law is an identical lattice structure of the components, so that for Ti and Zr the lattice parameters of the cubic bcc phase were chosen for calculations (polymorphous transformation from hcp to bcc occurs at $\sim 900\,°C$). As visualized in Table 4.2, the smallest deviation between
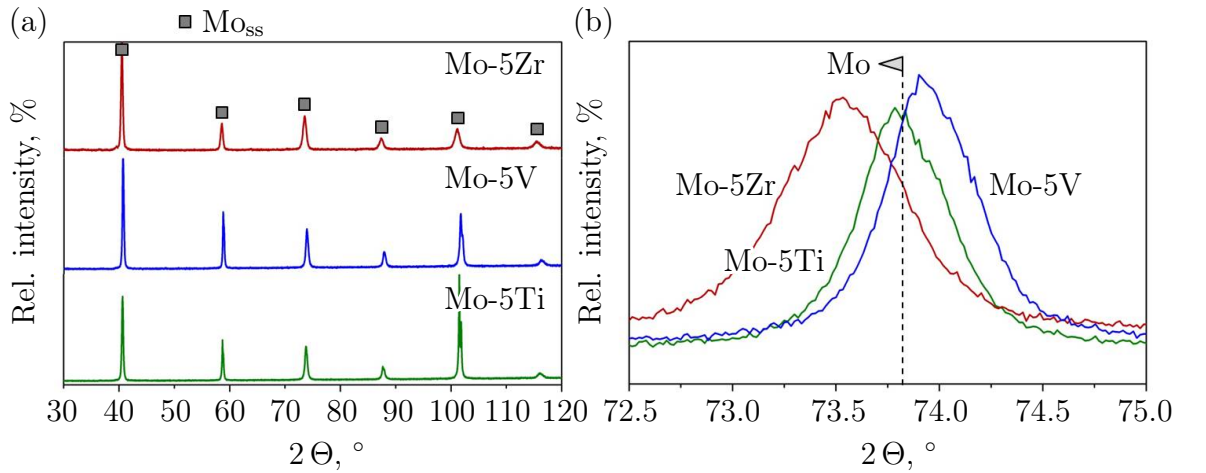

Figure 4.2: XRD data of Mo-5X solid solutions (a) standardized representation and (b) direct comparison visualizing the reflection shifting in comparison to pure Mo.

Table 4.2: Comparison of calculated and measured lattice parameters for Mo-5X alloys.

Alloy composition, at.%	Lattice parameter by Vegard's law, Å	Lattice parameter by Rietveld, Å
Mo	-	3.147
Mo-5Ti	3.155	3.148
Mo-5V	3.141	3.142
Mo-5Zr	3.151	3.158

the different approaches for lattice parameter determination is given by the alloy Mo-5V, which is due to the similar bcc lattice structure [16]. The Rietveld method verifies the bcc structure of all alloys investigated in this study. Only the alloy Mo-5Zr shows minor foreign reflexes which do not fit to the unit cells of the hcp lattice modification of Zr or the Mo_2Zr phase. Most likely a Mo_2Zr phase with bcc structure is formed which has been described by Blažina and co-workers [163, 164] with the space group Im-$3m$ and $a = 3.185$ Å. Furthermore Mo-5Zr shows broadened reflexes which indicate that Zr causes higher stresses within the lattice compared to V and Ti.

Hence, the microstructure of Mo-5Zr was investigated more detailed by SEM and EBSD investigations summarized in Figure 4.3. An impression on the distribution of Mo_2Zr precipitations in the microstructure of Mo-5Zr is given in Figure 4.3 (a). It also illustrates that the Mo_2Zr phases appear both at the grain boundaries and within the grains. An additional phase mapping, visualized in Figure 4.3 (b), clearly identified the corresponding phases as Mo_2Zr (blue) and Mo_{ss} (representing the matrix phase in yellow). Finally, the EDS analysis confirmed the composition of Mo_2Zr by measuring about 66 at.% Mo and 34 at.% Zr in the dark grey particles (Figure 4.3 (a)). The third image (Figure 4.3 (c)) depicts an EBSD orientation map of the Mo_2Zr phases which indicates that the precipitated phases are polycrystalline. A study on phase evolution and the effects of those second phases in Mo-XZr (X = 5, 10, 15, 20 at.%) alloys on the mechanical properties was published elsewhere [165].
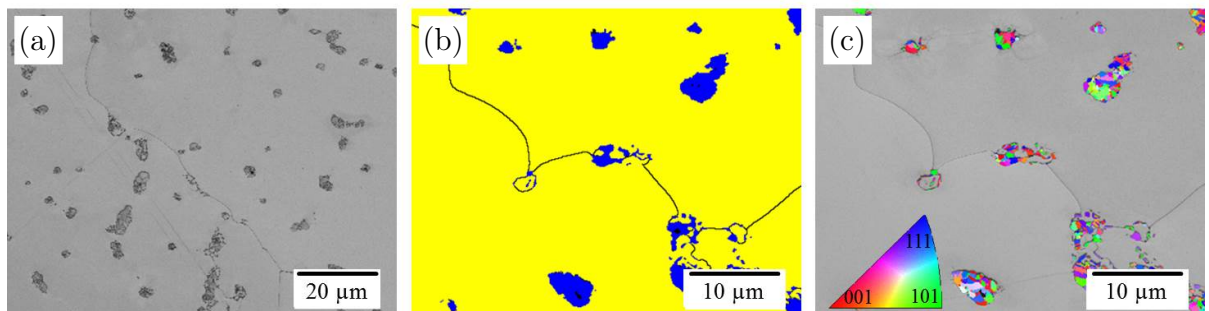

Figure 4.3: SEM and EBSD investigations of Mo-5Zr alloy: (a) EBSD Band Contrast Image (b) phase map (yellow-Mo; blue-Mo_2Zr) (c) orientation mapping of Mo_2Zr phases.

4.1.2 Impact of alloying on solid solution hardening and accompanied microhardness

Determining the microhardness with a pyramidal indenter is a simple method to obtain an initial estimation of the alloying impact of the selected elements $(\mathrm{Ti}, \mathrm{V}, \mathrm{Zr})$ on the mechanical properties of Mo solid solutions. In order to avoid the influence of dislocation pile-up at the grain or phase boundaries, it is necessary to consider a defined distance between the indents and the grain boundaries. According to [156] the minimum interval between the center of neighboring indents as well as the distance between indent and grain boundary should be the threefold of the indent's diagonal length.

For present alloys, the measured maximum diagonal length is $7.4\,\mu\mathrm{m}$ resulting in a minimum interval distance of $22.2\,\mu\mathrm{m}$. This requirement has been fulfilled by only analyzing indents where at least the defined minimum distance between the indents itself as well as between the indents and grain or phase boundaries was maintained. Based on the area ratio of indent (I) to grain (G) size, reaching values between $\mathrm{A_{I/G}} = 0.0001$ for Mo-5Ti up to $\mathrm{A_{I/G}} = 0.0017$ for Mo-5Zr, it was concluded that the effect of grain size on the microhardness values is negligible. Additionally, the effect of second phases, especially for the Mo-5Zr alloy, was neglected by only analyzing indents within the solid solution phase. The results of microhardness measurements evaluated via Vickers indentation technique are shown in Figure 4.4. In general, additions of Ti, V and Zr lead to solid solution hardening improving the microhardness. The hardness value of $3.74 \pm 0.28\,\mathrm{GPa}$ for Mo-5Ti is significantly higher than the reference of pure Mo which is below $3\,\mathrm{GPa}$ and can be understood as an increased level of solid solution strengthening as compared with a
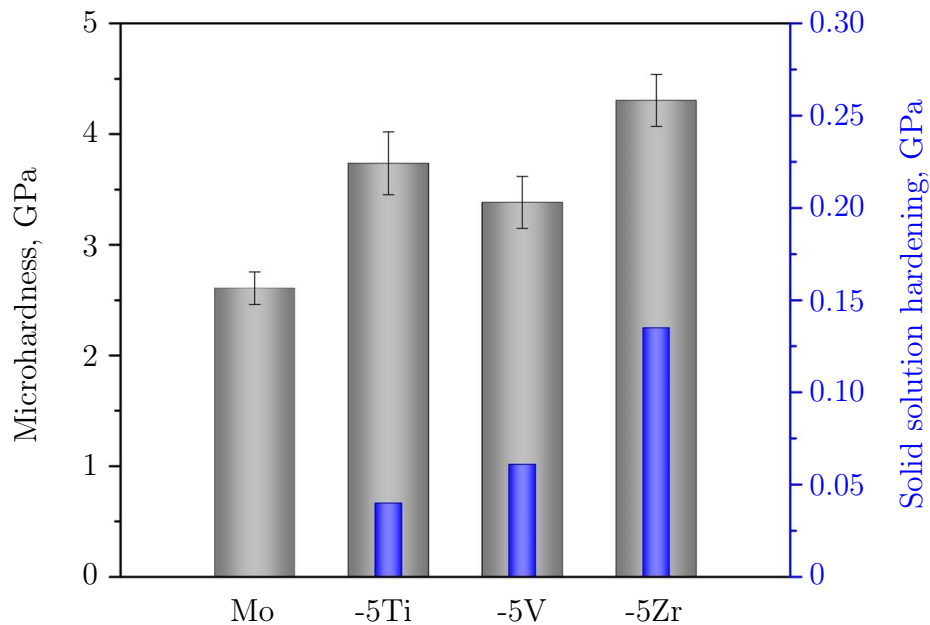

Figure 4.4: Microhardness values for Mo-5X alloys compared to pure Mo and calculated contribution of solid solution hardening.

Mo-0.3Ti alloy with a hardness of $\sim 2.57\,\text{GPa}$ [166] as well as a recrystallized Mo-2.5Ti alloy providing $2.16\,\text{GPa}$ [91]. As already shown in Figure 2.5 in Chapter 2.3 (page 19), even higher hardness values can be achieved as for the present alloys. However, a closer look at Figure 2.5 clarifies that the hardening impacts were assessed on Mo-based alloys in the as-cast state. So, the higher hardness values resulted from additional residual stresses after casting. Comparing the single-phase alloys indicates that Mo-5V shows the lowest improvement of hardness. Notably, the alloy Mo-5Zr represents the highest hardness values in the present comparison and therefore, seems to provide the most significant solid solution hardening effect.

In order to prove this influence, the solid solution hardening was calculated according to Labusch's approach [116] and boundary conditions after Vöhringer [117] as described in detail in Chapter 2.3. The exact parameters used for those calculations can be found in Table A.1 in the Appendix on page 88. In order to determine the pure effect of solid solution hardening on the microhardness, other influential factors according to Equation 2.1 have been considered individually in regard to the present alloys and their influence was weighed up. So, briefly discussed: the work hardening was supposed to be in the same order of magnitude due to an equivalent processing route for the present alloys. The relation of indent to grain size already clarified the negligible influence of grain size. Additionally, due to consequently setting the indents within the solid solution areas (especially in case of the Mo-5Zr alloy), the particle hardening also does not has to be considered.

The impact of Peierls stress is included by only indicating the hardness difference compared to pure Mo, as given in Table 4.3. According to Equation 2.2 the results of calculation are shown in Figure 4.4 and Table 4.3. Finally, the resulting contribution of solid solution hardening on the microhardness value is represented. These data indicate that $\sigma_{\text{SS(Ti)}}<\sigma_{\text{SS(V)}}<\sigma_{\text{SS(Zr)}}$, which is caused by the modulus misfit and different atomic sizes. The impact of solid solution strengthening is in good agreement with the investigations presented by Northcott [74] (on Mo alloys having lower concentrations of solute atoms as present alloys) who ranked the relative ability of alloying elements to harden molybdenum in a decreasing order: Zr, V, Ti.

So, even if Ti was identified as a less effective solid solution strengthener, the microhardness is slightly increased compared to the Mo-5V alloy. Residual stresses might be the reason which lead to significant lattice distortion leading to a high change of lattice parameter (Table 4.2). However, the present observation clearly demonstrates that V is actually a promising element to cause effective solid solution hardening resulting in an increase of

Table 4.3: Calculated impact of solid solution hardening on the microhardness value.

Alloy composition, at.%	Mo-5Ti	Mo-5V	Mo-5Zr
Value of hardness-increase in respect of pure Mo (2.61 GPa), GPa	1.13	0.77	1.70
Solid solution hardening according to Labusch [116], GPa	0.04	0.06	0.14
Contribution of solid solution hardening on the microhardness value, %	4	8	8

microhardness. The particular advantage of V is that, in contrast to Ti and Zr, it exhibits no limited solubility in Mo_{ss}. Therefore it can be dissolved in larger concentrations within the Mo_{ss} which is expected to increase the effect of solid solution hardening even at higher temperatures.

4.1.3 Compressive strength and plastic deformability of Mo solid solutions

The mechanical behavior was determined by constant displacement tests at at a nominal strain rate of $1 \cdot 10^{-4} \frac{1}{s}$ in uniaxial compression at room temperature (RT), 800 °C and 1100 °C. The results are presented in Figure 4.5 in terms of temperature-dependent compressive yield strength and plastic strain (a) and maximum compressive strength compared to tensile strength data (at RT and 871 °C) taken from literature (b). The exactly measured values are given in Table A.3 in the Appendix on page 90.

All alloys show the typical decrease of strength with rising temperatures. The general tendency of the microhardness measurements (Figure 4.4) is validated by the compressive yield strength and maximum compressive strength results at RT (Figure 4.5). Following the approach of Hall and Petch [121, 122] the contribution of the grain size effect must be considered as follows: $\sigma_{GS(Mo-5Ti)} < \sigma_{GS(Mo-5V)} < \sigma_{GS(Mo-5Zr)}$, according to Table 4.1. Therefore, the much smaller grain size of Mo-5Zr contributes significantly to its compressive strength especially at RT.
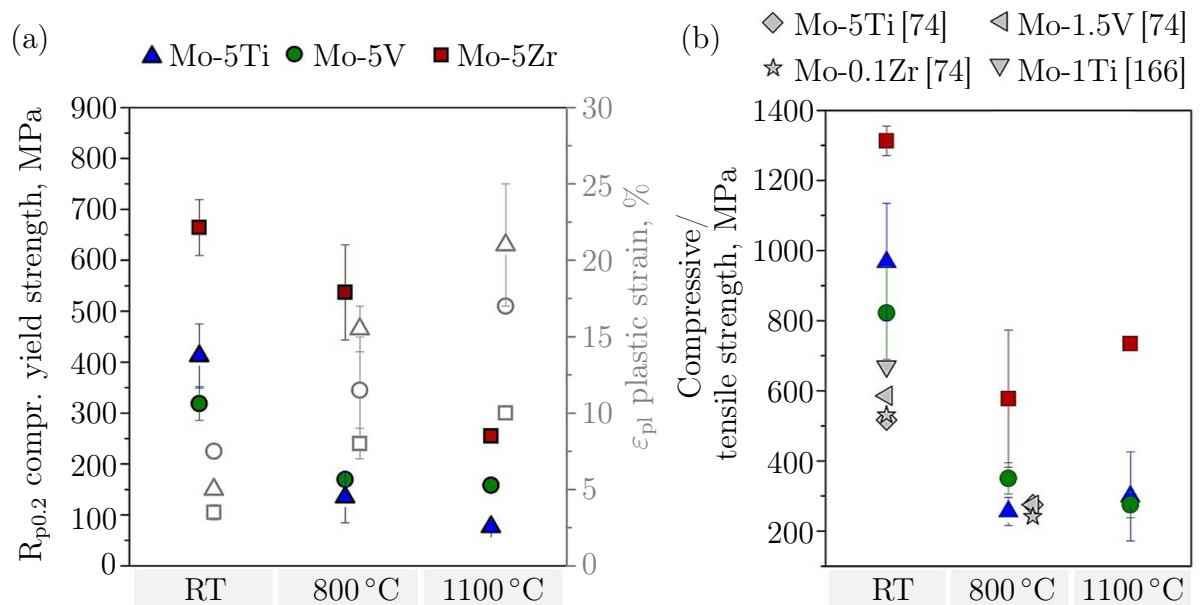

Figure 4.5: Results of compression tests at RT, 800 °C and 1100 °C for the alloys investigated; (a) $R_{p0.2}$ compressive yield strength, plastic strain (open symbols) and (b) maximum compressive strength compared to tensile strength (gray symbols) values taken from literature [74, 166] (at RT and 871 °C).

Even at higher temperatures, this alloy provides the highest values of compressive strength but suffers from low plastic strain with a maximum of 10 % at 1100 °C whereas the deformability of Mo-5Ti is more than twice as high. The outstanding mechanical strength of Mo-5Zr is mainly due to the following reasons: First, the Mo_2Zr precipitations cause the stabilization of the grain size during solidification, which results in the smaller grain size as compared with the other Mo-5X alloys. Second, compared to the investigations of Northcott [74], who evaluated single-phase Mo-Zr alloys up to 0.1 at.% Zr, much higher yield stresses were reached due to a stronger effect of solid solution strengthening at higher Zr concentrations. Third, an additional increase of strength is also given by the homogeneous distribution of the second phase Mo_2Zr particles [161].

The results at elevated temperatures also show that due to different atomic radii of the solute elements Ti and V, i.e. $r_{Mo} = 145$ pm $> r_{Ti} = 140$ pm $> r_V = 135$ pm, the strength and the high temperature deformability of the solid solution phase is dominantly affected. So, Mo-5V has a higher yield strength and lower deformability at 800 °C and 1100 °C compared with Mo-5Ti. The comparison with tensile data from Northcott [74] illustrates that reliable results were obtained for the present alloys. However, the reference data reveal slightly lower strengths than the Mo-5X alloys. It should be noted that the comparative data resulted from tensile tests where material inhomogeneities, like microvoids, and the cross-sectional tapering during testing feature higher impacts on the material's failure than in the compression test. The higher concentration of dissolved elements for the Mo-5X alloys can be considered as a reason for the improved strength level compared with the literature data.

Evaluation of ductility improvement by three-point bending at RT

Beside the density reduction, increasing the plasticity of Mo-based alloys by adding additional alloying elements is a particular objective in the present work. The ductility enhancing effect of the additional elements was already visible in the evaluation of the compression tests. However, it was assumed that the plastic strain was overestimated in those experiments. So, in order to get a more realistic assessment of this material property, three-point flexure was performed on Mo-5X alloy rods in the microtest cell (Figure 3.4 (b), section 3.6.2) at ambient temperatures. After testing a minimum of two samples per alloy, their separate curves lay very close to each other. Therefore, the results are plotted in Figure 4.6 using representative graphs for the respective alloys. The values determined for maximum bending stress and outer fiber tensile strain are given in Table A.4 in the Appendix on page 90.

In general, the measurements confirm the brittle behavior of the Mo-5Zr alloy during the compression test (Figure 4.5) at RT. Whereas for the single-phase Mo-5Ti and Mo-5V alloy a plastic deformability can be recognized. Their strength level is comparable to a PM Mo-1.5Si alloy providing a maximum bending stress of 516 MPa [17]. So, keeping in mind that Si is known as a strong solid solution strengthener, the results of bending tests illustrate, that Ti and V are as well able to improve the materials' strength in the same range, at least due to their higher dissolved fractions within the Mo_{ss}. The higher plastic strain of Mo-5Ti (0.7 %) compared with Mo-5V (0.1 %) seems more realistic as initially
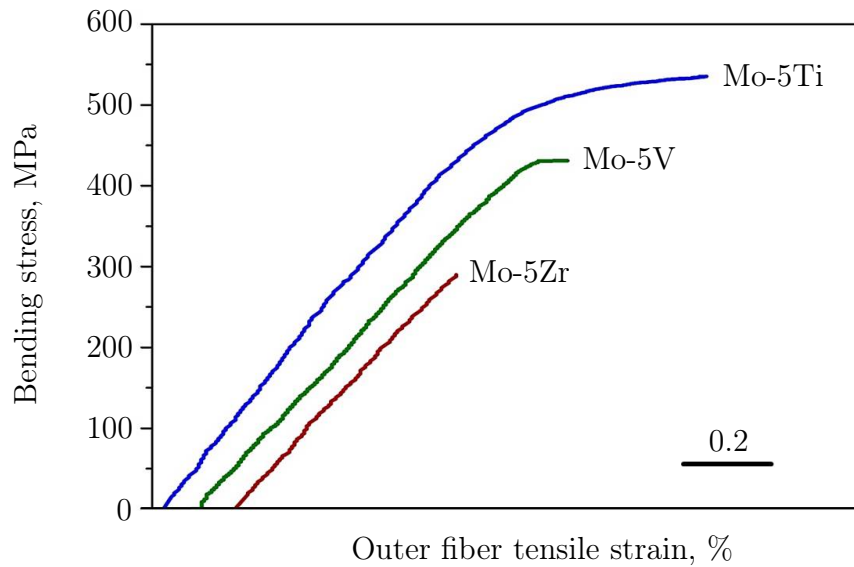
Figure 4.6: Results of three-point bending tests at RT for Mo-5X alloys; Bending stress applied against outer fiber tensile strain.

assumed by the compression tests. So, due to diverse interactions with the relevant foreign atoms, not only the strength and deformability at high temperatures but also the RT properties seemed to be significantly affected. So, the V added Mo_{ss} also exhibits a lower deformability at room temperature compared to Mo-5Ti. The brittleness of Mo-5Zr, is caused by the amount of intermetallic Mo_2Zr phases but also due to the high impact of Zr on the solid solution. The highly differing atomic radii between Mo and Zr (Table 2.2, section 2.2) induce strong lattice distortions as well as effective solid solution hardening (Table 4.3).

The investigation of the fracture surfaces, in Figure 4.7, revealed that in all cases the fracture at room temperature is brittle. Similar to pure Mo [17] the alloy Mo-5Ti ruptured transcrystalline (Figure 4.7 (a)). In contrast, the addition of V to Mo changed the fracture mode into intergranular fracture (Figure 4.7 (b)). As visualized in Figure 4.7 (c), in case of alloy Mo-5Zr, the fracture surface shows predominantly intergranular but also large areas of transcrystalline rupture. In conclusion, the compression as well as the three-point
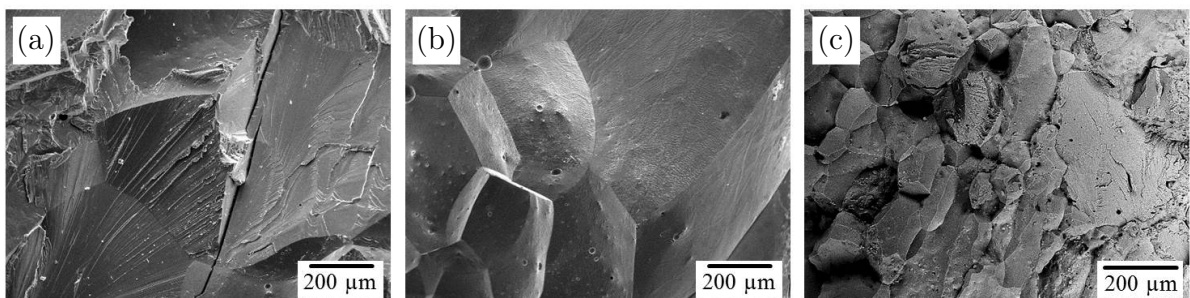

Figure 4.7: SEM images of the fracture surfaces of the binary alloys (a) Mo-5Ti, (b) Mo-5V and (c) Mo-5Zr, all presenting a brittle fracture behavior.

bending tests confirmed vanadium to be a competitive alloying element compared with Ti and Zr, due to its positive effect on the strength and ductility of Mo-based alloys in the entire range of potential application temperatures. In this context, contrasting to Ti and Zr, V exhibits an essential advantage: it is highly soluble in Mo, which might affect the mechanical properties and the density on a wider range than Ti and Zr would do.

4.2 Density reduction of multiphase Mo-Si-B alloys by vanadium substitution

The promising observations regarding the binary alloying systems represent an excellent starting point for further investigations concerning the effects of V in the favored ternary composition Mo-9Si-8B. In order to get a first impression on the microstructural properties, Mo-9Si-8B powders alloyed with increased V-concentrations (10, 20, 30, 40 at.%) have been investigated. Detailed SEM, EDS as well as X-ray analysis coupled with Rietveld refinement and DFT calculations provided information on special microstructure and crystallographic features.

Afterwards, the Mo-40V-9Si-8B alloy was chosen for further studies on the mechanical properties. The tests required for thermomechanical characterization were carried out on compact specimen produced via field assisted sintering technology (FAST) as well as arc-melting (Arc). The application-specific properties were analyzed using three-point bending of notched samples at RT (evaluating the fracture toughness) and three-point flexure (determination of BDTT) as well as creep tests at elevated temperatures up to 1100 °C.

Finally, the oxidation resistance was tested performing cyclic oxidation tests between 800 °C and 1100 °C. Additionally, the effect of minor Fe-additions (3 at.%) on the oxidation performance of the Mo-40V-9Si-8B alloy has been verified.

4.2.1 Characterization of Mo-XV-9Si-8B powders

First investigations of the microstructural evolution were performed on mechanically alloyed (200 rpm for 30 h) and thermally treated (1300 °C for 5 h under argon) Mo-XV-9Si-8B powders, which represents a useful approach to predict the microstructure of compact powder metallurgy (PM) samples. Due to the high solubility of V in Mo and in order to achieve a significant density reduction of Mo-9Si-8B, the V substitutions to Mo are supposed to be higher as for the binary alloy (Mo-5V), so 10, 20, 30 and 40 at.% V were chosen.

BSE images of the resulting powders are illustrated in Figure 4.8 and represent the characteristic multiphase microstructure already known for similarly treated Mo-9Si-8B powders from previous work [57]. All powders revealed a balanced fraction of Mo_{ss} phase (light-gray phase) and finely distributed intermetallic phases (IP, dark-gray phases), as proven by the values listed in Table 4.5. Their morphology and distribution seemed to be
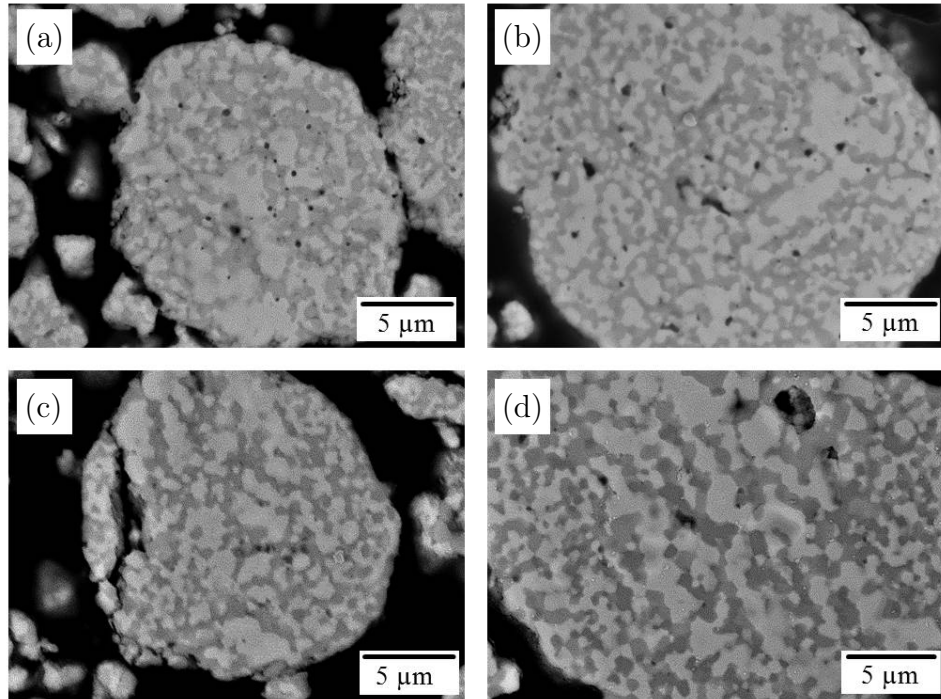
Figure 4.8: SEM images of mechanically alloyed Mo-XV-9Si-8B powders after thermal treatment at 1300 °C for 5 h with V concentration of (a) 10 at.%, (b) 20 at.%, (c) 30 at.%, and (d) 40 at.%; Mo_{ss} phase is light-gray; IP's are the dark-gray phases [99].

independent of the V concentration in the alloy. The average particle sizes are listed in Table 4.4. After processing, the powder exhibited particle sizes of ~ 4–5 μm, showing a slight trend for size reduction with increasing V concentration. A significant effect was observed regarding the oxygen concentration of the powders (Table 4.4). Vanadium exhibits a high affinity for oxygen [129], so even the as-received V powder contained 5100 wppm O_2, compared with 1500 wppm O_2 for Mo powder. Consequently, higher V additions led to an increase of the oxygen concentration in the Mo-Si-B powders.

Figure 4.9 shows representative powder X-ray diffractograms for the Mo-40V-9Si-8B sample in the as-milled state (MA) and after thermal treatment (TT) at 1300 °C for 5 h, in comparison with similarly processed Mo-9Si-8B powder. As expected from previous work

Table 4.4: Decisive features of the Mo-XV-9Si-8B powders investigated.

| Nominal alloy composition, at.%	Average particle size, μm	Oxygen concentration, wppm
Mo-10V-9Si-8B	4.78 ± 0.52	4135 ± 475
Mo-20V-9Si-8B	4.28 ± 0.73	4957 ± 193
Mo-30V-9Si-8B	4.18 ± 0.51	4984 ± 66
Mo-40V-9Si-8B	3.96 ± 0.75	5787 ± 188
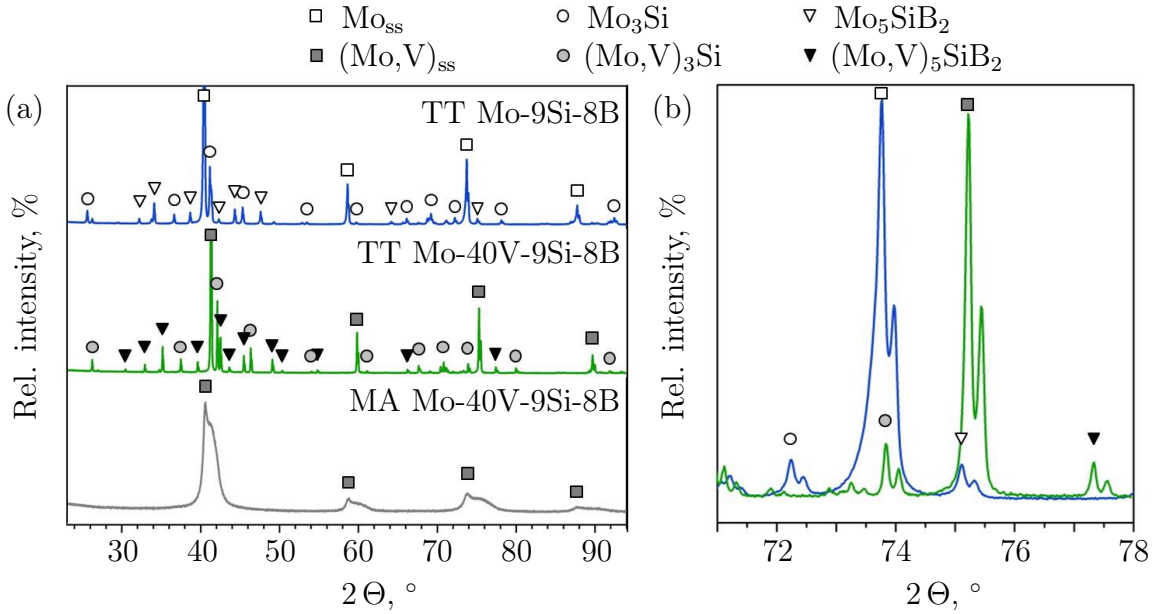
Figure 4.9: X-ray diffraction data: (a) for the mechanically alloyed (MA) and the thermally treated (TT) powders of the Mo-40V-9Si-8B sample in comparison with a mechanically alloyed and thermally treated Mo-9Si-8B powder and (b) visualization of peak shifting shown on an enlarged region between 71° and 78° [99].

on mechanically alloyed Mo-Si-B and V-Si-B powders [13, 57], a supersaturated $Mo(V, Si, B)$ solid solution phase formed after 30 h of milling, causing explicit reflection broadening due to the high concentrations of V, Si, and B dissolved in the Mo lattice. After thermal treatment the reference alloy Mo-9Si-8B shows the typical intermetallic phases Mo_3Si and Mo_5SiB_2 beside the Mo_{ss} phase, as visualized in Figure 4.9. In general, the alloy Mo-40V-9Si-8B depicted a similar diffraction pattern after thermal treatment as compared with reference alloy Mo-9Si-8B, but includes a shift of reflexes towards higher 2Θ angles (Figure 4.9 (b)). According to Braggs' Equation 3.3, this effect occurs due to the smaller atomic size of V, which is dissolved within the corresponding phases. So, this slight shift of reflexes confirms the assumption of vanadium dissolved in the respective phases. This is also visible for the materials alloyed with 10, 20 and 30 at.% V where the shifting effect increases with higher V concentrations, as illustrated in Figure 4.10.

Further analysis by Rietveld refinement finally confirmed the presence of intermetallic $(Mo,V)_3Si$ and $(Mo,V)_5SiB_2$ phases in addition to the $(Mo,V)_{ss}$ phase (light-gray phase; Figure 4.8) after thermal treatment. As a result, the exact alloy composition (phase fractions in wt.%) as well as the densities of the individual phases were given in order to determine the phase fractions in vol.%. As presented in Table 4.5, the amount of Mo_{ss} phase ranged between 54.0 vol.% (for Mo-10V-9Si-8B) and 47.4 vol.% (for Mo-40V-9Si-8B), the balance being the sum of the intermetallic phases.

Hence, it can be assumed that V alloying will not lead to a significant change in the general phase formation in Mo-Si-B alloys within the Mo_{ss}-Mo_3Si-Mo_5SiB_2 triangle. This aspect is very important in order to keep the balance between Mo_{ss} and intermetallic phases
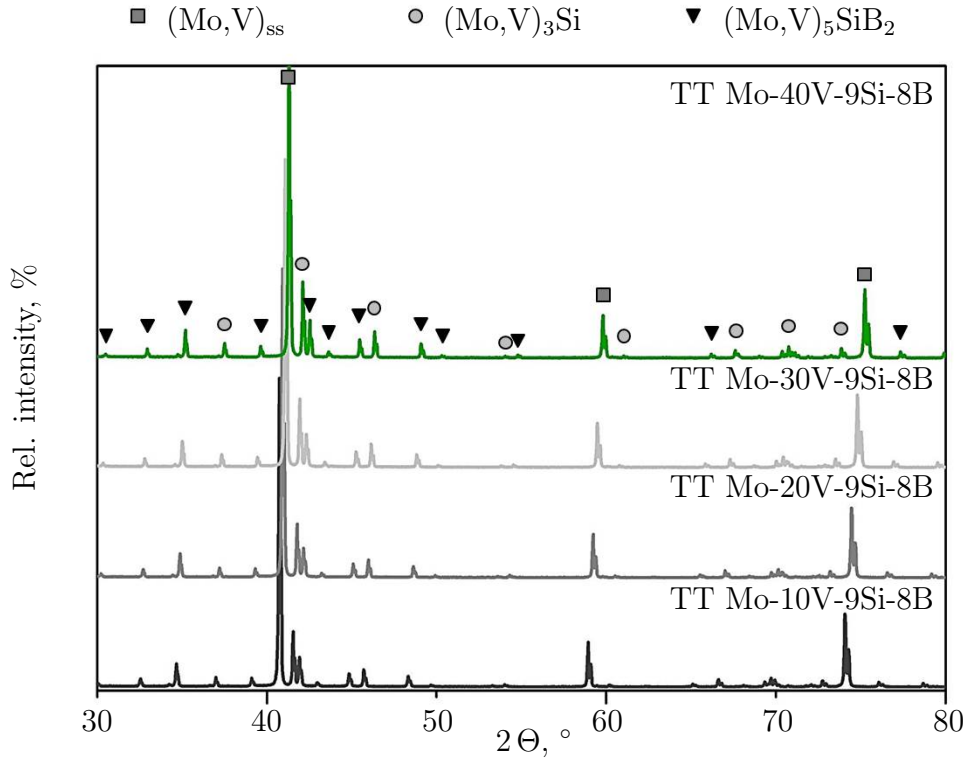
Figure 4.10: Comparison of XRD Pattern for MA and TT Mo-XV-9Si-8B alloys.

providing the desired microstructure according to Berczik [19, 20].

Following the aim of a highly reduced density, the powder alloyed with $40 \, \text{at.\%}$ V provides a (calculated) density of $8.48 \, \frac{\text{g}}{\text{cm}^3}$ (Table 4.5) which is not only smaller compared to PM Mo-9Si-8B ($\rho = 9.47 \pm 0.05 \, \frac{\text{g}}{\text{cm}^3}$ [99, 100]) but even undercuts the density of CMSX-4 ($\rho = 8.7 \, \frac{\text{g}}{\text{cm}^3}$ [5]). Thus, more detailed Rietveld refinement concentrated on this promising alloy composition.

The volume fraction of the respective phases as well as the concentration of V dissolved in each phase are presented in Table 4.5, verifying the high solubility of V in the three-phase Mo-Si-B system. Generally, it can be observed that there is a strong affinity of V to occupy the transition metal positions of $(Mo,V)_5SiB_2$. In this regard, Rietveld refinement was applied to analyze the characteristics of the occupation of atomic positions in the Mo-40V-8B-9Si powder, especially for $(Mo,V)_5SiB_2$.

For $(Mo,V)_{ss}$ and $(Mo,V)_3Si$, vanadium randomly occupies the Mo sites, thus the resulting crystal structures are isotypic to Mo_{ss} and Mo_3Si phases known from the ternary Mo-Si-B system (Table 2.1; section 2.1). Interestingly, the amount of V dissolved in the intermetallic phases deviated significantly from the overall vanadium content of $40 \, \text{at.\%}$ as adjusted during the alloy preparation. The V concentration was $60 \, \text{at.\%}$ for $(Mo,V)_3Si$ but $54 \, \text{at.\%}$ for $(Mo,V)_5SiB_2$, indicating preferred solubility of vanadium in the intermetallic phases. Consequently, the $(Mo,V)_{ss}$ is depleted in V ($24 \, \text{at.\%}$) with respect to the initial V concentration. Taking those doping levels into account, in combination with the volume fractions of the individual phases, the correct overall composition of Mo-40V(-9Si-8B) is obtained, indicating that the V contents within the phases are reliable values.

In contrast to the Mo_{ss} and Mo_3Si phases, the Mo_5SiB_2 ($D8_I$) structure contains two

Table 4.5: Individual phase fractions (including their respective V-concentrations) and densities used for density calculation of Mo-XV-9Si-8B alloys.

	Phase fractions, vol.%	Concentration of V dissolved in the phases, at.%	Density of individual phases, $\frac{g}{cm^3}$	Theoretical composite density, $\frac{g}{cm^3}$
Mo-10V-9Si-8B				9.35
$(Mo,V)_{ss}$	54.0	10	10.15	
$(Mo,V)_3Si$	20.1	17	8.51	
$(Mo,V)_5SiB_2$	25.9	73	8.32	
Mo-20V-9Si-8B				9.09
$(Mo,V)_{ss}$	52.2	8	10.11	
$(Mo,V)_3Si$	23.7	32	8.05	
$(Mo,V)_5SiB_2$	24.1	76	7.90	
Mo-30V-9Si-8B				8.77
$(Mo,V)_{ss}$	48.9	14	10.08	
$(Mo,V)_3Si$	28.8	45	7.58	
$(Mo,V)_5SiB_2$	22.3	65	7.47	
Mo-40V-9Si-8B				8.48
$(Mo,V)_{ss}$	47.4	24	10.04	
$(Mo,V)_3Si$	29.7	60	7.11	
$(Mo,V)_5SiB_2$	22.9	54	7.05	

crystallographic distinguishable metal sites (Wyckoff positions 4c and 16l in space group $I\frac{4}{m}cm$) which differ in their site symmetry [47, 167]. From the Rietveld refinement results, a preference of V for the more highly symmetric 4c site, which is occupied to 94 at.% by V, compared with the 16l position (50 at.% V) could be derived. This special metal site occupation has been visualized in Figure 4.11 using the software Diamond [168]. First, it was assumed, that this might be a consequence of the different coordination environment (Figure 4.11 (b) and (c)), especially with Si and B, for both positions: At the 4c site, the metal is surrounded by four B atoms and two Si atoms forming a distorted octahedron, each face of which is capped by another metal atom (total coordination number, CoN: 14). In contrast, the metal on site 16l is irregularly surrounded by only three B and two Si atoms plus 11 other metal atoms (total CoN: 16). In order to understand the results of Rietveld refinement and to find out the driving force for the site preference of V, DFT calculations were carried out and evaluated in the following section.
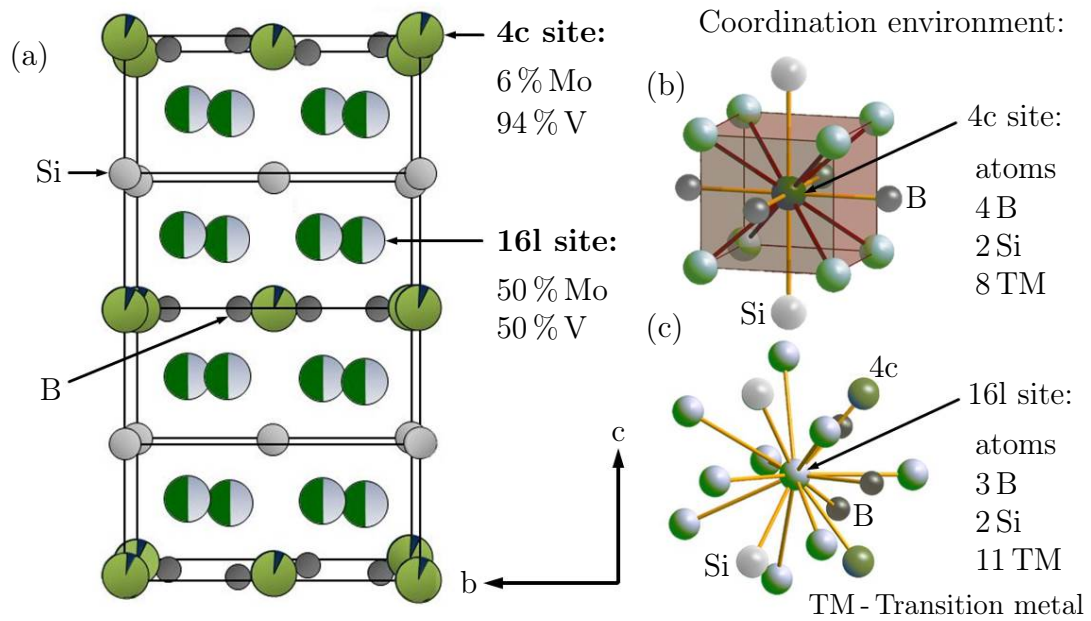
Figure 4.11: (a) Projection of the D8$_I$ structure of (Mo,V)$_5$SiB$_2$ on the (100) plane using the data from mechanically alloyed and thermally treated Mo-40V-9Si-8B powder, (b) coordination environment of metal site 4c in (Mo,V)$_5$SiB$_2$ and (c) coordination environment of metal site 16l in (Mo,V)$_5$SiB$_2$ [99].

4.2.2 DFT simulation for site preference of V in (Mo,V)$_5$SiB$_2$

The DFT calculations by Dr. rer. nat. Rachid St. Touzani were based on the experimental findings from the Mo-XV-9Si-8B powder analyses [169]. The Rietveld refinement after X-ray diffraction measurements confirmed the existence of V within the corresponding phases (Mo,V)$_{ss}$, (Mo,V)$_3$Si and (Mo,V)$_5$SiB$_2$. Additionally, it was pointed out, that in the (Mo,V)$_5$SiB$_2$ compound, V showed a site preference for the 4c Wyckoff position whereas the 16l Wyckoff position was randomly occupied by V and Mo (Figure 4.11). A similar observation was made for rhenium additions to a Mo-Si-B alloy, where Re occupied the 4c position in Mo$_5$SiB$_2$ [170].

In general, TM$_5$SiB$_2$ (TM: Transition metals) is also known as T2 phase in the scientific community. For instance, Mo$_5$SiB$_2$ was described in the late fifties by Nowotny and co-workers [30] while its experimental elastic properties have been reported by Ihara et al. in 2002 [50]. Some elastic properties, calculated by first principles density functional theory (DFT) have been reported by Aryal et al. [171], Zhang et al. [172] and Hütter et al. [173].

V$_5$SiB$_2$ has been focused by different research groups starting with investigations by Kudielka et al. [174] in 1957. Its experimentally measured microhardness was reported by Krüger [13], while DFT studies for the elastic properties of V$_5$SiB$_2$ are still missing. Both Mo$_5$SiB$_2$ and V$_5$SiB$_2$ crystallize as a ternary variant of the Cr$_5$B$_3$ type structure [175] (Space group: $I\frac{4}{m}cm$) with Wyckoff positions 4c and 16l for Mo/V, 4a for Si and 8h for B. Since the T2 phases are enormously important for the creep performance of TM-Si-B alloys, the phenomenon of site preference as well as the influence of V on the chemical

Table 4.6: Exact composition of T2 - $V_y Mo_{5-y} SiB_2$ phase according to the results of Rietveld refinement.

Nominal alloy composition, at.%	$V_y Mo_{5-y} SiB_2$	
	y	5-y
Mo-10V-9Si-8B	3.65	1.35
Mo-20V-9Si-8B	3.80	1.20
Mo-30V-9Si-8B	3.25	1.75
Mo-40V-9Si-8B	2.94*	2.06*

*According to the crystallographic model shown in Figure 4.11.

bonding has to be clarified. In this work, the approach of first principles DFT calculations was used to answer those questions.

Speaking about $(Mo,V)_5 SiB_2$ phases generally means apart from one Si and two B atoms, there are five atoms per formula unit, which can either be Mo or V. Hence, in the present thesis, a more precise notation will be introduced: $V_y Mo_{5-y} SiB_2$, where V is mentioned first since it is listed before Mo in the periodic table. The subscripts y for V and 5-y for Mo had been assigned since there are only a few DFT studies for $V_5 SiB_2$ yet, whereas the crystallography of $Mo_5 SiB_2$ has already been extensively investigated.

Starting with the assumption, according to the crystallographic model shown in Figure 4.11, that T2 generally exhibits in total 20 transition metal atoms/positions (16l+4c), the number of V and Mo atoms, visualized in Table 4.5, were divided by this total value in order to obtain the empirical formula. A more precise determination was possible for the T2 crystal structure of Mo-40V-9Si-8B, visualized in Figure 4.11, due to the exact percentages given for V and Mo on 16l as well as on 4c site. The results are shown in Table 4.6 which indicates that two main phase compositions were obtained for the present alloys with the following idealized composition: $V_3 Mo_2 SiB_2$ and $V_4 MoSiB_2$.

Beside these two compositions, the further members of the boride series $V_y Mo_{5-y} SiB_2$ ($V_5 SiB_2$, $V_2 Mo_3 SiB_2$, $VMo_4 SiB_2$, $Mo_5 SiB_2$) had also been considered in the DFT calculations. As shown in Table 4.7, different occupations of 4c and 16l position had been assumed for modeling the respective phases.

In a first step, the lattice parameters as well as the density after structural relaxation were calculated for the $V_y Mo_{5-y} SiB_2$ phases. Using the lattice parameters (listed in Table A.2 in the Appendix, page 89) the volume of unit cell was determined in order to illustrate the effect of alloying with vanadium. In Figure 4.12 the influence of increasing V concentrations (y = 0, 1, 2, 3, 4, 5) on the volume of unit cell and on the density of the boride series $V_y Mo_{5-y} SiB_2$ is shown. Figure 4.12 (a) clearly illustrates the decrease of the volume of unit cell with increasing V and decreasing Mo concentrations. Thus, this volume effect resulted from the decrease of lattice parameters a and c as expected from the smaller atomic size of V compared with the atomic size of Mo.

The comparison to experimental data (from Rietveld refinement) shows that, except for $V_4 MoSiB_2$, the calculations are in good agreement with the present GGA-PBE-DFT calcu-

Table 4.7: Occupation of 4c and 16l sites in the T2 models for DFT calculation.

y	$V_yMo_{5-y}SiB_2$	4c	16l
0	Mo_5SiB_2	100 % Mo	100 % Mo
1	VMo_4SiB_2	100 % V	100 % Mo
2	$V_2Mo_3SiB_2$	100 % Mo	50% Mo/V
3	$V_3Mo_2SiB_2$	100 % V	50% Mo/V
4	V_4MoSiB_2	100 % Mo	100 % V
5	V_5SiB_2	100 % V	100 % V

lated data. In general, both calculated lattice parameters a and c (Table A.2, Appendix page 89) as well as the volume of unit cell provided a maximum of 1 % deviation from the experimental parameters. However, for V_4MoSiB_2 the deviation between experimental and DFT data was less than 4 %, which can be explained by the differences in site occupation. So, as shown in Table 4.7 the model for V_4MoSiB_2 assumed 100 % Mo on 4c and 100 % V on 16l site whereas under real conditions V was expected to occupy the 4c site due to its site preference. Based on this assumption, a deviation of less than 4 % is still acceptable. An additional comparison with lattice parameters of Mo_5SiB_2 and V_5SiB_2 resulting from other DFT studies by several authors [167, 171–173] showed a high agreement to the parameters of the present DFT calculations and therefore confirmed its reliability. Another important issue of alloying with vanadium is the density reduction
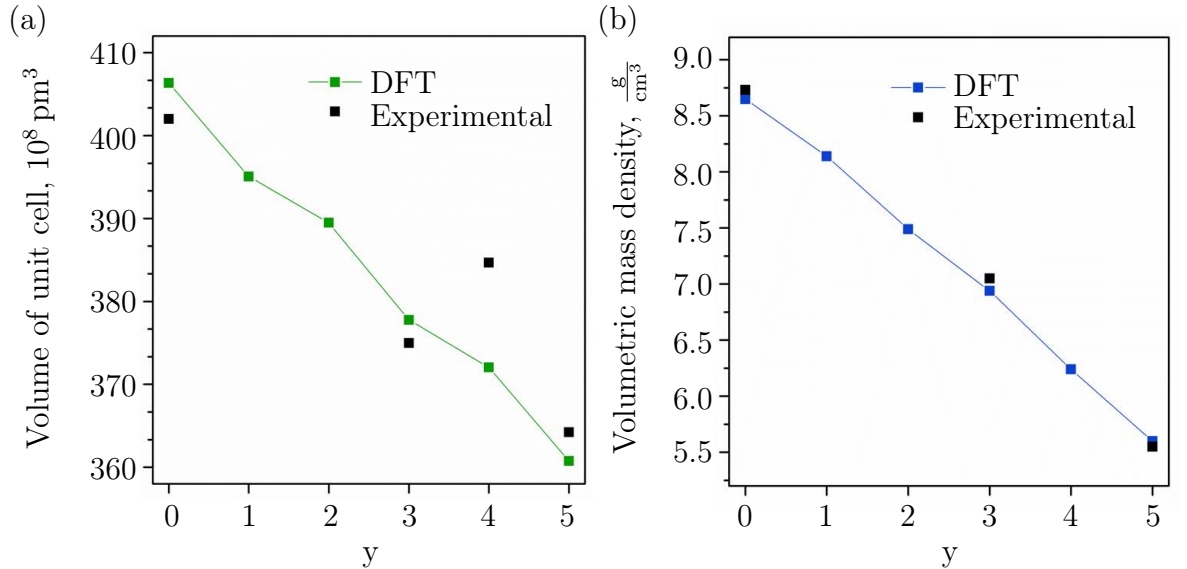

Figure 4.12: Comparison of experimental and DFT calculated parameters of $V_yMo_{5-y}SiB_2$ phases for $y = 0, 1, 2, 3, 4, 5$ (a) lattice volume of unit cell (experimental data for Mo_5SiB_2 and V_5SiB_2 determined after [174, 176]) and (b) density according to Rietveld refinement, also for V_5SiB_2 [169].

which is visualized in Figure 4.12 (b). The volumetric mass density of the boride series declines from $8.65 \frac{g}{cm^3}$ for Mo_5SiB_2 to $5.60 \frac{g}{cm^3}$ for V_5SiB_2 with increasing amount of V. The experimental volumetric mass densities deviate by less than 2% from the DFT calculated volumetric mass densities. They also represent the trend of decreasing volumetric mass densities with increasing amount of V and therefore the DFT calculations are in very good agreement with the experiment. The effect on the density represents a huge advantage in regard to the focused application of the present Mo-XV-9Si-8B alloys. Especially in the case of Mo-40V-9Si-8B, where the T2 phase corresponds to the empirical formula $V_{2.94}Mo_{2.06}SiB_2$ (Table 4.6, Figure 4.11) a density reduction of 19% was reached compared to Mo_5SiB_2 in Mo-9Si-8B.

Enthalpy of formation of the boride series $V_yMo_{5-y}SiB_2$

In order to gain a further insight of the boride series $V_yMo_{5-y}SiB_2$ ($y = 0, 1, 2, 3, 4, 5$) the enthalpy of its formation was calculated, presented in Figure 4.13. The enthalpy of formation ranges between $-370 \frac{kJ}{mol}$ for Mo_5SiB_2 and $-591 \frac{kJ}{mol}$ for V_5SiB_2, respectively. Hence, the formation of these phases is energetically in favor versus the pure elements. As shown in Figure 4.13, an increasing amount of V generally features a lower energy for the enthalpy of formation, which obviously favors the vanadium rich $V_yMo_{5-y}SiB_2$ borides. This aspect might explain, why there were no vanadium poor borides found in the Mo-XV-9Si-8B alloys.

However, there are two exceptions to this general trend concerning $V_2Mo_3SiB_2$ and V_4MoSiB_2 as their enthalpy of formation slightly increases. For both phases the Wyckoff 4c position is occupied by 100% molybdenum (Table 4.7). So in general this means that in terms of energy the Wyckoff position 4c favors vanadium, which is in agreement with
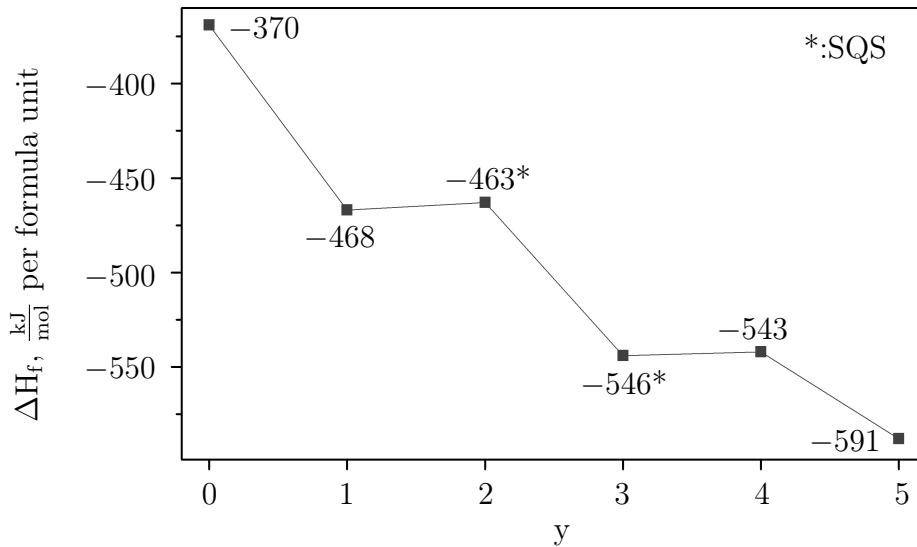

Figure 4.13: Plot of the enthalpy of formation for the borides $V_yMo_{5-y}SiB_2$ ($y = 0, 1, 2, 3, 4, 5$), SQS: Special Quasirandom Structure.

the experimental observations as the 4c position shows a 94 % occupation of V and only 6 % Mo (Figure 4.11). As explained earlier, the coordination environment might be an influential aspect in order to find a reason for this site preference behavior. So in a next step it was decided to analyze the chemical bonding for the transition metals V and Mo on Wyckoff position 4c and search for unstable bonding situations for this atomic site.

Chemical bonding situation in the borides $V_yMo_{5-y}SiB_2$

The following figures, kindly permitted by Dr. rer. nat. Rachid St. Touzani, illustrate the Crystal Orbital Hamilton Population ($-$COHP) plots to reveal the influence of the occupation by either Mo or V on the Wyckoff position 4c to the TM-Si (TM $=$ Mo or V) bonding interaction. A similar procedure was reported by Deringer et al. [177] in order to explain the mixed occupation of Ti and Os in the intermetallic boride $Ti_{1+x}Os_{2-x}RuB_2$ and is therefore an useful approach to explain the present phenomenon.

First, the bonding situation for Mo_5SiB_2 was considered with Mo on both Wyckoff sites 4c and 16l. The $-$COHP plot, given in Figure 4.14 (a), demonstrates a large number of occupied antibonding states (red) in the area of -1.4 eV to 0 eV for the Mo-Si bonds with

(a) 2x Mo(4c)-Si in Mo_5SiB_2 (b) 2x V(4c)-Si in V_5SiB_2
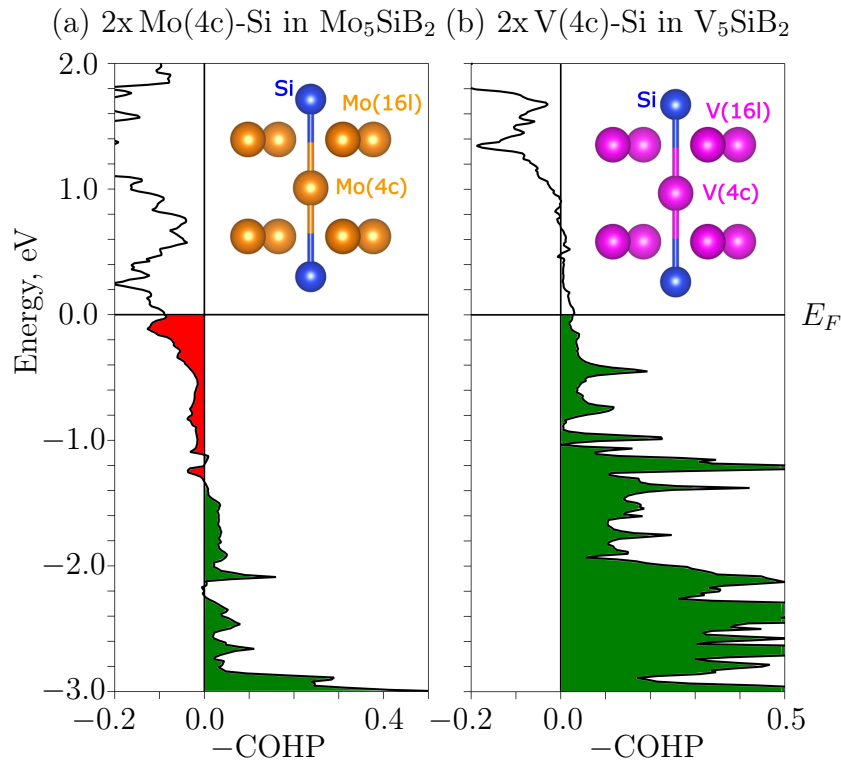
Figure 4.14: $-$COHP plots of (a) the Mo-Si bonds in Mo_5SiB_2 and (b) the V-Si bonds in V_5SiB_2, each Mo/V atom of the Mo/V-Si bond is on the Wyckoff 4c site. Occupied antibonding states are shown in red, while the bonding states are shown in green [169].

Mo on the 4c site. However, in the case of V_5SiB_2, where V is on 4c and 16l, the $-$COHP plot depicted in Figure 4.14 (b) only shows occupied bonding states (green) near the Fermi level (E_F).

If Mo substitutes V on the 4c Wyckoff site in V_5SiB_2, the composition turns to V_4MoSiB_2, where the Mo occupies now exclusively the 4c site. As represented by the $-$COHP plot in Figure 4.15 (a), the Mo-Si bonds still show a significant amount of occupied antibonding states near the Fermi level in the area of $-1.6\,\mathrm{eV}$ to $0\,\mathrm{eV}$. Figure 4.15 (b) depicts the situation of the V-Si bond where V substitutes Mo on the 4c site and Mo is on 16l position in order to model VMo_4SiB_2. In this case only very small amounts of occupied antibonding states are present for the V-Si bonds near the Fermi level.

The two remaining models shall imitate the experimentally observed $50\,\%$ V and $50\,\%$ Mo occupation on Wyckoff position 16l. The corresponding $-$COHP plots of the TM-Si (TM $=$ Mo or V) bonds are illustrated in Figure 4.16. In $V_2Mo_3SiB_2$, Mo is on Wyckoff site 4c, while the Wyckoff position 16l is occupied by $50\,\%$ V and $50\,\%$ Mo. The $-$COHP plot of two independent Mo(4c)-Si bonds (which means the two Mo-Si bonds do not originate from the same Mo atom), shown in Figure 4.16 (a), represent a significant amount of occupied antibonding states near the Fermi level. In total 30 of 32 ($94\,\%$) Mo(4c)-Si bonds show antibonding interactions near the Fermi level.

A totally different situation was found for the boride $V_3Mo_2SiB_2$ which is a model very close

(a) 2x Mo(4c)-Si in V_4MoSiB_2 (b) 2x V(4c)-Si in VMo_4SiB_2
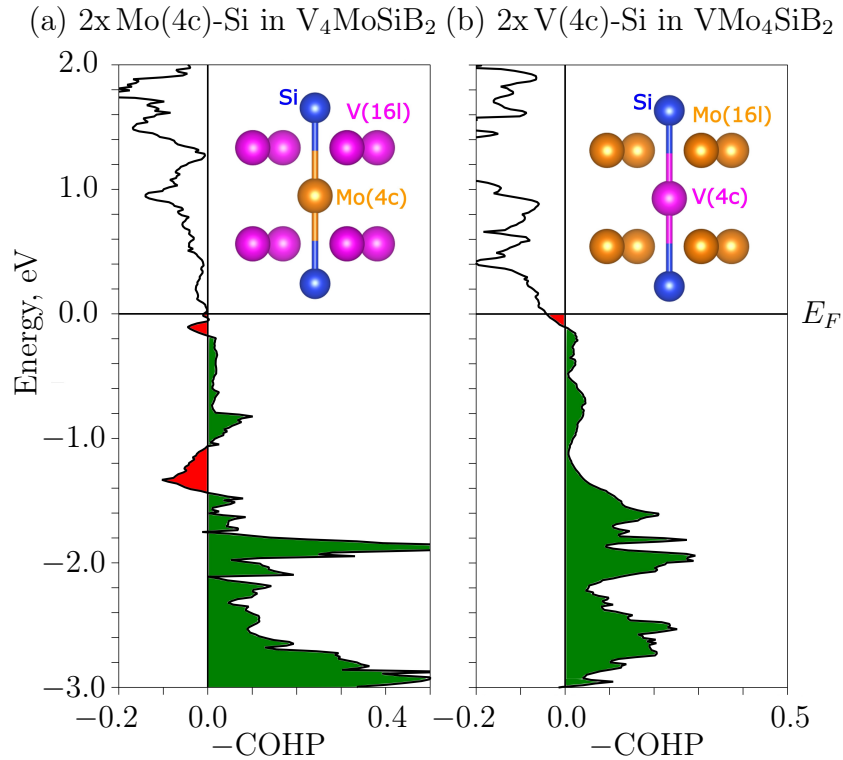
Figure 4.15: $-$COHP plots of (a) the Mo-Si bonds in V_4MoSiB_2 and (b) the V-Si bonds in VMo_4SiB_2, each Mo/V atom of the Mo/V-Si bond is on the Wyckoff 4c site. Occupied antibonding states are shown in red, while the bonding states are shown in green [169].

(a) 1x Mo(4c)-Si in $V_2Mo_3SiB_2$ (b) 1x V(4c)-Si in $V_3Mo_2SiB_2$
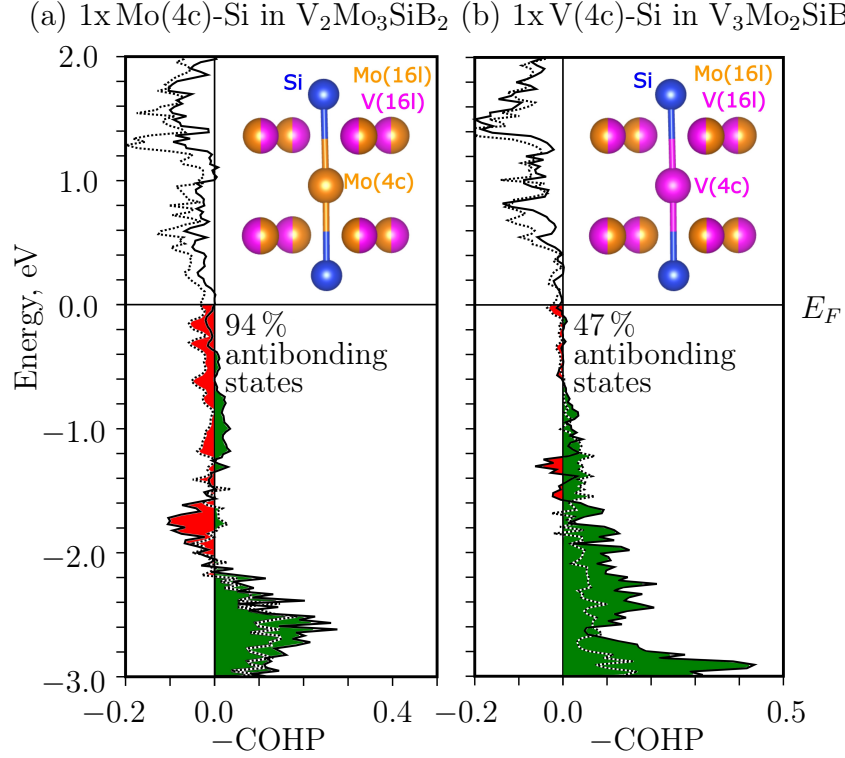
Figure 4.16: −COHP plots of (a) the Mo-Si bonds in $V_2Mo_3SiB_2$ and (b) the V-Si bonds in $V_3Mo_2SiB_2$, each Mo/V atom of the Mo/V-Si bond is on the Wyckoff 4c site. Occupied antibonding states are shown in red, while the bonding states are shown in green [169].

to the experimentally determined chemical composition $V_{2.94}Mo_{2.06}SiB_2$ in Mo-40V-9Si-8B. Similar to the model explained before, the Wyckoff position 16l is occupied with 50 % V and 50 % Mo. However, the Wyckoff position 4c is occupied by V. In Figure 4.16 (b), the −COHP is plotted for two independent V(4c)-Si bond in $V_3Mo_2SiB_2$. This type of bond provides only a few amounts of occupied antibonding states compared to the Mo(4c)-Si bond in $V_2Mo_3SiB_2$. There are only 15 of 32 V(4c)-Si bonds (47 %) showing occupied antibonding states. Hence, the V(4c)-Si bond in $V_3Mo_2SiB_2$ is more stable than the Mo(4c)-Si bond in $V_2Mo_3SiB_2$ as not only the antibonding interaction is smaller in the V(4c)-Si bond but also the amount of antibonding interaction is decreased.

These results of chemical bonding analysis represent a clearly explanation for the observed site preference of V on 4c site. While the Mo-Si bonds with Mo on the 4c site content antibonding states regardless of the amount of V, the unstable Mo-Si bonding situation is removed once V occupies the 4c site to make V-Si bonds with only small amounts of antibonding interactions near the Fermi level. Interactions such as V/Mo(4c)-B, V/Mo(4c)-V/Mo(16l), V/Mo(16l)-B and V/Mo(16l)-Si did not show any signs of instability and thus are not relevant for the present site preference phenomenon.

So, the DFT calculation clearly showed that alloying with V is profitable on the one hand in order to get a high density reduction but also to obtain stable T2 phases, since, in contrast to Mo, V induces a better enthalpy of formation and a higher chemical bonding stability.

4.3 Microstructures of solid state Mo-40V-9Si-8B alloys

The previous investigations on the powder material demonstrated the high potential of the Mo-40V-9Si-8B alloy in order to obtain a high density reduction while keeping the balance between Mo_{ss} phase and intermetallic phases but also in terms of increasing the stability of the T2 phase. Therefore this alloy composition was chosen for further investigations on the thermomechanical and oxidation properties.

X-ray diffraction measurements of the mechanically alloyed and thermally treated Mo-XV-9Si-8B powders already showed the expected phases $(Mo,V)_{ss}$, $(Mo,V)_3Si$ and $(Mo,V)_5SiB_2$ (Figure 4.9), where the $(Mo,V)_{ss}$ always formed the matrix phase. Hence, these aspects represent beneficial starting conditions to achieve an optimized microstructure (according to Berczik [19, 20]) after compacting.

Figure 4.17 (b) shows that the sintering process of the mechanically alloyed powder particles via FAST led to a similar microstructure compared with the thermally treated powders shown in Figure 4.8. The comparison with a FAST Mo-9Si-8B alloy (Figure 4.17 (a)) reveals similarities in the length scale, morphology and distribution of phases, as verified in Table 4.8. Apart from rare exceptions of larger $(Mo,V)_{ss}$ phase regions (Figure 4.17 (b)), the FAST Mo-40V-9Si-8B exhibits a very homogeneous microstructure, as also observed in earlier studies on PM Mo-9Si-8B alloys [70, 112] (see Chapter 2, Figure 2.2, page 9).

A special feature of the FAST Mo-40V-9Si-8B alloy could be shown with the help of an
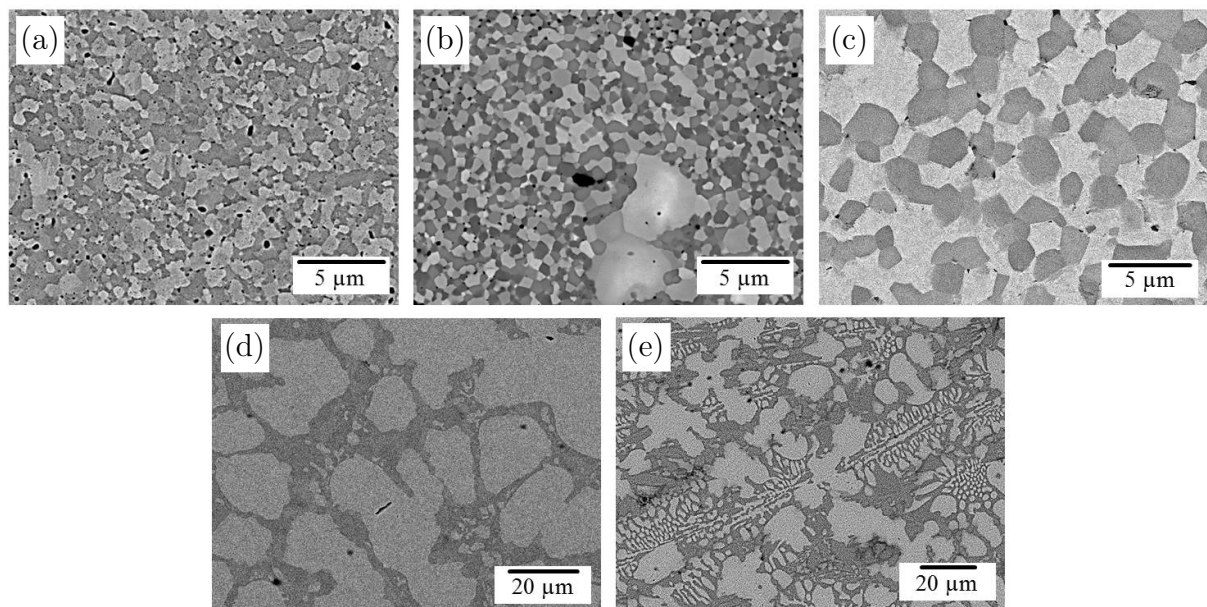
Figure 4.17: SEM images of compact materials (a) FAST Mo-9Si-8B (bright: Mo_{ss}, gray: Mo_3Si, dark: Mo_5SiB_2, black particles: SiO_2 [70, 100] (b) FAST Mo-40V-9Si-8B and (c) FAST and TT (1600 °C, 10 h) Mo-40V-9Si-8B (bright: $(Mo,V)_{ss}$, gray: $(Mo,V)_3Si$, dark: $(Mo,V)_5SiB_2$, black particles: V-oxide) (d) Arc Mo-9Si-8B (phase identification the same as in (a)) (e) Arc Mo-40V-9Si-8B (phase identification the same as in (b) and (c)).
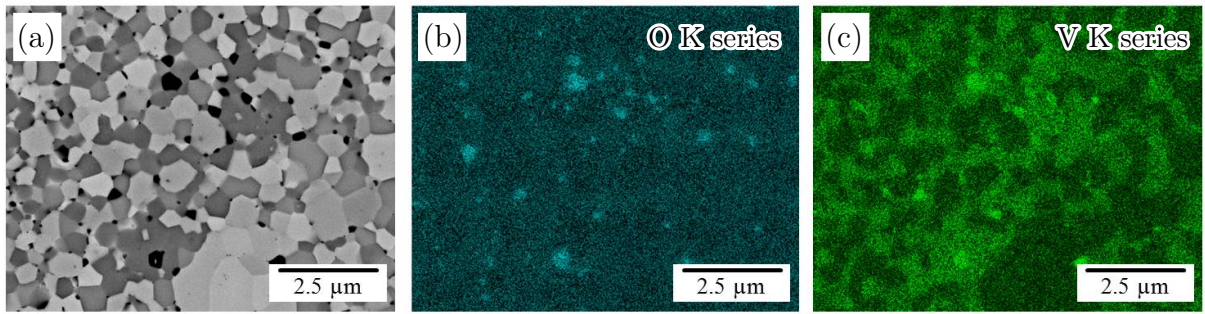
Figure 4.18: BSE image and element mapping of FAST Mo-40V-9Si-8B identifying the black spots as (b) oxygen- and (c) vanadium-rich particles.

EDS element mapping which is depicted in Figure 4.18. Instead of the SiO_2 particles detected in FAST Mo-9Si-8B [70, 100], vanadium-rich oxides were formed in the FAST Mo-40V-9Si-8B alloy. Hence, no SiO_2 could be detected, since the oxygen was completely gettered by V, which is known for its high affinity for oxygen [129]. This observation would explain the significantly increased oxygen concentration within the Mo-40V-9Si-8B alloy compared with Mo-9Si-8B (Table 4.8).

However, assuming grain boundary sliding, the very fine microstructure with grain sizes $< 1\,\mu$m (Table 4.8), would contribute to creep deformation, as previously demonstrated on a FAST Mo-9Si-8B alloy providing a grain size of $0.7\,\mu$m [70]. With regard to this, Jéhanno et al. [21] reported that a thermal treatment on a Mo-2.7Nb-8.9Si-7.7B alloy resulted in grain coarsening by one order of magnitude and therefore decreased the creep rate by one order of magnitude. Hence, the FAST Mo-40V-9Si-8B alloy was additionally thermally treated (TT) at 1600 °C for 10 h to obtain a grain coarsening which should provide a positive effect on the creep performance. The resulting microstructure is illustrated in Figure 4.17 (c) and shows much coarser grains, having an average size of $3\,\mu$m, compared with the FAST Mo-40V-9Si-8B alloy (Table 4.8). The black spots within the microstructures are again assumed to be V-oxide particles, according to Figure 4.18, indicating nonoptimized

Table 4.8: Microstructural features of alloys investigated compared with Mo-9Si-8B [70,178].

	Matrix phase	Amount of intermetallic phases, vol.%	Grain size, μm	Oxygen concentration, wppm	Density, $\frac{g}{cm^3}$
Mo-9Si-8B FAST	Mo_{ss}	51	0.7 [70]	1430 [70]	9.30
Mo-40V-9Si-8B FAST	$(Mo,V)_{ss}$	55	0.5 ± 0.1	6338 ± 570	7.73
Mo-40V-9Si-8B FAST and TT	$(Mo,V)_{ss}$	55	3 ± 1	4673 ± 33	7.52
Mo-9Si-8B Arc	IP	45	10 ± 3	$3 \dots 86$ [178]	9.53
Mo-40V-9Si-8B Arc	IP	52	5 ± 2	34 ± 9	7.87

deoxidation during processing. After the thermal treatment, the oxygen concentration within the FAST+TT Mo-40V-9Si-8B (4673 ± 33) alloy was in the same range as for FAST Mo-40V-9Si-8B (6340 ± 570 wppm). However, those concentrations are about four times higher compared with the FAST Mo-9Si-8B alloy (1430 wppm [70]). On the one hand, this was due to higher concentration of O_2 in the as-milled powders (Table 4.4), which cannot be reduced during the sintering process. On the other hand, higher porosity and increased concentration of V-oxide particles were observed in the FAST Mo-40V-9Si-8B alloy, caused by the higher affinity of vanadium to oxygen [129]. However, in general, such high oxygen contamination may induce embrittlement which would be unfavorable in terms of fracture toughness and brittle-to-ductile transition.

In contrast to the FAST material, the arc-melted alloys shown in Figure 4.17 (d) and (e) provide typical solidified microstructures with an intermetallic matrix and much coarser grain sizes (5...10 µm), which would be beneficial in terms of creep performance, according to [22]. The reference material (Figure 4.17 (d)) shows a microstructure which is similar to arc-melted Mo-9Si-8B reported in [179]. Generally, the Arc alloy Mo-40V-9Si-8B (Figure 4.17 (e)) provided a more homogeneous and fine-grained microstructure compared with Mo-9Si-8B. Hence, it is assumed that the lowered melting point of the Mo_{ss} decreases the difference in melting temperatures between Mo_{ss} and Mo_3Si/M_5SiB_2 so that the cooling time in the mushy zone is quite reduced and the growth of the primary solidified Mo_{ss} phase is limited. Due to the high affinity of V for Mo_3Si and M_5SiB_2, a shift of phase equilibrium could explain the higher amount of intermetallic phases (52 vol.%) compared with Arc Mo-9Si-8B (45 %). In this case, the V substitution had no significant effect on the
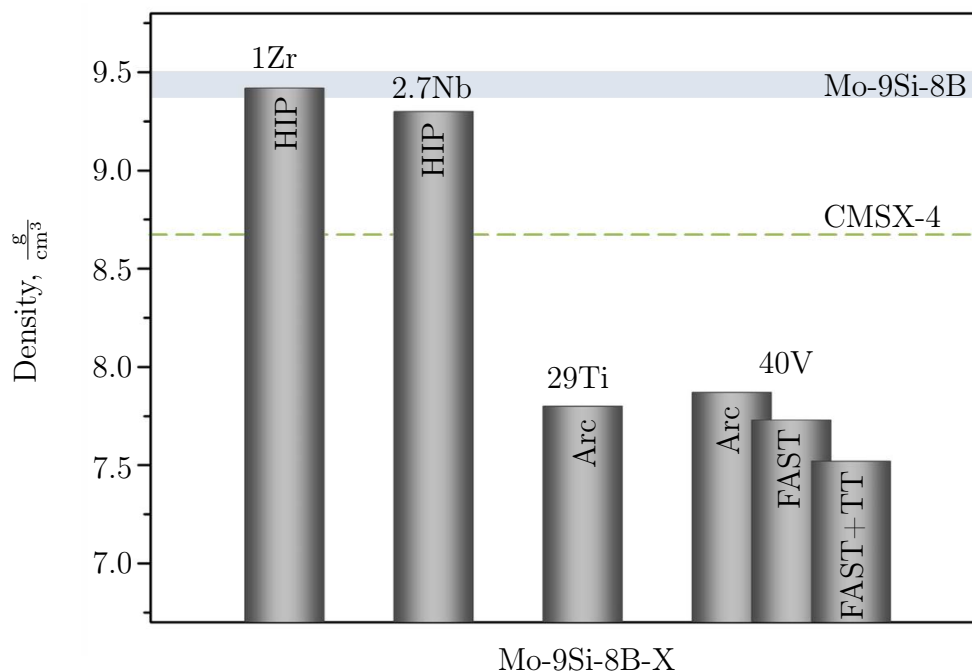

Figure 4.19: Density classification of Mo-40V-9Si-8B compared with other density optimized Mo-9Si-8B-X (X = 1Zr [70], 2.7Nb [21,67], 29Ti [96]) alloys as well as Mo-9Si-8B (PM, Cast) [17] and CMSX-4 [5,6].
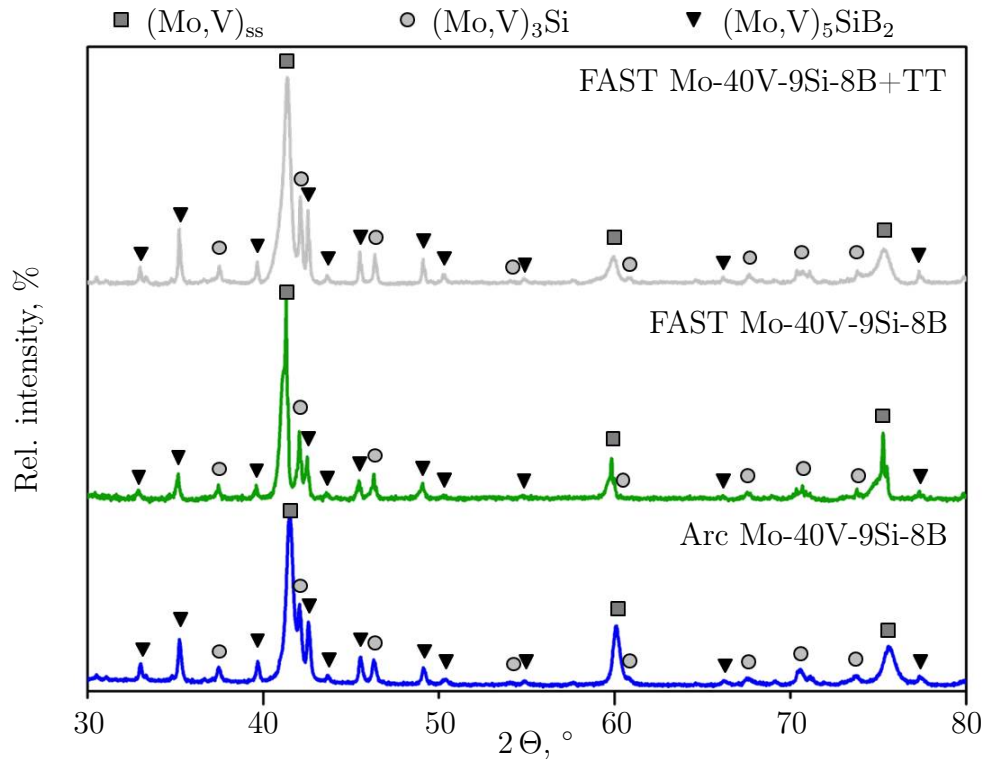
Figure 4.20: X-ray diffraction pattern for the Arc, FAST and FAST+TT Mo-40V-9Si-8B alloy.

oxygen concentration. In general, the oxygen contamination is considerably less than for the FAST alloys. This aspect represents a common problem for the PM route. Depending on the amount of silicon oxides and residual porosity, the higher oxygen contamination resulted in smaller densities compared with arc-melted alloys (Table 4.8).

However, as shown in Table 4.8, with density values ranging between $7.87 \frac{g}{cm^3}$ for the arc-melted Mo-40V-9Si-8B alloy and $7.52 \frac{g}{cm^3}$ for its FAST and thermally treated version, the density is reduced by more than 17% compared with the Mo-9Si-8B reference alloys. While small additions of Zr and Nb in Mo-9Si-8B provide less density optimization, depicted in Figure 4.19, the significant density reduction for the present alloys is in the same range as for Mo-9Si-8B-29Ti [96]. Hence, the Mo-40V-9Si-8B alloys fulfill one of the most important objectives of this thesis providing a significantly decreased density which is even smaller than for state-of-the-art CMSX-4 [5,6]. As illustrated with the microstructures, shown in Figure 4.17 all alloys consist of the ternary phase composition $(Mo,V)_{ss}$-$(Mo,V)_3Si$-$(Mo,V)_5SiB_2$ initially determined by EDS measurments. Additional X-ray diffraction measurements (Figure 4.20) and subsequent Rietveld refinement confirmed this phase construct, as expected from the powder analyzes (Figure 4.10). After thermal treatment, the alloy composition as well as the phase fractions remained the same.

4.4 Mechanical properties of Mo-40V-9Si-8B alloys

The microstructural investigation showed that it was possible to produce Mo-40V-9Si-8B alloys in the same way as Mo-9Si-8B materials while generating comparable or even more homogeneous/fine-grained microstructures. According to Figure 2.2 on page 9, the processing routes create typical microstructures having a significant effect on the room and high temperature characteristics. So, in the next step, the properties ranging from ambient up to high temperatures ($> 1000\,°C$) were determined for the novel Mo-40V-9Si-8B alloys and compared with other density reduced Mo-9Si-8B alloys.

4.4.1 Room temperature fracture toughness

In terms of the focused application as turbine engine materials, an acceptable fracture toughness is important in oder to create a damage-tolerant material [180]. Considering the fact that the room temperature fracture toughness of the intermetallic phases with $1.5\ldots3\,\mathrm{MPa}\sqrt{\mathrm{m}}$ [41] is significantly lower than for pure Mo ($24\,\mathrm{MPa}\sqrt{\mathrm{m}}$ [28]), it seems challenging to produce a ternary Mo-Si-B alloy providing an acceptable or high RT fracture toughness.

Previous investigations on the fracture toughness of PM Mo-9Si-8B alloys mainly originate from Vickers indentation fracture method [17, 44, 112], which is a useful technique to demonstrate a qualitatively comparison of alloys brittlenesses. However, this type of testing doesn't allow the determination of critical stress intensity factors K_{Ic} as they can only be calculated after three-point bending of notched or pre-cracked samples.

Hence, in order to classify the values of fracture toughness for the Mo-40V-9Si-8B alloys, other density reduced Mo-Si-B materials with different nominal compositions (close to Mo-9Si-8B) were chosen for comparison. Depending on the phase fractions and their distribution, critical stress intensity factors for Mo-Si-B alloys generally range between $6\,\mathrm{MPa}\sqrt{\mathrm{m}}$ and $16\,\mathrm{MPa}\sqrt{\mathrm{m}}$ [17, 45].

In Figure 4.21, the fracture toughness of the different alloys arranged with increasing $\mathrm{Mo_{ss}}$ phase fraction is given. The schematic illustrates that depending on the manufacturing process, the amount of $\mathrm{Mo_{ss}}$ phase as well as its continuity dominantly affect the materials' fracture toughness. Three main groups were marked within this schematic representing alloys having excellent ($> 12\,\mathrm{MPa}\sqrt{\mathrm{m}}$), acceptable ($8$–$12\,\mathrm{MPa}\sqrt{\mathrm{m}}$) or insufficient ($< 8\,\mathrm{MPa}\sqrt{\mathrm{m}}$) fracture toughness values. Additionally, the alloys were distinguished by their continuity of $\mathrm{Mo_{ss}}$ phase (black: discontinuous and white continuous $\mathrm{Mo_{ss}}$).

It is clearly shown that in case of insufficient fracture toughness the alloys always provide a discontinuous $\mathrm{Mo_{ss}}$ phase due to primary solidification during arc-melting or directional solidification (as predicted by Figure 2.2 in Chapter 2, page 9), but also by HIPing gas atomized powder particles, in case of Mo-8.9Si-7.7B [46]. However, this is not the only reason since other alloys having a discontinuous $\mathrm{Mo_{ss}}$ phase can even provide higher values. So, the grain size is also a decisive aspect in terms of crack propagation. Generally, the crack propagates through the brittle intermetallic phases and is trapped by the $\mathrm{Mo_{ss}}$ phase. In case of the alloys Mo-12Si-8.5B and Mo-12Si-10Nb-8.5B the small phase regions of $\mathrm{Mo_{ss}}$
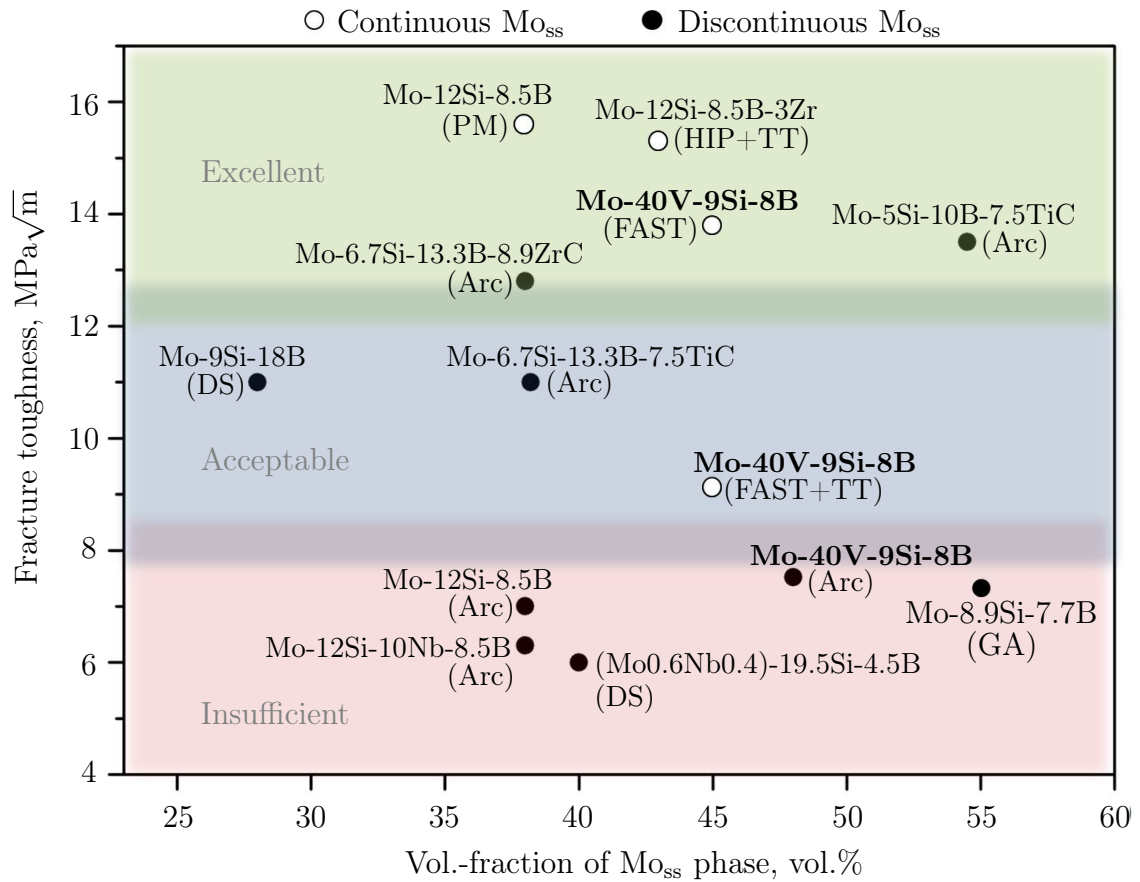
Figure 4.21: Comparison of fracture toughness K_{Ic} of Mo-40V-9Si-8B alloys with different Mo-Si-B alloys [48, 55, 61, 181–185].

phase do not have enough crack arresting capability, so that the crack is finally trapped by large Mo_{ss} phase regions with maximum sizes of $100\,\mu m$ and $50\,\mu m$ [181]. Hence, the alloy Mo-12Si-8.5B shows a higher fracture toughness than Mo-12Si-10Nb-8.5B due to the larger Mo_{ss} phase regions [181]. Therefore, the alloy composition (Mo0.6Nb0.4)-19.5Si-4.5B exhibits the lowest fracture toughness due to its small size of discontinuous Mo_{ss} phase less than $10\,\mu m$ [61]. The GA and HIPed alloy Mo-8.9Si-7.7B [46] benefits from the high amount (55 %) of Mo_{ss} phase, which forms regions having a size of around $20\,\mu m$.

In case of the arc-melted alloy Mo-40V-9Si-8B, the fracture toughness of $7.52\,\mathrm{MPa}\sqrt{m}$ represents an increased (Figure 4.21) level compared with the alloys mentioned before. This can be explained by the higher amount of Mo_{ss} phase as well as the homogeneously distribution of the large ($\sim 30\,\mu m$) ductile regions. In contrast, a highly improved value for fracture toughness was represented by the FAST variant of Mo-40V-9Si-8B, providing $13.8\,\mathrm{MPa}\sqrt{m}$. Compared with the alloys having insufficient fracture toughness values, this alloy benefited from its continuous Mo_{ss} phase which is not significantly reduced in toughness by the V substitution [161]. The advantage of the continuous Mo_{ss} phase was also shown for the alloy Mo-12Si-8.5B (PM) [68] and Mo-12Si-8.5B-3Zr (HIP+TT) [183] providing high values for fracture toughness as well.

According to Schneibel [68], it can be said, that the fracture toughness is not only de-
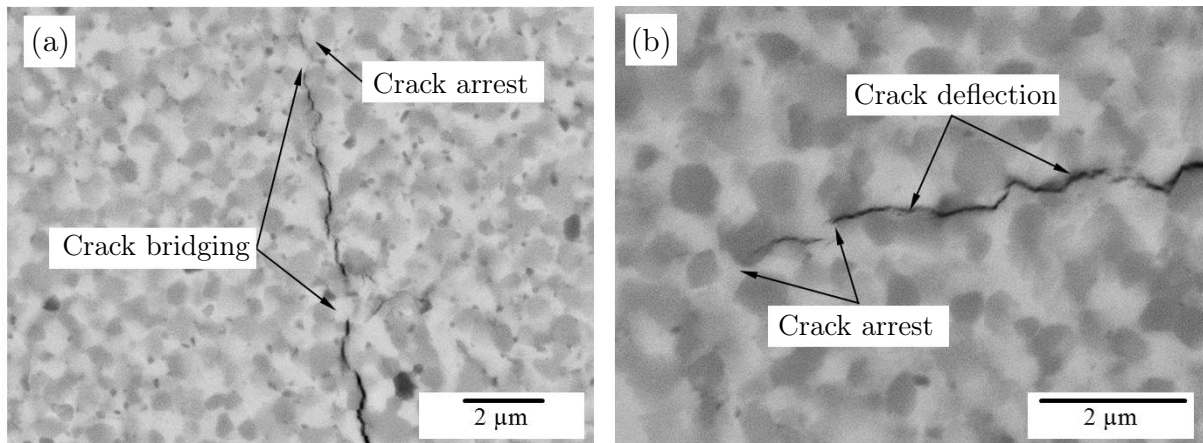
Figure 4.22: Crack propagation in FAST Mo-40V-9Si-8B (a) depicting crack bridging and arrest and (b) showing the crack deflection and interception.

termined by the volume fraction of the continuous Mo_{ss} phase, but also by its scale. Therefore, the FAST Mo-40V-9Si-8B alloy is affected by its very fine microstructure with a median size for Mo_{ss} of $0.5\,\mu m$ after FAST processing. As demonstrated in Figure 4.22, the crack propagates through the intermetallic phases but cannot be stopped by a larger Mo_{ss} phase region. Due to the crack interception through smaller Mo_{ss} areas, the crack loses energy the more often it passes the ductile phase. This is also known as crack bridging (Figure 4.22 (a)) which represents an effective toughening process in composite intermetallics [48]. Furthermore, crack deflection is shown which has also been identified in other fine-grained Mo-Si-B materials with homogeneous microstructures, e.g. in [183]. Hence, despite of the less amount of Mo_{ss} compared with FAST Mo-40V-9Si-8B, the fracture toughness of Mo-12Si-8.5B (PM) [68] and Mo-12Si-8.5B-3Zr (HIP+TT) [183] is higher due to the larger scale of the ductile phase. Especially in case of Mo-12Si-8.5B-3Zr (HIP+TT), the thermal treatment at $1800\,°C$ resulted in the formation of coarser Mo_{ss} regions having a size of around $1.2\,\mu m$ which were additionally improved in ductility by alloying with $3\,at.\%$ Zr [43,183]. Considering the aspect that both competing alloys provide densities of approximately $9\,\frac{g}{cm^3}$, the FAST Mo-40V-9Si-8B alloy is preferable due to combining a high fracture toughness and a highly reduced density of $7.73\,\frac{g}{cm^3}$. Furthermore, the fracture toughness of FAST Mo-40V-9Si-8B can be improved by optimizing the process parameters in order to reduce the contamination with oxygen.

Another improvement of the fracture toughness for FAST Mo-40V-9Si-8B might be induced by the thermal treatment resulting in coarser Mo_{ss} phase regions. Such a coarse-grained microstructure was reached after thermal treatment of the FAST Mo-40V-9Si-8B alloy at $1600\,°C$ for $10\,h$. However, the fracture toughness was decreased to $9.12\,MPa\sqrt{m}$ which might be explained by the following reasons.

During the thermal treatment, not only the size of the Mo_{ss} phase regions was increased but also the size of intermetallic phases, forming larger connected phase fields. Therefore, the Mo_{ss} appears less continuous and homogeneous affecting the crack propagation behavior. The trend of decreasing fracture toughness due to larger intermetallic phases was also shown for several PM Mo-Si-B alloys [44,112]. Another, influential aspect might be again the contamination with oxygen which is approximately as high as for the FAST

Mo-40V-9Si-8B. However, the consistent amount of continuous Mo$_{ss}$ phase, after thermal treatment, ensured a value of fracture toughness which is still acceptable.

As shown in Figure 4.21 there are further materials such as Mo-9Si-18B (DS) and TiC/ZrC-added (Arc) alloys having a discontinuous Mo$_{ss}$ phase and still provide acceptable or even excellent values for fracture toughness. In case of directionally solidified Mo-9Si-18B [61] it was shown, that the morphology of Mo$_{ss}$ phase is decisive as well. The lamellar structure is beneficial in terms of crack deflection along the Mo/T2 interface, especially, when the length of the Mo$_{ss}$ is perpendicular to the crack path. Then the crack has to deviate in order to follow the interface, around the ends of the lamellar Mo$_{ss}$ regions which results in a significantly improved fracture toughness. In case of the ZrC- and TiC-added alloys Mo-6.7Si-13.3B-8.9ZrC [184], Mo-5Si-10B-7.5TiC and Mo-6.7Si-13.3B-7.5TiC [182] fractographic results suggested that not only the ductile phase toughening by Mo$_{ss}$ phase but also an extra-toughening by the TiC/ZrC phase is responsible for the excellent fracture toughness values. So, generally it was reported that the fracture toughness improved with an increase in the volume fractions of the Mo$_{ss}$ and ZrC/TiC phases [182, 184].

The different cleavage mechanisms in the Mo-40V-9Si-8B alloys were also represented by their fracture surfaces after three-point flexure of notched samples, illustrated in Figure Figure 4.23. The FAST alloy of Mo-40V-9Si-8B shows predominantly transgranular but also intergranular fracture which was indicated by the crack propagation path in Figure 4.22. The fine-grained microstructure in this alloy (Figure 4.23 (a)) provided sharp changes in the stress intensity factors during crack extending through the corresponding phases, so that the mixed fracture mode represents the easiest path for crack propagation. The thermal treated variant of FAST Mo-40V-9Si-8B shows a mixed fracture mode as well, depicted in Figure 4.23 (b).

The micrograph in Figure 4.23 (c) shows regions of cleavage fracture corresponding mostly to the (Mo,V)$_3$Si and (Mo,V)$_5$SiB$_2$ intermetallic particles while the (Mo,V)$_{ss}$ phase predominantly shows intergranular fracture. The image indicated that transgranular cleavage fracture was dominant. Uneven surfaces and river patterns in Mo$_{ss}$ demonstrate evidence of plastic deformation through crack propagation, also shown in [182].
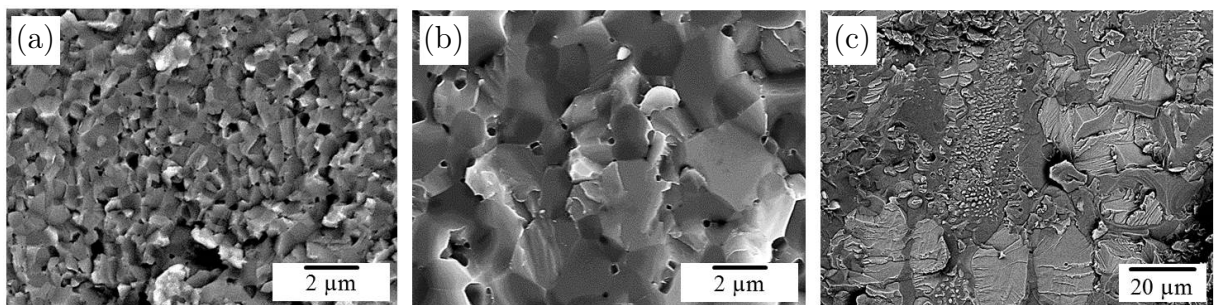

Figure 4.23: Fracture surfaces after three-point bending of notched samples of Mo-40V-9Si-8B (a) FAST, (b) FAST+TT and (c) Arc.

4.4.2 The brittle-to-ductile transition of FAST Mo-40V-9Si-8B

As demonstrated by the three-point bending tests of notched samples, the FAST alloy Mo-40V-9Si-8B provided an excellent fracture toughness at room temperature, due to its high fraction of continuous Mo_{ss} phase with finely distributed intermetallic particles. A mean-field homogenization of the tensile deformation by Krüger and co-workers [103] confirmed that the deformability of multi-phase Mo-Si-B alloys is mainly governed by the Mo_{ss} phase. Hence, the FAST Mo-40V-9Si-8B alloy offers a high potential in order to provide a decreased brittle-to-ductile transition temperature compared with Mo-9Si-8B.
In order to determine the BDTT of the present material, three-point bending tests were performed adopting the temperatures between RT and 1100 °C from previous investigations on PM Mo-Si-B alloys, reported in [57,103,112]. In Figure 4.24, the stress-outer fiber tensile strain data at three decisive temperatures (871 °C, 954 °C, 980 °C) were given for the FAST Mo-40V-9Si-8B alloy. The curves clearly illustrate the transition from brittle-to-ductile fracture behavior. At 871 °C, the yield strength is not achieved which indicates brittle fracture behavior, according to [107].
Increasing the temperature by ∼ 80 °C results in total plastic strain of 0.34 % (see Table A.5 on page 91) before failure. In this case, the yield strength is less than the maximum bending stress and therefore introduces the temperature region where plastic deformation occurs. The plastic strain of around 0.3 % at 954 °C represents a beginning of ductile behavior and is therefore supposed to be the brittle-to-ductile transition temperature, as also visualized in Figure 4.25. At higher temperatures, the plastic strain is assumed to be significantly increased as shown for 980 °C with a plastic deformation up to 1.4 %. If
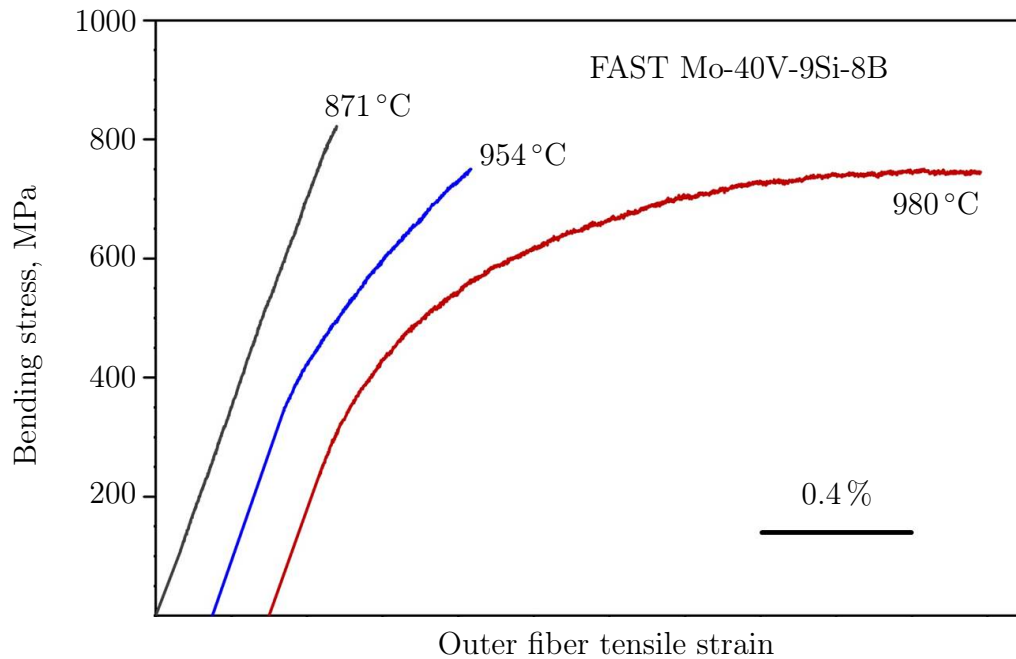

Figure 4.24: Stress-strain curves after three-point bending tests for Mo-40V-9Si-8B at 871 °C, 954 °C and 980 °C.
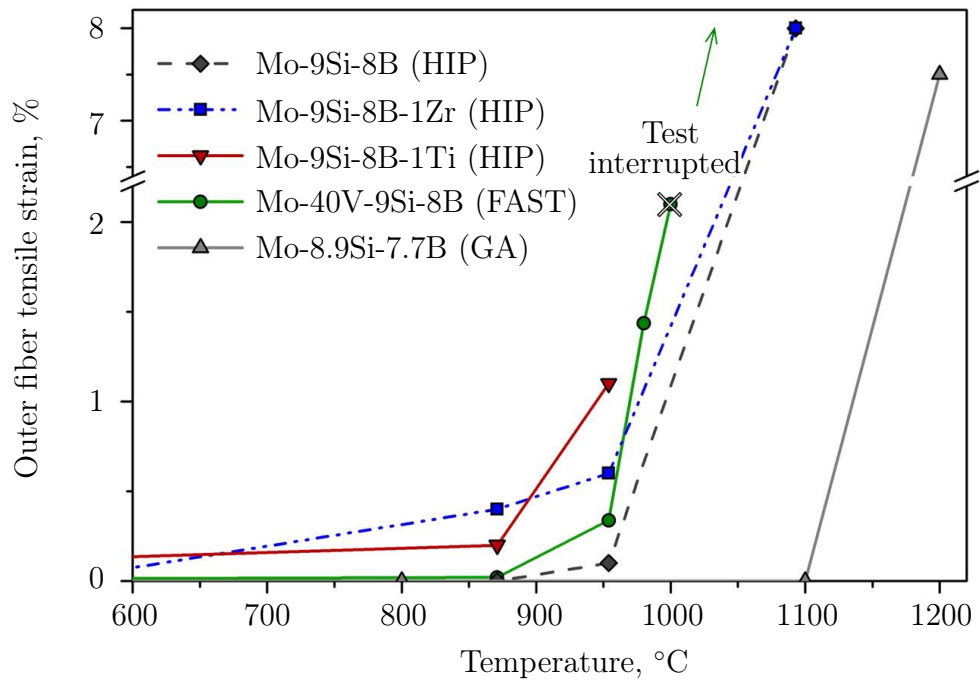
Figure 4.25: Outer fibre tensile strain of FAST Mo-40V-9Si-8B compared with PM Mo-Si-B alloys [46, 57, 103, 112] as a function of temperature. The brittle-to-ductile transition temperature (BDTT) is defined as the intersect of the curves with the temperature axis.

the temperature is further increased, the plastic strain is assumed to increase significantly, as shown in Figure 4.25. At 1000 °C the plastic strain increased again until the test was interrupted, since the measuring range of the elongation sensor reached its limit, before cleavage occurred. The plastic strain was expected to be significantly higher.

In order to classify these results, experimental data of PM Mo-Si-B alloys were used for comparison. The following Figures 4.25 and 4.26 depict the maximum bending stress as well as the strain of the outer fiber with increasing temperatures for Mo-40V-9Si-8B compared with Mo-9Si-8B (HIP), its Zr-/Ti-doped [57, 103, 112] version and gas atomized (GA) Mo-8.9Si-7.7B [46]. In Figure 4.25 the importance of an continuously distributed Mo_{ss} phase is revealed. In contrast to the mechanically alloyed and HIP/FAST alloys, the Mo-8.9Si-7.7B alloy was consolidated from atomized powders leading to a discontinuous Mo_{ss} phase after HIPing. So generally it is obvious that the BDTT, which is defined as the intersect of the curves with the temperature axis, decreased by more than 150 °C by switching from a discontinuous to a continuous Mo_{ss} matrix. The comparison of FAST Mo-40V-9Si-8B with the HIPed alloys seems to indicate they might yield identical BDTTs. This illusion might result from the lack of additional data between 900 °C and 1000 °C which would be important in order to localize the respective BDTT. In [112], it is assumed that the alloy with the highest fraction of Mo_{ss} matrix would yield the lowest BDTT. Generally, the HIPed Mo-9Si-8B-1Zr/-1Ti and the FAST Mo-40V-9Si-8B alloy provide an improved ductility compared with the reference alloy Mo-9Si-8B at 950 °C. According to Krüger [17], alloying with 1 at.% Ti showed the highest effect on the ductility
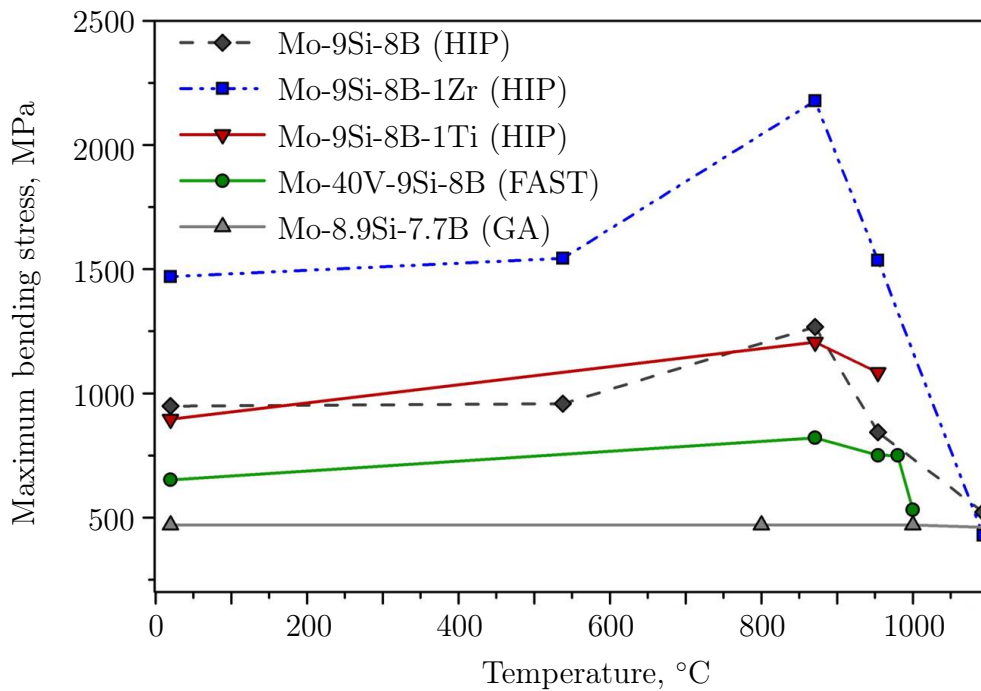
Figure 4.26: Maximum bending stress versus test temperature of FAST Mo-40V-9Si-8B compared with selected PM Mo-Si-B alloys, reported in [46, 57, 103, 112].

but is not assumed to further decrease the BDTT compared with Mo-9Si-8B-1Zr. The addition of Zr contributed to the decrease of BDTT due to the "cleaning effect" of the Mo_{ss} phase from detrimental oxygen and crack deflection at the Mo_{ss}/ZrO_2 interfaces. Furthermore, the grain boundaries in the Mo-9Si-8B-1Zr alloy are strengthened by the gettering effect of Zr, so that the fracture mode at RT changed from intergranular for Mo-9Si-8B to transgranular [103]. For the alloy FAST Mo-40V-9Si-8B, the ductility is negatively affected by the high oxygen contamination (6338 wppm) which leads to the formation of V-O-particles mainly decorating the grain and phase boundaries. Therefore, the BDTT can be significantly decreased if the oxygen content could be kept at a low level by an optimized de-oxidation during FAST processing.

As depicted in Figure 4.26, the Zr alloying also effects also significantly affected the strength of Mo-9Si-8B-1Zr resulting in the highest maximum bending stresses which occur twice as high as for Mo-9Si-8B. The diagram illustrates an slight increase of strength up to 871 °C for the MA HIP/FAST alloys until the typical decrease of strength with increasing temperatures occurs, i.e. after reaching the BDTT. As shown by the fracture surfaces in Figure 4.27, the intergranular cleavage at 871 °C changed to a mixed fracture mode with a higher amount of transgranular fracture at 980 °C. The FAST Mo-40V-9Si-8B alloy exhibits values of maximum bending stresses of 530 MPa – 820 MPa and is therefore positioned in between the curves of Mo-9Si-8B and Mo-8.9Si-7.7B. Here again, the present alloy suffers from oxygen contamination leading to a weakening of grain/phase boundaries due to SiO_2 particles. However, the average specific applied stress up to ~ 950 °C for FAST Mo-40V-9Si-8B (96 $\frac{J}{g}$) is in a similar magnitude of order as compared with Mo-9Si-8B (106 $\frac{J}{g}$) and Mo-9Si-8B-1Ti (118 $\frac{J}{g}$).
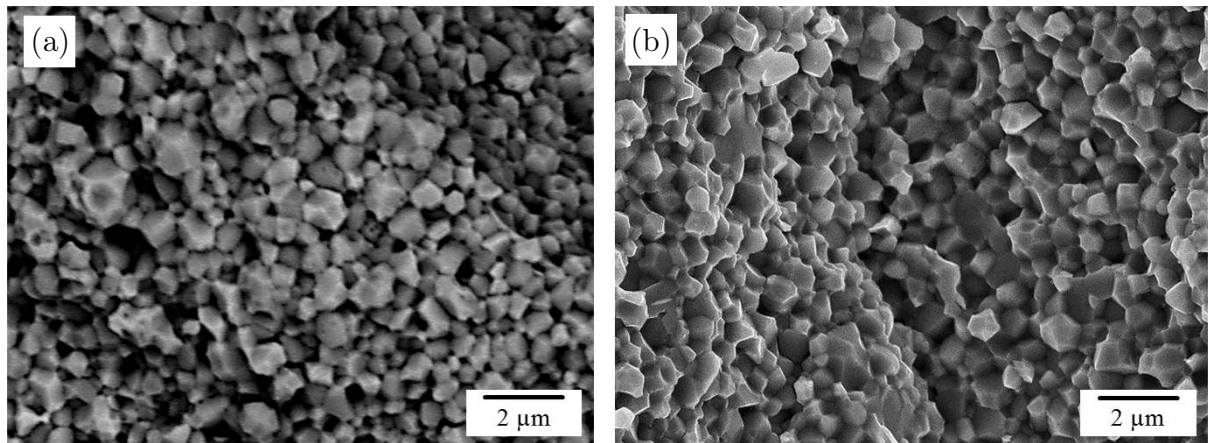
Figure 4.27: Fracture surfaces of FAST Mo-40V-9Si-8B after failure in three-point bending tests (a) at 871 °C and (b) at 980 °C.

4.4.3 The creep performance of Mo-40V-9Si-8B alloys

In addition to the significantly reduced density, the FAST Mo-40V-9Si-8B alloy in particular provides a competitive RT fracture toughness and promising BDTT. Another important issue for the focused high temperature applications is a good creep performance in order to provide a slow deformation of the turbine blade stressed from centrifugal force [1]. The creep behavior of the density optimized Mo-40V-9Si-8B alloys was performed by compressive creep tests with stresses ranging between 50 MPa and 200 MPa. As a typical operating temperature in high-pressure turbines and for reasons of comparison with previously analyzed creep data, the temperature of 1093 °C was considered here. Additionally, in order to determine the activation energies, the alloys were stressed with 200 MPa at 1000 °C, 1050 °C and 1093 °C, respectively. The results are shown in Figure 4.28, depicting the typical Norton and Arrhenius plot for the alloys investigated. The corresponding stress exponents and activation energies were calculated as described in Chapter 2.3 on page 22 ff. As depicted in Figure 4.28 (a), the FAST Mo-40V-9Si-8B alloy shows higher creep rates under similar creep loading compared with the FAST+TT and Arc variant. The stress exponent of the FAST alloy was found to be 2.8, indicating dominance of dislocation-controlled creep. At temperatures below 1200 °C, crept Mo-Si-B samples typically show dislocation activities only in the Mo_{ss} phase, which yields the lowest creep resistance in this multiphase system [124]. Since this phase forms the matrix phase in the FAST alloy, the creep response is mainly due to plastic deformation of Mo_{ss}. The very fine microstructure with grain sizes of 0.5 μm additionally contributes to creep deformation.

The approach of a thermal treatment for grain coarsening in order to improve the creep resistance works very well, as predicted by Jéhanno et al. [21]. The FAST+TT alloy showed a grain size of 3 μm after thermal treatment at 1600 °C for 10 h and therefore provides a six times higher grain size as the FAST alloy. Figure 4.28 (a) visualizes the improvement of the creep response by one order of magnitude due to grain coarsening. The stress exponent of $n \sim 2$ indicated predominantly grain boundary sliding. Hence, the coarser grains provide less phase/grain boundaries for sliding processes as compared with the FAST alloy. The
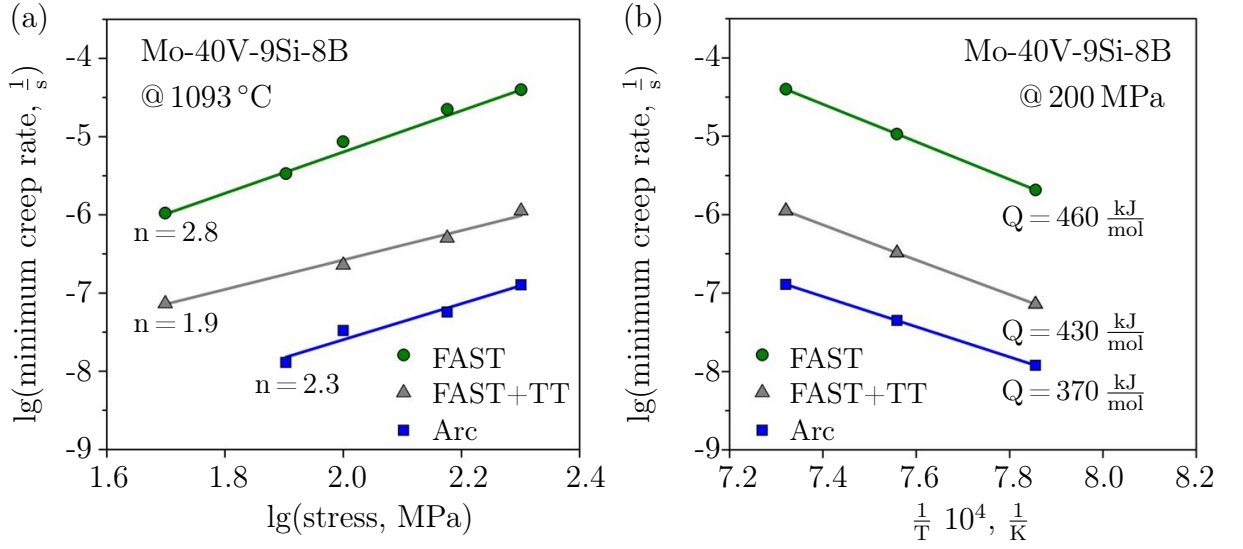
Figure 4.28: Creep performance of the Mo-40V-9Si-8B alloys, showing (a) the Norton plot with the calculation of the stress exponent and (b) the Arrhenius plot at 200 MPa including the determination of activation energy.

diffusion controlled creep has to be considered as well, since it is closely coupled to the grain boundary sliding. Since the volume diffusion (Nabarro creep) is expected at higher temperatures above $0.8\,T_{\mathrm{M}}$ [15], the diffusion along the grain boundaries (Coble creep) is assumed for the present alloys due to the testing temperatures of $1093\,°\mathrm{C}$ ($\sim 0.54\,T_{\mathrm{M}}$).

For both mechanisms, the grain size features a significant influence. In case of Coble creep the creep rate can be highly improved by coarser grain sizes according to the approximation $\frac{1}{\mathrm{d}^3} \sim \dot{\varepsilon}$, given in [15]. Hence, this effect also contributed to the creep performance of the FAST+TT alloy. Since the processes in this alloy were controlled by grain boundary sliding and diffusion creep, the alloy performed much more stable over the range of stress levels than the FAST alloy which was additionally influenced by dislocation creep. This behavior is represented by the slope of the curves in Figure 4.28 (a), expressed by their stress exponents, which decrease from 2.8 for the FAST alloy to 1.9 for FAST+TT Mo-40V-9Si-8B.

At last, the different creep mechanisms are represented by the activation energies shown in the Arrhenius plot in Figure 4.28 (b). For the FAST alloy $Q_{\mathrm{FAST}} = 460\,\frac{\mathrm{kJ}}{\mathrm{mol}}$ and its thermally treated version $Q_{\mathrm{FAST+TT}} = 430\,\frac{\mathrm{kJ}}{\mathrm{mol}}$ the activation energies do not differ strongly from each other, but are close to the activation energy for self-diffusion $Q_{\mathrm{SD}} = 405\,\frac{\mathrm{kJ}}{\mathrm{mol}}$ in Mo [186]. Accordingly, it shows that the creep behavior is mainly driven by the continuous $\mathrm{Mo_{ss}}$ phase. The higher activation energy of the FAST alloy might be explained by the predominant dislocation creep, since a higher activation energy is generally assumed for this creep mechanism. However, the activation energies are in good agreement with those ones reported by Jéhanno et al. [21] and Hochmuth et al. [100]. Their determined activation energies for alloys having a continuous $\mathrm{Mo_{ss}}$ matrix range between $444\,\frac{\mathrm{kJ}}{\mathrm{mol}}$ [21] and $560\,\frac{\mathrm{kJ}}{\mathrm{mol}}$ [100] for PM Mo-2.7Nb-8.9Si-7.7B and PM Mo-9Si-8B, respectively.

A superior creep performance was achieved in case of the arc-melted Mo-40V-9Si-8B alloy. The reason for this observation is attributed to the intermetallic matrix which is more creep

resistant [124] than the Mo_{ss} matrix of the FAST alloys. The creep exponent of $n = 2.3$ would imply that predominantly grain boundary sliding occurs. However, according to Schneibel [54], the assumption of inverse creep due to the intermetallic matrix complicates the explicit identification of the dominant creep mechanism. The intermetallic phases behave brittle forming cracks within the matrix phase, as shown by Hasemann et al. [22], since the begin to deform plastically is assumed at $T > 1200\,°C$. So, here again, the dislocation movement causing deformation should mostly be governed by the Mo_{ss} phase. This was confirmed by the activation energy $Q_{Arc} = 370\,\frac{kJ}{mol}$ which is close to the activation energy for self-diffusion in Mo [186]. The determined value is in very good agreement with the activation energies identified for arc-melted and directionally solidified Mo-Si-B alloys, reported by Hasemann et al. [22] and Schneibel [54]. Their alloys, providing a microstructure comparable with Arc Mo-40V-9Si-8B, showed activation energies between $345\,\frac{kJ}{mol}$ for arc-melted Mo-9.5Nb-12Si-8.5B [54] and $349\,\frac{kJ}{mol}$ for Arc/DS Mo-17.5-8B [187]. These authors also reported stress exponents near $n = 3$ when testing at temperatures between $1200\,°C$ and $1400\,°C$ [54]. This seems reasonable, since dislocation operating starts in Mo_3Si at $1220\,°C - 1320\,°C$, while T2 acts as the most creep resistant phase [34, 36]. Therefore, due to the lower testing temperature of $1093\,°C$ presented here, the alloy benefits from the creep resistance of the intermetallic matrix resulting in a reduced stress exponent of $n = 2.3$, which describes a more stable creep behavior over stress range investigated. Those conclusions clearly show the temperature dependence of the creep performance and indicate that the creep resistance of the present alloys will decrease at higher temperatures [36, 124]. In order to classify the creep performance of the density optimized Mo-40V-9Si-8B alloys, they were compared with other density reduced PM and Arc Mo-Si-B alloys as well as with the reference alloy Mo-9Si-8B and state-of-the-art CMSX-4. The exact creep rates and stress levels for the PM and solidified Mo-Si-B-X alloys are listed in Table A.6 and Table A.7 in the Appendix on page 92 and ff.

First, the FAST alloys are shown in Figure 4.29 visualizing a double-logarithmic plot of creep rate versus normalized applied stress at $1093\,°C$ compared with other PM alloys having a continuous Mo_{ss} matrix. Therefore, the creep response for the alloys shown in Figure 4.29 was assumed to be governed by the Mo_{ss} phase, respectively. Compared with the reference alloy Mo-9Si-8B (produced via FAST) [99], the FAST Mo-40V-9Si-8B alloy is slightly weaker under similar creep loading. Both alloys showed an ultrafine-grained microstructure with grain sizes less than $1\,\mu m$ which significantly contributed to creep deformation. As mentioned before, the additional thermal treatment at $1600\,°C$ for $10\,h$ caused a grain growth by about $80\,\%$ which improved the creep performance of the FAST Mo-40V-9Si-8B alloy by more than one order of magnitude (Figure 4.29). Obviously, the thermally treated variant of FAST Mo-40V-9Si-8B is able to compete with the more creep resistant alloys shown here. As depicted in Figure 4.29, the creep rates of FAST+TT Mo-40V-9Si-8B are very close to those achieved for Mo-2.7Nb-8.9Si-7.7B in the as-HIPed condition [21]. Due to their similar stress exponents of $n \sim 2$, grain boundary sliding is predominantly assumed. In case of Mo-2.7Nb-8.9Si-7.7B, a thermal treatment at $1700\,°C$ for $10\,h$ also resulted in an improved creep resistance due to grain coarsening (from $0.7\,\mu m$ to approximately $7\,\mu m$ for Mo_{ss}) by one order of magnitude [21]. Hence, it can be assumed, that additional grain growth would further enhance the creep resistance of the FAST+TT alloy, since its current grain size is about $3\,\mu m$. However, the alloys Mo-9Si-8B-1Zr and CMSX-4 show lower creep rates especially at lower stress levels compared with FAST+TT Mo-40V-9Si-8B, which
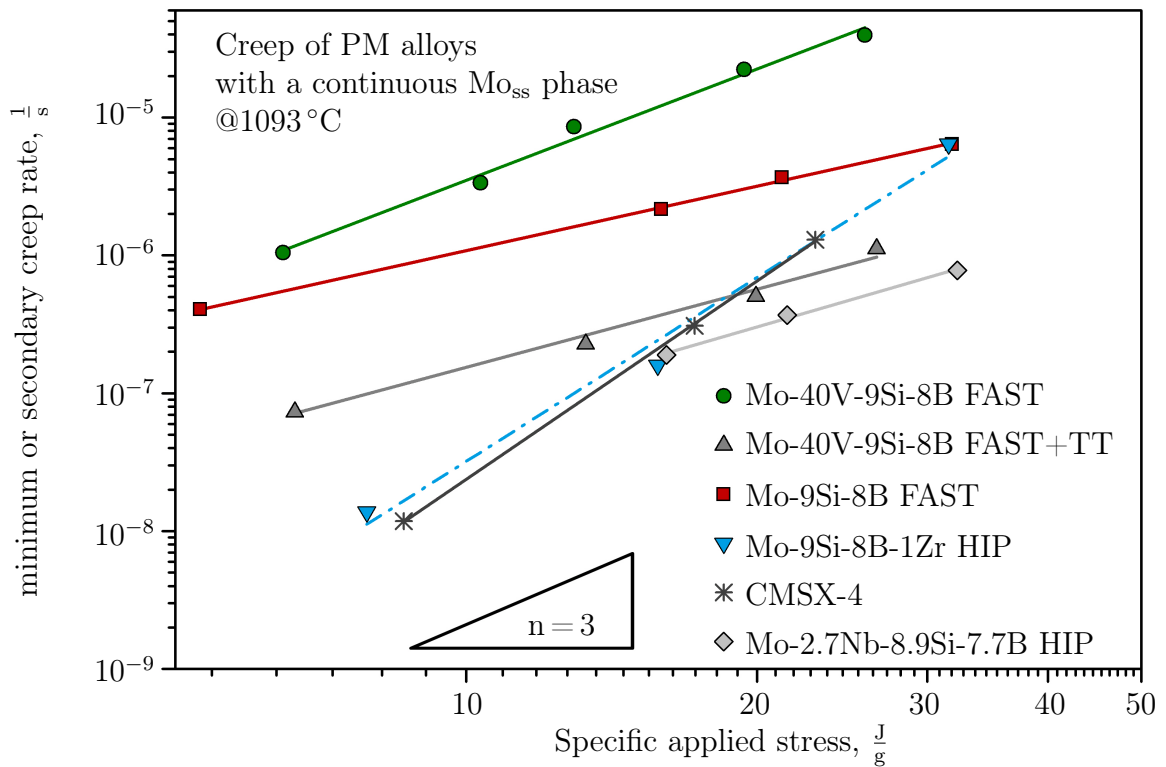
Figure 4.29: Comparison of FAST Mo-40V-9Si-8B alloys with creep data available from literature for FAST Mo-9Si-8B [99], HIPed Mo-9Si-8B-1Zr [70], PM Mo-2.7Nb-8.9Si-7.7B [21] and CMSX-4 [99, 188].

becomes inverse at higher stresses above $150\,\mathrm{MPa}$ (Appendix Table A.6). This behavior can be explained by the higher stress exponents $n > 3$ of Mo-9Si-8B-1Zr and CMSX-4 assuming predominantly dislocation controlled creep. So, the FAST+TT Mo-40V-9Si-8B alloy benefited from the more stable creep response due to the predominant grain boundary sliding. A superior creep performance was observed for the arc-melted Mo-40V-9Si-8B alloy, as described earlier. Generally, it has to be noted that the alloy composition of Mo-9Si-8B is favorable especially for the PM route. Hence, there is less scientific data available for the properties of arc-melted alloys for this special alloy composition. Therefore, as illustrated in Figure 4.30, the present alloy is compared with the most promising density reduced Mo-Si-B alloys, which also exhibits an intermetallic matrix. Additionally, the creep performance is again compared with CMSX-4. As depicted in Figure 4.30, the Arc Mo-40V-9Si-8B alloy provides an enhanced creep performance compared with state-of-the-art CMSX-4 [99, 188] and Mo-5Si-10B-7.7TiC (Arc+TT) [189, 190]. Even though the testing temperature for the TiC-added Mo-Si-B alloy was $1400\,^{\circ}\mathrm{C}$, the material yields excellent creep properties. In this case, two mechanisms contribute to the creep performance: phase boundary sliding between the hard T2 and (Ti,Mo)C phases and the $\mathrm{Mo_{ss}}$ phase, and dynamic recovery and recrystallization in $\mathrm{Mo_{ss}}$ [189]. The properties reported for Mo-Si-B-TiC reveals that alloys for ultra-high temperature applications with intermetallic matrix were usually tested at $1200\,^{\circ}\mathrm{C}$ or higher temperatures, since dislocation movement in $\mathrm{Mo_3Si}$ begins at that temperature regime [34, 36]. As depicted in Figure 4.30, the creep rates of the
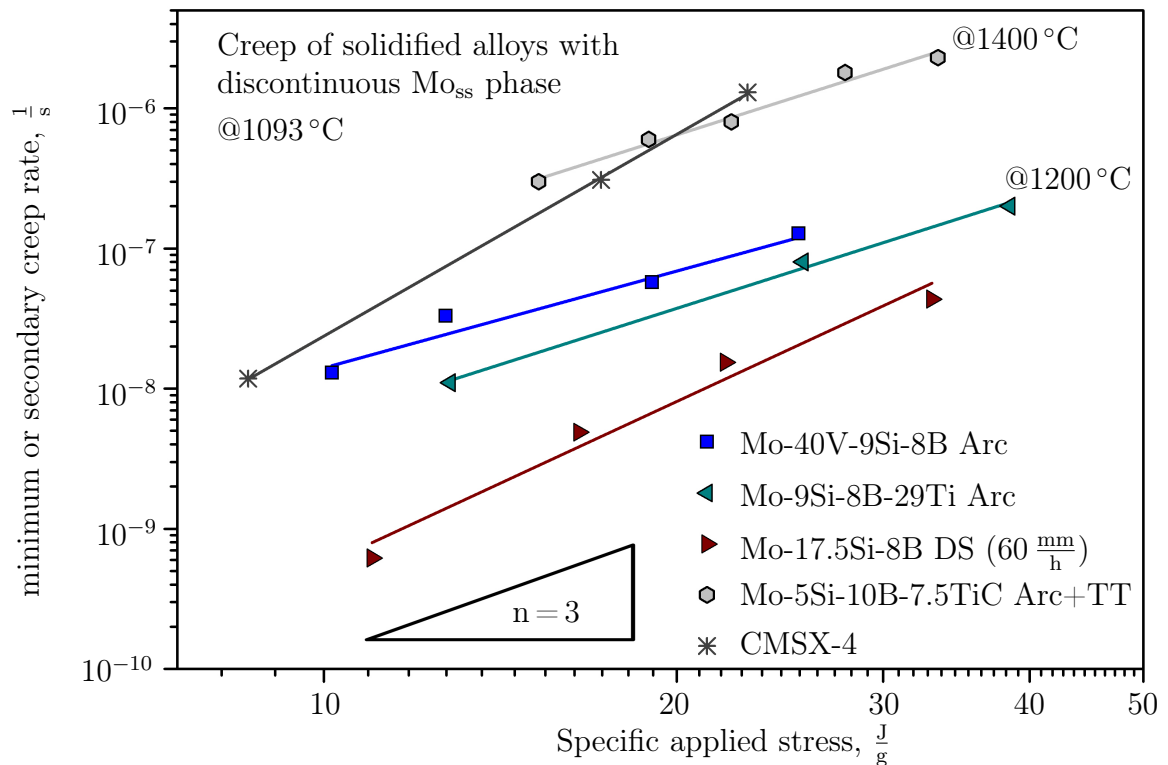
Figure 4.30: Comparison of Arc Mo-40V-9Si-8B with creep data available from literature for Arc Mo-9Si-8B-29Ti [105], DS Mo-17.5Si-8B [22], Arc Mo-5Si-10B-7.5TiC [189, 190] and CMSX-4 [99, 188].

Arc Mo-40V-9Si-8B alloy are in the same range as for the Mo-9Si-8B-29Ti alloy, which also yields a significantly reduced density of $7.8\,\frac{g}{cm^3}$ [105]. However, despite of higher testing temperatures (1200 °C), the alloy Mo-9Si-8B-29Ti shows a favorable creep behavior compared with Arc Mo-40V-9Si-8B. According to Azim [105] dislocation controlled creep ($n \sim 3$) can be assumed where a pinning effect of Ti_5Si_3 precipitates on dislocation motion is believed to be the reason for the improved creep resistance of Ti-containing alloys. A significantly increased creep performance was reported for the near-eutectic DS Mo-17.5Si-8B alloy which can be explained by the high amount ($\sim 70\,\% - 80\,\%$) of intermetallic matrix phase [187]. However, the major advantage of the Mo-Si-B-Ti and Mo-V-Si-B alloys is the dramatically decreased density - even below the density of Ni-based superalloys [98]. Hence, in terms of the focused application e.g. in turbine rotors, the reduction in weight would result in a decrease in the centrifugal force, which extends the creep lifetime of the material. Furthermore, it has been reported that Ti additions in Mo-Si-B alloys were able to stabilize the Mo_5Si_3 phase which had a positive influence on the oxidation resistance [96, 105]. However, in Mo-9Si-8B-29Ti the Mo_5Si_3 phase was replaced by Ti_5Si_3 (as depicted in Figure 2.4 (b), page 16), which degraded the oxidation resistance (relative to a Mo-9Si-8B), forming a relatively porous duplex layer with titania matrix enabling easy inward diffusion of oxygen [96]. In terms of the high affinity of vanadium for oxygen a degrading impact on the oxidation properties was expected for the present alloys, which will be focused in the next chapter.

4.5 Cyclic oxidation properties

Besides mechanical properties at ambient and elevated temperatures, the oxidation resistance is also a decisive factor for alloys which should be applied as structural materials for high temperature applications. The alloys investigated here are suspected to show weak performance against oxidation processes due to their high amounts of vanadium. According to the assumption described by Schneibel et al. [45], the arc-melted Mo-40V-9Si-8B alloy was chosen for cyclic oxidation experiments due to its intermetallic matrix. It should be mentioned that the following results represent a first orientation for the oxidation performance for this density optimized material class and do not consider profoundly oxidation kinetics.

As described in Chapter 3.7 on page 39, three different temperatures had been applied for cyclic oxidation experiments, namely 800 °C, 1000 °C and 1150 °C. In order to stress the material under the harshest conditions, the temperature of 800 °C was chosen because it is known as a critical temperature for "pesting". The elevated temperatures of 1000 °C and 1150 °C were then chosen as targeted application temperatures. The corresponding mass change curves for Arc Mo-40V-9Si-8B are shown in Figure 4.31 and compared with the reference alloy PM Mo-9Si-8B [191]. At 800 °C (Figure 4.31 (a)) both alloys suffer from catastrophic oxidation failure which is typical for Mo-Si-B alloys within the first $10\,\text{h} - 20\,\text{h}$ of testing in the temperature range between 700 °C and 800 °C [24, 126]. The Arc Mo-40V-9Si-8B shows less mass loss as the reference alloy at 800 °C. However, as depicted in Figure 4.32 (a), a very porous scale of oxides had been formed and no substrate material could be identified after the exposure at 800 °C, which indicates that the material was fully oxidized.

At temperatures $T \geq 1000\,°\text{C}$ a significant change of oxidation mechanism occurs for Mo-9Si-8B, as illustrated in Figure 4.31 (b) and (c). In case of Mo-9Si-8B, after an initial mass loss during the first hours, the slope of the curve reaches a plateau-like behavior which is in good agreement with the oxidation mechanism map in Figure 2.8 on page 26 according to
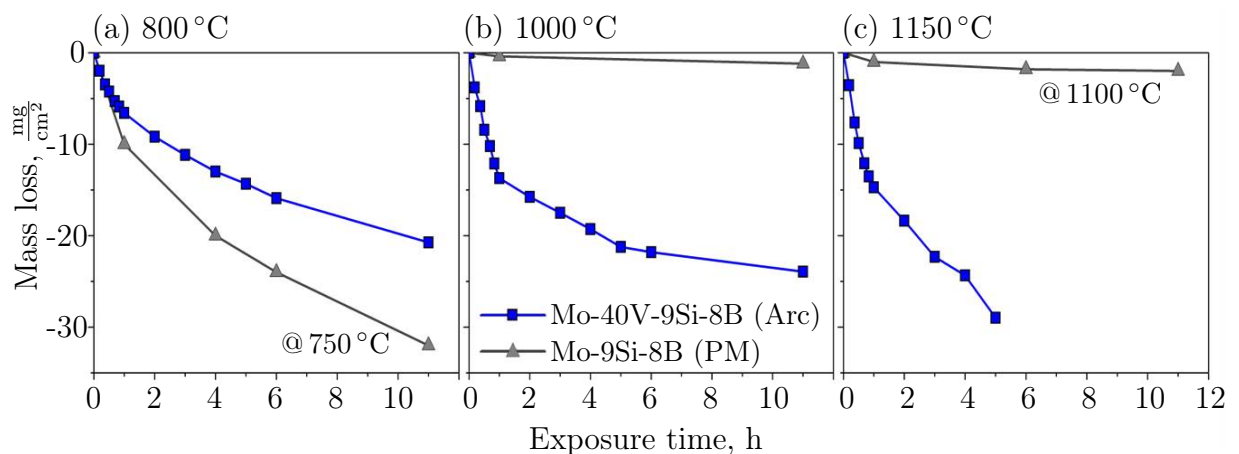

Figure 4.31: Specific mass change of Arc Mo-40V-9Si-8B (a) at 800 °C, (b) at 1000 °C and (c) at 1150 °C; compared with isothermal weight change of PM Mo-9Si-8B, reported in [191].
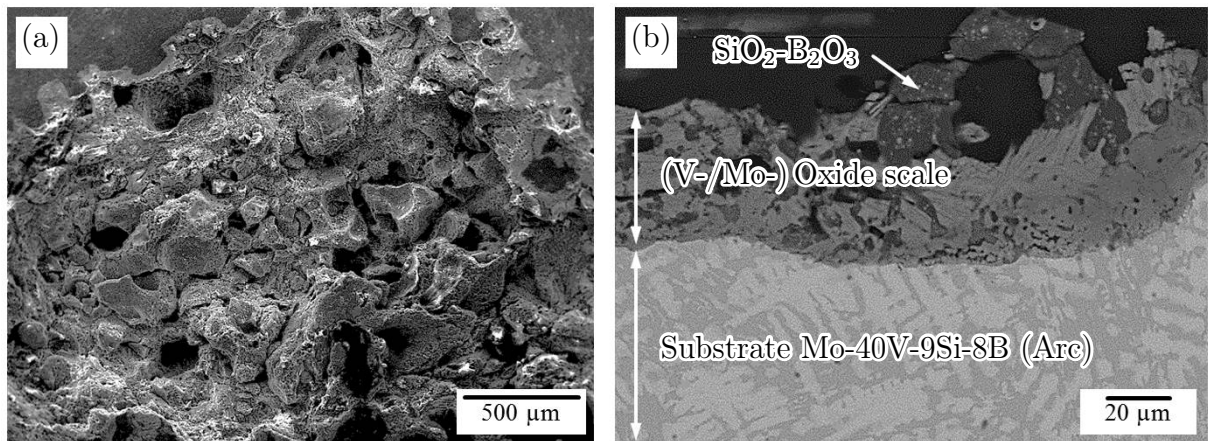
Figure 4.32: Oxide scale on Arc Mo-40V-9Si-8B after oxidation (a) entirely oxidized, i.e. catastrophic failure at $800\,°C$ and (b) oxide scale after oxidation at $1000\,°C$ (after $6\,h$ exposure).

Parthasarathy et al. [23]. For Arc Mo-40V-9Si-8B there is no passivation behavior observed at higher temperatures ($T \geq 1000\,°C$). As illustrated in Figure 4.32 (b), a discontinuous glass layer was formed and predominantly V-oxides were deposited at the surface. According to further microstructural investigations it is assumed that the glass scale flows off the surface due to its low viscosity. The decrease of the viscosity is attributed to the negative effects of V_2O_5 working as a network modifier or as a poor network former, as described in Chapter 2.4 on page 24 and reported by several authors [130–133]. Since Schneibel et al. [45] reported that small particles of Mo_{ss} phase within an intermetallic matrix would less affect the oxidation resistance, the insufficient behavior of Arc Mo-40V-9Si-8B can also be attributed to its microstructure. The formation of dendritical or extended regions of Mo_{ss} phase might contradict the formation of a continuous glass layer.

Methods for improving the oxidation resistance

In order to improve the oxidation performance of the arc-melted Mo-40V-9Si-8B alloy, small amounts ($3\,at.\%$) of Fe had been added, since Sossaman et al. [134] as well as Kumar et al. [135] reported its positive effect on the oxidation properties of Mo-Si-B alloys. The studies carried out by Sossaman et al. [134] targeted a change of the glass composition. Their aim was to reduce the viscosity of the glass layer in order to achieve rapid flow into non-protective Mo_{ss} regions and overall coverage of the substrate surface, resulting in the reduction of overall mass loss by MoO_3 volatilization. Thus, the investigations refer to the oxidation process according to Meyer et al. [37] (Figure 2.8 on page 26). Hence, Fe should work as a network modifier which increases the amount of non-bridging-oxides (NBO) and therefore reduces the viscosity of the glass scale. Kumar and co-workers [135] followed another decisive approach, investigating the effects of microstructural modifications due to minor Fe additions on the oxidation properties of Mo-Si-B alloys. They found out, that the inclusion of Fe in the A15 phase increased the amount of Si available for phase formation
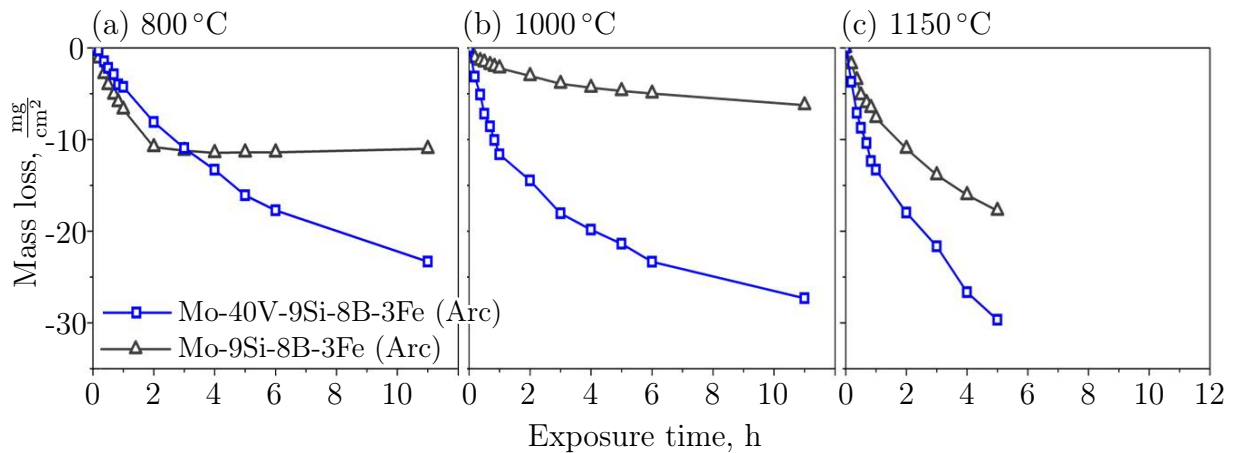
Figure 4.33: Specific mass change of Arc Mo-40V-9Si-8B-3Fe and Mo-9Si-8B-3Fe (a) at 800 °C, (b) at 1000 °C and (c) at 1150 °C.

and lead to an increase (9 %) of the A15 phase. This caused an improved formation of silicate glass on the materials' surface and thus prevented the loss of material in the critical oxidation phase (around 800 °C).

The Fe-alloyed compositions (Mo-40V-9Si-8B-3Fe and Mo-9Si-8B-3Fe) were also tested using cyclic oxidation tests at temperatures between 800 °C and 1150 °C. The resulting mass change curves are presented in Figure 4.33. While the Mo-9Si-8B-3Fe alloy shows a passivation behavior at 800 °C (Figure 4.33 (a)), the Mo-40V-9Si-8B-3Fe composition suffers from high mass losses for all temperatures tested. The performance for Mo-9Si-8B-3Fe at 800 °C seems untypical, as "pesting" usually occurs in this temperature region. Thus, those results indicate the positive effect of Fe on the oxidation resistance of arc-melted Mo-9Si-8B. Its slight increase of weight over time after an initial mass loss at 800 °C can be attributed to an oxide deposition on the layer surface, shown in Figure 4.34 (b) and (c). At higher temperatures $T \geq 1000$ °C a loss of the passivation is observed for Mo-9Si-8B-3Fe, depicted in Figure 4.33 (b) and (c), which was unexpected, as this represents the temperature region where passivation usually occurs.

Hence, the Mo-9Si-8B-3Fe alloy shows an oxidation performance which is different to those generally reported for Mo-Si-B alloys [23]. This can be attributed to the Fe-additions, decreasing the glass layer viscosity and resulting in a rapid formation of a protective glass scale. However, the decrease of viscosity automatically enables a higher oxygen diffusion at temperatures above 1000 °C, leading to mass losses despite the presence of a protective glass layer (Figure 4.34 (c)). Hence, at 1150 °C the increased diffusion rates impede the formation of an protective glass layer.

Even though, the Mo-40V-9Si-8B alloy provides a more fine-grained microstructure (similar to Figure 4.17 (e) on page 62) and a higher amount of intermetallic phases (53 %) as compared with Mo-9Si-8B-3Fe (similar to Figure 4.17 (d); amount of IP ~ 45 %), the alloy demonstrates an insufficient oxidation behavior. As depicted in Figure 4.34 (a), the layer formed at 800 °C on Mo-40V-9Si-8B-3Fe shows a more porous surface as compared with the glass scale on Mo-9Si-8B-3Fe (Figure 4.34 (b)). Since V_2O_5 is already suspected to reduce the glass viscosity, additional alloying with Fe seems to intensify this effect, so that no passivation can be achieved due to the significantly increased flowability of
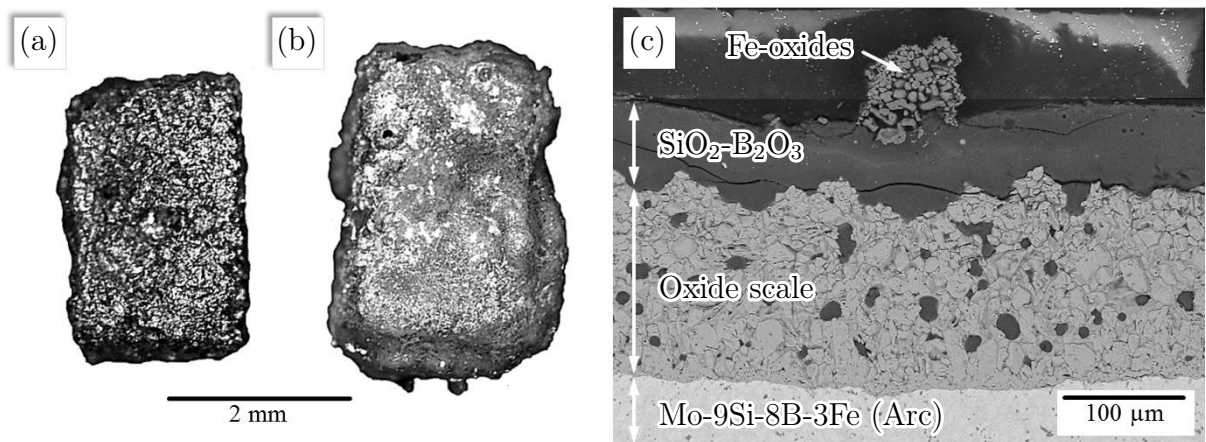
Figure 4.34: Oxide scales for Fe-alloyed Arc Mo(-40V)-9Si-8B after oxidation at 800 °C on (a) Mo-40V-9Si-8B-3Fe (b) Mo-9Si-8B-3Fe and (c) Mo-9Si-8B-3Fe after oxidation at 1000 °C.

the glass layer. Therefore it is assumed that alloying with Fe is not the most suitable approach to increase the oxidation resistance of Mo-40V-9Si-8B. Further approaches for improvement should therefore focus on the stabilization of the glass layer, e.g. by adding a strong network former such as Zr(-oxides) [192]. Furthermore, promising protective coatings could be considered in order to improve the oxidation resistance. Different coating systems and techniques, such as pack cementation [193, 194], magnetron sputtering [195] and plasma spraying [196] are discussed in the scientific community to control the oxidation properties of Mo-based alloys. Another recently developed coating system of pre-ceramic polymers (perhydropolysilazane - PHPS) was reported by Smokovych et al. [197, 198] and was handled as a promising candidate for active oxidation protection of Mo-Si-B alloys. Those PHPS coatings were found to provide a significant increase of oxidation resistance at 800 °C for Mo-Hf-B and Mo-Zr-B alloys [125].

5 Summary and conclusion

Since Mo-Si-B alloys are potential candidates for structural materials in stationary gas turbines or aircraft engines, the reduction of their density is one of the important issues for further development. Especially, the PM Mo-9Si-8B alloy shows a high potential since it combines an acceptable fracture toughness at ambient temperatures with excellent creep properties and oxidation resistance [19, 20]. However, its high density of 9.54 $\frac{g}{cm^3}$ [17] is a drawback in terms of flying applications. Therefore, the aim of this thesis was to optimize the density of the favorable composition Mo-9Si-8B which should be even smaller compared with state-of-the-art CMSX-4 (8.7 $\frac{g}{cm^3}$) [5, 6]. In order to realize this aim, an evaluation of possible lightweight elements helped to find potential alloying partners which could also improve the mechanical properties of this alloy class.

In terms of RT properties, the Mo_{ss} phase is a decisive component in Mo-Si-B alloys. Hence, first investigations focused on alloying elements like Ti, Zr and V evaluating their potential with respect to density reduction and solubility in the Mo_{ss} phase as well as their impact on solid solution strengthening. The Mo-5X (X = Zr, Ti, V) alloys were characterized by microstructure analysis, microhardness measurements, constant displacement tests in the compressive mode between room temperature and 1100 °C as well as three-point bending tests at RT. The results indicated vanadium to be a potential alloying partner that can entirely be solved in Mo_{ss} phase. A competitive strength-ductility relation at room temperature was shown compared with the Ti-alloyed material, i.e. slightly reduced strength and plastic deformability. In contrast, higher strength compared with V-added alloys but poor ductility was demonstrated by alloying with Zr due to second phase formation resulting from limited solubility in Mo.

In a next step, the advantageous features of vanadium were transferred on alloying concepts for ternary Mo-Si-B alloys. Therefore, initial studies were carried out on mechanically alloyed and thermally treated Mo-9Si-8B powders with varying vanadium concentrations (10, 20, 30, 40 at.%). The comparison of the resulting microstructures indicated that the fraction, morphology and distribution of Mo_{ss} phase appears independent of the V concentrations. An X-ray diffraction analysis enabled that the typical phase construct of Mo_{ss}-Mo_3Si-Mo_5SiB_2 was formed after thermal treatment. Rietveld refinement additionally confirmed that V was soluble in all three phases within the triangle, which means that the Mo-10...40V-9Si-8B alloys were composed of $(Mo,V)_{ss}$, $(Mo,V)_3Si$ and $(Mo,V)_5SiB_2$.

Those analyses also pointed out, that vanadium had a strong affinity to occupy the transition metal positions in $(Mo,V)_5SiB_2$ and at least, for alloy Mo-40V-9Si-8B, preferred the 4c Wyckoff position. These observations could be reasonably explained by means of density functional theory (DFT) calculations on $V_yMo_{5-y}SiB_2$ phases. The lattice and density parameters from the structural relaxation agreed very well with those experimentally found, illustrating the decrease of the lattice volume of unit cell and density of T2 with

increasing V concentrations. The calculations on the enthalpy of formation confirmed that for $V_yMo_{5-y}SiB_2$ in terms of energy the Wyckoff position 4c favored vanadium. So, furthermore the coordination environment as an influential aspect was considered by analyzing the chemical bonding situation for V and Mo on Wyckoff 4c position. It was found that Mo on the Wyckoff site 4c destabilized the chemical bonding to Si, while the occupation of V on 4c removed the unstable chemical bonding situation and therefore contributed to the stability of T2 phase.

The effects of such vanadium alloying on the mechanical properties of Mo-9Si-8B were derived from field assisted sintered (FAST)/ FAST+thermally treated (TT) and arc-melted (Arc) Mo-40V-9Si-8B alloys, featuring a density reduction by more than 17 %. Microstructural investigations on the compact materials showed that the desired three-phase compositions of $(Mo,V)_{ss}$-$(Mo,V)_3Si$-$(Mo,V)_5SiB_2$ were formed after processing. While the FAST Mo-40V-9Si-8B alloy exhibited a very fine-grained ($\bar{d} = 0.5\,\mu m$) microstructure with continuous Mo_{ss} phase, the arc-melted variant showed a coarser microstructure ($\bar{d} = 5\,\mu m$) due to primary solidification of Mo_{ss} phase resulting in an intermetallic matrix. A subsequent thermal treatment on FAST Mo-40V-9Si-8B at 1600 °C for 10 h resulted in a grain-coarsening by 80 % ($\bar{d} = 3\,\mu m$).

In terms of material characterization at ambient temperatures, those ternary alloys were tested in terms of room temperature (RT) fracture toughness. Three-point-bending of pre-notched samples showed that the FAST Mo-40V-9Si-8B alloy provided an excellent fracture toughness of $13.8\,MPa\sqrt{m}$ which is competitive to other Mo-Si-B alloys with a Mo_{ss} matrix phase. However, the Arc and FAST+TT variant of Mo-40V-9Si-8B showed decreased values for fracture toughness between $7\,MPa\sqrt{m}$ and $9\,MPa\sqrt{m}$, which was mainly attributed to the oxygen contamination during PM processing and the intermetallic matrix in case of the arc-melted alloy.

Due to the promising behavior of FAST Mo-40V-9Si-8B at RT, this alloy composition was tested by three-point bending at elevated temperatures. The results indicated that the brittle-to-ductile-transition occurs at ~ 950 °C which was in good agreement with the BDTT of other PM Mo-Si-B alloys. It was assumed that the BDTT could be further decreased if the oxygen contamination (6338 wppm) would be reduced.

In order to estimate the high temperature behavior, the creep performance for the present alloys was studied at 1093 °C. Their creep response was mainly governed by the Mo_{ss} phase, as derived from the resulting activation energies (360–460 $\frac{kJ}{mol}$). It could be shown that the arc-melted alloy of Mo-40V-9Si-8B provided a superior creep resistance due to its intermetallic matrix. The FAST alloy therefore suffered from predominant dislocation creep within the Mo_{ss} phase. However, in case of FAST+TT Mo-40V-9Si-8B, it was shown that a grain coarsening of 80 % resulted in a decrease of creep rates by more than one order of magnitude. Therefore, the creep performance became competitive to those achieved from other density optimized PM Mo-Si-B alloys and CMSX-4. It was concluded that the highly reduced density ($\sim 7.8\,\frac{g}{cm^3}$), which is even smaller compared with CMSX-4 ($\sim 8.7\,\frac{g}{cm^3}$) [5,6], represented a huge advantage of this alloy class. In terms of the focused applications e.g. in turbine engines, the reduction in weight would lead to a decrease in centrifugal forces, which finally extends the creep lifetime of the material.

As the last fundamental part of the high temperature material characterization, the oxidation properties were tested via cyclic oxidation tests between 800 °C and 1150 °C. The results confirmed the initial assumption that V could impair the oxidation resistance due

to its high affinity for oxygen [129]. The Arc Mo-40V-9Si-8B alloy suffered from oxidation failure for the temperatures tested, which was attributed to the negative effects reported for V_2O_5 [130–133]. It could also be shown that additional alloying with Fe did not yield the desired improvement of oxidation resistance, as initially reported for Mo-Si-B alloys [134, 135]. Therefore, different coating strategies have to be considered in order to control the oxidation performance.

It can be concluded, that vanadium is definitely a high potential alloying partner for Mo-Si-B alloys, which is able to optimize the density while providing competitive mechanical properties at ambient and even at high temperatures. However, there is still room for optimization, so further work is required for ongoing alloy development.

Future prospects

A basic problem which is known from PM processing is the contamination with oxygen, which is quite more critical for those V containing alloys. Generally, high oxygen concentrations were reported for the FAST alloys. TEM investigations could help to find out, where and in which form the oxygen (or oxygen containing compounds) is deposited within the microstructure. The oxygen concentration could be decreased by working with higher purity powders and especially by optimizing the process parameters for field assisted sintering in order to ensure an adequate deoxidation. A significantly reduced oxygen concentration could hinder an embrittlement and would therefore improve the fracture toughness and lower the BDTT of PM Mo-V-Si-B alloys. Referring to this, a very obvious approach would be the overall reduction of vanadium concentration within the alloy. Therefore, it would be profitable to study the properties of compact Mo-30V-9Si-8B, while this composition also yielded a high density optimizing potential (approximately higher than 10 %).

Additional alloying with $0.5 - 1$ at.% Zr could also result in advanced mechanical properties due to its gettering effect for oxygen which might also be beneficial in terms of oxidation resistance. The general problem of insufficient oxidation resistance could be enhanced by applying polymer-derived ceramic coatings.

Since the alloys investigated here were only tested in compressive creep mode, another important issue would be the testing of tensile creep which includes the application-related strains and damage mechanisms, e.g. the formation of micropores. These tests are planned in cooperation with the department of metallic materials of Bayreuth university. Creep tests at higher temperatures beyond 1093 °C would also be interesting, as a significant increase of creep rates is expected.

A Appendix

Binary alloy phase diagrams
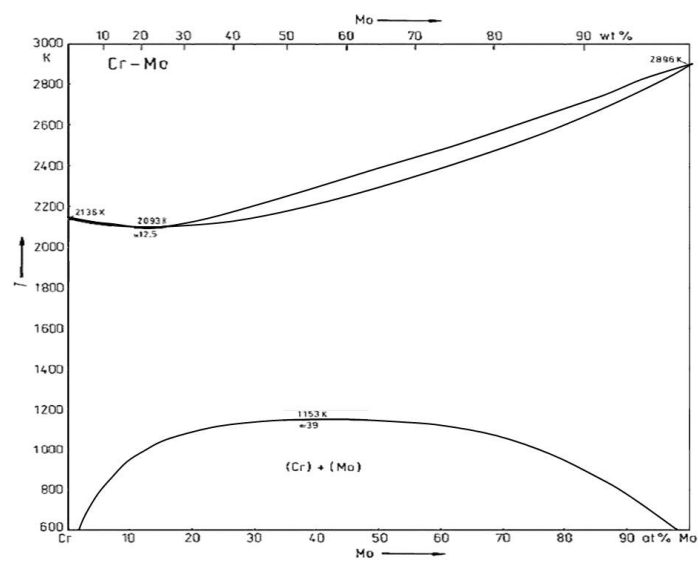
Figure A.1: Binary phase diagram of Mo-Cr [78].
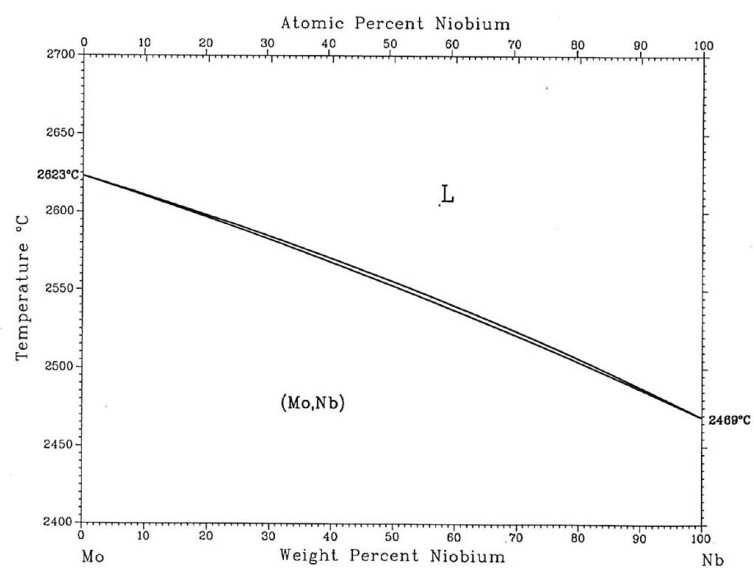
Figure A.2: Binary phase diagram of Mo-Nb [79].
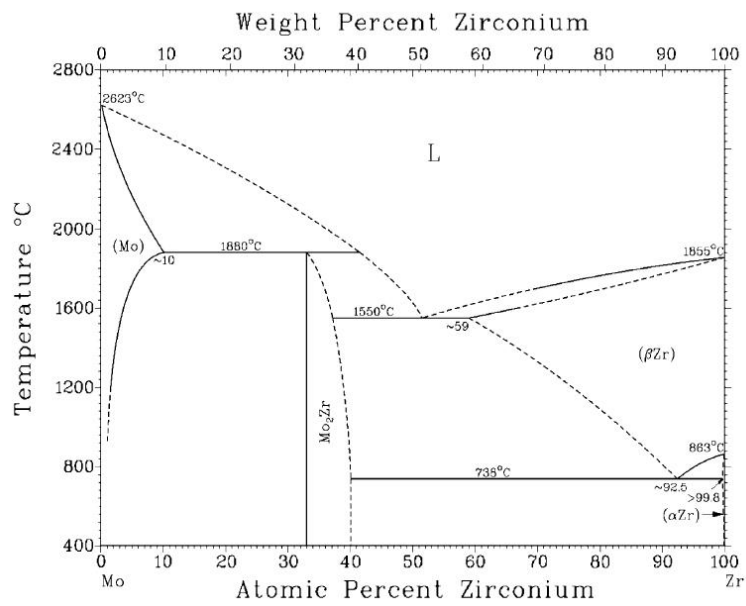
Figure A.3: Binary phase diagram of Mo-Zr [79].
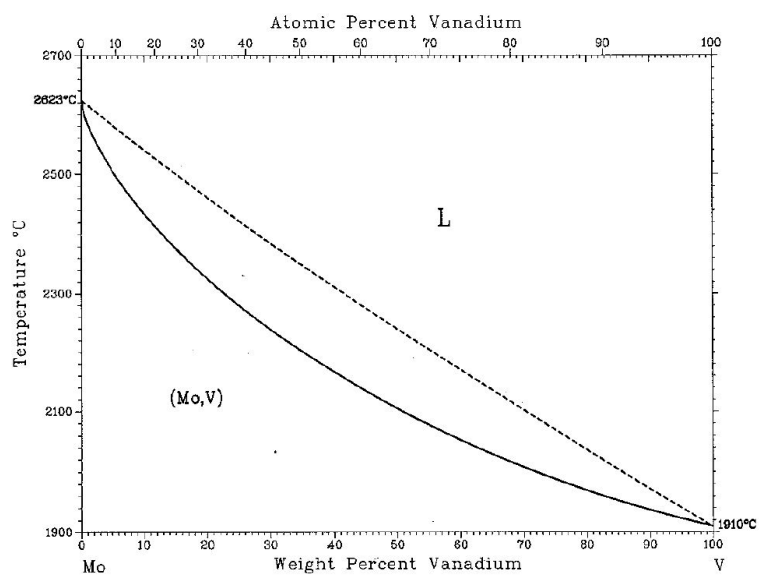
Figure A.4: Binary phase diagram of Mo-V [79].
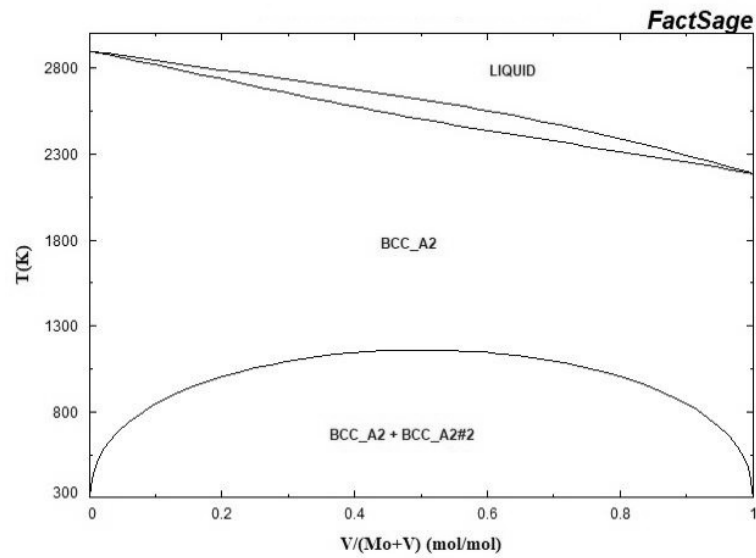
Figure A.5: Binary phase diagram of Mo-V from FactSage showing a miscibility gap [86].
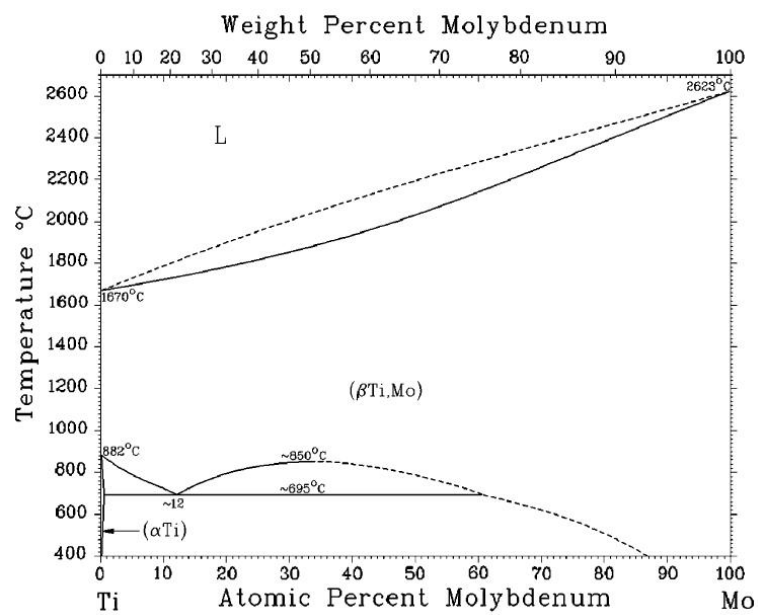
Figure A.6: Binary phase diagram of Mo-Ti [79].

Solid solution hardening in Mo-5X alloys

Table A.1: Parameters used for calculation of solid solution hardening.

	Mo	Ti	V	Zr
Shear modulus [16], GPa	130	44	47	26
Alloy compositions, at.%		Mo-5Ti	Mo-5V	Mo-Zr
Initial concentration (c_1) of dissolved elements in pure Mo	0			
Concentration of dissolved alloying elements (c_2) in Mo_{ss} (based on EDS measurements)		0.0523	0.0568	0.0406
Lattice parameter of pure Mo, Å (based on Rietveld refinement)	3.147			
Lattice parameter of Mo_{ss}, Å (based on Rietveld refinement)		3.148	3.142	3.158
Constants	$\alpha_d = 15$	$Z = 550$	$M = 3.06$	

DFT calculation

Table A.2: Experimental and DFT calculated work lattice parameters and resulting density for $V_yMo_{5-y}SiB_2$ phases, $*\frac{1}{2}a$ of 2x2x1 supercell.

		Lattice parameters, Å		Volumetric mass density, $\frac{g}{cm^3}$	
		DFT	Experimental	DFT	Experimental
Mo_5SiB_2	a	6.046	6.027 [176]	8.65	8.73
	c	11.116	11.067 [176]		
VMo_4SiB_2	a	5.971	-	8.14	-
	c	11.081	-		
$V_2Mo_3SiB_2$	a	5.957*	-	7.49	-
	c	10.976	-		
$V_3Mo_2SiB_2$	a	5.885*	5.870	6.94	7.05
	c	10.908	10.883		
V_4MoSiB_2	a	5.863	5.923	6.24	6.19
	c	10.823	10.965		
V_5SiB_2	a	5.786	5.81 [174]	5.60	5.55
	c	10.776	10.79 [174]		

Mechanical testing

Table A.3: Results of compression tests at RT, 800 °C and 1100 °C for Mo-X alloys, including the standard deviation (SD) and literature data.

Alloy at.%	Compressive yield strength, MPa			Compressive strength, MPa			Plastic strain %		
	RT	800	1100	RT	800	1100	RT	800	1100
Mo-5Ti	412	135	76	967	256	299	5	16	21
± SD	63	50	9	167	40	127	0.5	1.5	4
Mo-5V	318	169	158	821	350	275	8	12	17
± SD	33	12	3	133	45	37	0.5	4	0.5
Mo-5Zr	664	537	255	1312	578	735	4	8	10
± SD	55	93	-	42	195	-	0.5	1	0.1
				Tensile strength, MPa			Ref.		
				RT	871				
Mo-1Ti				670	-		[166]		
Mo-5Ti				517	275		[74]		
Mo-1.5V				586	275		[74]		
Mo-0.1Zr				531	241		[74]		

Table A.4: Results of three-point bending tests at RT for Mo-5X alloys.

Alloy, at.%	Maximum bending stress, MPa	Outer fiber tensile strain, %
Mo-5Ti	488 ± 48	1.3 ± 0.1
Mo-5V	407 ± 28	0.1
Mo-5Zr	265 ± 30	0

Table A.5: Results of three-point bending tests from RT up to 1000 °C and literature data for Mo-Si-B-X alloys.

Alloy, at.%	Maximum bending stress, MPa								Ref.
	RT	538	871	954	980	1000	1093	1200	
Mo-40V-9Si-8B (FAST)	652	-	821	751	750	531*	-	-	-
Mo-9Si-8B (HIP)	949	958	1268	843	-	-	522	-	[17]
Mo-9Si-8B-1Ti (HIP)	896	-	1206	1084	-	-	-	-	[17]
Mo-9Si-8B-1Zr (HIP)	1470	1544	2177	1536	-	-	428	-	[17]
Mo-8.9Si-7.7B (GA)	470	-	470	-	-	470	-	450	[46]
Outer fiber tensile strain, %									
Mo-40V-9Si-8B (FAST)	0	-	0.02	0.34	1.44	2.10*	-	-	-
Mo-9Si-8B (HIP)	0	-	-	0.1	-	-	8.0	-	[17]
Mo-9Si-8B-1Ti (HIP)	0	-	0.2	1.1	-	-	-	-	[17]
Mo-9Si-8B-1Zr (HIP)	0	-	0.4	0.6	-	-	8.0	-	[17]
Mo-8.9Si-7.7B (GA)	0	-	0	-	-	0	-	7.5	[46]

* Test interrupted

Table A.6: Results of creep tests and literature creep data for PM Mo-Si-B-X alloys and CMSX-4.

Alloy at.%	Temperature °C	Stress MPa	minimum/ steady-state creep rate, $\frac{1}{s}$	Ref.
Mo-40V-9Si-8B (FAST)	1093	50	$1.05 \cdot 10^{-6}$	-
		80	$3.36 \cdot 10^{-6}$	
		100	$8.57 \cdot 10^{-6}$	
		150	$2.23 \cdot 10^{-5}$	
		200	$3.97 \cdot 10^{-5}$	
Mo-40V-9Si-8B (FAST+TT)	1093	50	$7.32 \cdot 10^{-8}$	-
		100	$2.28 \cdot 10^{-7}$	
		150	$5.05 \cdot 10^{-7}$	
		200	$1.12 \cdot 10^{-6}$	
Mo-9Si-8B (FAST)	1093	50	$4.05 \cdot 10^{-7}$	[99]
		100	$2.16 \cdot 10^{-6}$	
		200	$3.67 \cdot 10^{-6}$	
		300	$6.42 \cdot 10^{-6}$	
Mo-9Si-8B-1Zr (HIP)	1093	75	$1.38 \cdot 10^{-8}$	[70]
		150	$1.60 \cdot 10^{-7}$	
		300	$6.42 \cdot 10^{-6}$	
Mo-2.7Nb-8.9Si-7.7B (HIP)	1093	150	$1.90 \cdot 10^{-7}$	[21]
		200	$3.70 \cdot 10^{-7}$	
		300	$7.80 \cdot 10^{-7}$	
CMSX-4	1093	75	$1.18 \cdot 10^{-8}$	[99, 188]
		150	$3.09 \cdot 10^{-7}$	
		200	$1.30 \cdot 10^{-6}$	

Table A.7: Results of creep tests and literature creep data for solidified Mo-Si-B-X alloys and CMSX-4.

Alloy at.%	Temperature °C	Stress MPa	minimum/ steady-state creep rate, $\frac{1}{s}$	Ref.
Mo-40V-9Si-8B (Arc)	1093	80	$1.29 \cdot 10^{-8}$	-
		100	$3.30 \cdot 10^{-8}$	
		150	$5.71 \cdot 10^{-8}$	
		200	$1.27 \cdot 10^{-7}$	
Mo-9Si-8B-29Ti (Arc)	1200	100	$1.10 \cdot 10^{-8}$	[105]
		200	$8.00 \cdot 10^{-8}$	
		300	$2.00 \cdot 10^{-7}$	
Mo-17.5Si-8B (DS)	1093	100	$6.19 \cdot 10^{-10}$	[187]
		150	$4.88 \cdot 10^{-9}$	
		200	$1.54 \cdot 10^{-8}$	
		300	$4.35 \cdot 10^{-8}$	
Mo-5Si-10B-7.5TiC (Arc+TT)	1400	137	$3.00 \cdot 10^{-7}$	[189, 190]
		170	$6.00 \cdot 10^{-7}$	
		200	$8.00 \cdot 10^{-7}$	
		250	$1.80 \cdot 10^{-6}$	
		300	$2.30 \cdot 10^{-6}$	

References

[1] J.H. Perepezko. Materials Science. The Hotter the Engine, the Better. *Science*, 326(5956):1068–1069, 2009.

[2] Take a Look Under the Hood of the GP7200. https://www.enginealliance.com/gp7200/, april 2019.

[3] W. Smarsly. Werkstoffe für Luftfahrtantriebe - Status und zukünftige Perspektiven. In *Symposium 30 Jahre GWP Gesellschaft für Werkstoffprüfung mbh*, 2007.

[4] G. Cerbe and G. Wilhelms. *Technische Thermodynamik - Theoretische Grundlagen und praktische Anwendungen*. Carl Hanser Verlag München, 2008.

[5] G.L. Erickson. The Development of the CMSX® -11B and CMSX® -11C Alloys for Industrial Gas Turbine Application. *Superalloys*, pages 45–52, 1996.

[6] Y. Koizumi, T. Kobayashi, T. Yokokawa, J. Zhang, M. Osawa, H. Harada, Y. Aoki, and M. Arai. Development of Next-Generation Ni-Base Single Crystal Superalloys. *Superalloys*, pages 35–43, 2004.

[7] J.E. Jackson, D.L. Olson, B. Mishra, and A.N. Lasseigne-Jackson. Deposition and characterization of Al-Si metallic TBC precursor on Mo-Si-B turbine materials. *International Journal of Hydrogen Energy*, 32:3789–3796, 2007.

[8] A.P. Alur, N. Chollacoop, and K.S. Kumar. Creep effects on crack growth in a Mo-Si-B alloy. *Acta Materialia*, 55(3):961–974, 2007.

[9] K. Yoshimi, S. Nakatani, N. Nomura, and S. Hanada. Thermal expansion, strength and oxidation resistance of Mo/Mo_5SiB_2 in-situ composites at elevated temperatures. *Intermetallics*, 11(8):787–794, 2003.

[10] J. Cheng, S. Yi, and J.S. Park. Oxidation behaviors of Nb-Si-B ternary alloys at 1100 °C under ambient atmosphere. *Intermetallics*, 23:12–19, 2012.

[11] F. Gang, A. Kauffmann, and M. Heilmaier. Oxidation behaviors of Nb-Si-B ternary alloys at 1100 °C under ambient atmosphere. *Metallurgical and Materials Transactions A*, 49(3):763–771, 2018.

[12] A.A.A. Pinto da Silva, N. Chaia, F. Ferreira, G. Carvalho Coelho, J.M. Fiorani, N. David, M. Vilasi, and C.A. Nunes. Thermodynamic modeling of the V-Si-B system. *Calphad*, 59:199–206, 2017.

[13] M. Krüger. High temperature compression strength and oxidation of a V-9Si-13B alloy. *Scipta Materialia*, 121:75–78, 2016.

[14] R. Fleischer. High-Temperature, High-Strength Materials - An Overview. *Journal of Metals*, 37(12):16–20, 1985.

[15] R. Bürgel, H.J. Maier, and T. Niendorf. *Handbuch Hochtemperatur-Werkstofftechnik*. Vieweg+Teubner Verlag; Springer Fachmedien Wiesbaden GmbH, 2011.

[16] P. Enghag. *Encyclopedia of the Elements: Technical Data-History-Processing-Applications*. WILEY-VCH Verlag GmbH & Co. KGaA, 2004.

[17] M. Krüger. *Dissertation: Pulvermetallurgische Herstellung und Charakterisierung von oxidationsbeständigen Molybdänbasislegierungen für Hochtemperaturanwendungen*. Logos Verlag Berlin, 2010.

[18] W.O. Soboyejo and T.S. Srivatsan. *Advanced Structural Materials: Properties, Design Optimization, and Applications*. CRC Press,Taylor & Francis Group, 2006.

[19] D.M. Berczik. Improved oxidation resistant molybdenum alloy, 1997. United States Patent 5.693.156.

[20] D.M. Berczik. Method for enhancing the oxidation resistance of molybdenum alloy, and a method of making a molybdenum alloy, 1997. United States Patent 5.595.616.

[21] P. Jéhanno, M. Heilmaier, H. Saage, M. Böning, H. Kestler, J. Freudenberger, and S. Drawin. Assessment of the high temperature deformation behavior of molybdenum silicide alloys. *Materials Science and Engineering A*, 463:216–223, 2007.

[22] G. Hasemann, I. Bogomol, D. Schliephake, P.I. Loboda, and M. Krüger. Microstructure and creep properties of a near-eutectic directionally solidified multiphase Mo-Si-B alloy. *Intermetallics*, 48:28–33, 2014.

[23] T.A. Parthasarathy, M.G. Mendiratta, and D.M. Dimiduk. Oxidation mechanisms in Mo-reinforced Mo_5SiB_2(T2)-Mo_3Si alloys. *Acta Materialia*, 50:1857–1868, 2002.

[24] M.G. Mendiratta, T.A. Parthasarathy, and D.M. Dimiduk. Oxidation behavior of αMo-Mo_3Si-Mo_5SiB_2 (T2) three phase system. *Intermetallics*, 10(3):225–232, 2002.

[25] K.-I. Takagi and Y. Yamasaki. Effects of Mo/B Atomic Ratio on the Mechanical Properties and Structure of Mo_2NiB_2 Boride Base Cermets with Cr and V Additions. *Journal of Solid State Chemistry*, 154(1):263–268, 2000.

[26] X.Y. Chong, X.Y. Jiang, R. Zhou, and J. Feng. Stability, chemical bonding behavior, elastic properties and lattice thermal conductivity of molybdenum and tungsten borides under hydrostatic pressure. *Ceramics International*, 42:2117–2132, 2016.

[27] M. Zhang, H. Yan, Q. Wei, and H. Wang. Pressure-induced phase transition and mechanical properties of molybdenum diboride: First principles calculations. *Journal of Applied Physics*, 112(1):013522–1–013522–7, 2012.

[28] D. Sturm, M. Heilmaier, J.H. Schneibel, P. Jéhanno, B. Skrotzki, and H. Saage. The influence of silicon on the strength and fracture toughness of molybdenum. *Materials Science and Engineering A*, 463:107–114, 2007.

[29] H. Saage, M. Krüger, D. Sturm, M. Heilmaier, J.H. Schneibel, L. George, E.and Heatherly, Ch. Somsen, G. Eggeler, and Y. Yang. Ductilization of Mo-Si solid solutions manufactured by powder metallurgy. *Acta Materialia*, 57:3895–3901, 2009.

[30] H. Nowotny, E. Dimakopoulou, and H. Kudielka. Untersuchungen in den Dreistoff-systemen: Molybdän-Silizium-Bor, Wolfram-Silizium-Bor und in dem System: VSi_2–$TaSi_2$. *Monatshefte für Chemie*, 88:180–192, 1957.

[31] R. Sakidja and J.H. Perepezko. Phase stability and alloying behavior in the Mo-Si-B system. *Metallurgical and Materials Transactions A*, 36(3):507–514, 2005.

[32] R. Sakidja, J.H. Perepezko, S. Kim, and N. Sekido. Phase stability and structural defects in high-temperature Mo-Si-B alloys. *Acta Materialia*, 56:5223–5244, 2008.

[33] S.H. Ha, K. Yoshimi, K. Maruyama, R. Tu, and T. Goto. Compositional regions of single phases at $1800\,°C$ in Mo-rich Mo-Si-B ternary system. *Materials Science and Engineering A*, 552:179–188, 2012.

[34] M. Meyer, M.J. Kramer, and M. Akinc. Boron-doped molybdenum silicides. *Advanced Materials*, 8(1):85–88, 1996.

[35] M.K. Meyer and M. Akinc. Isothermal Oxidation Behavior of Mo-Si-B Intermetallics at $1450\,°C$. *Journal of the American Ceramic Society*, 79(10):2763–2766, 1996.

[36] M.K. Meyer, M.J. Kramer, and M. Akinc. Compressive creep behavior of Mo_5Si_3 with the addition of boron. *Intermetallics*, 4:273–281, 1996.

[37] M.K. Meyer, A.J. Thom, and M. Akinc. Oxide scale formation and isothermal oxidation behavior of Mo-Si-B intermetallics at 600–$1000\,°C$. *Intermetallics*, 7(2):153–162, 1999.

[38] M. Akinc, M.K. Meyer, M.J. Kramer, A.J. Thom, J.J. Huebsch, and B. Cook. Boron-doped molybdenum silicides for structural applications. *Materials Science and Engineering A*, 261:16–23, 1999.

[39] P. Mandal, A.J. Thom, M.J. Kramer, V. Behrani, and M. Akinc. Oxidation behavior of Mo-Si-B alloys in wet air. *Materials Science and Engineering A*, 371(1):335–342, 2004.

[40] J. Perepezko, R. Sakidja, and S. Kim. Phase Stability in Processing and Microstructure Control in High Temperature Mo-Si-B Alloys. *Materials Research Society Proceedings*, 646:N4.5.1–N4.5.12, 2001.

[41] R. Mitra. Mechanical behaviour and oxidation resistance of structural silicides. *International Materials Reviews*, 51(1):13–64, 2006.

[42] J.H. Schneibel, C.T. Liu, D.S. Easton, and C.A. Carmichael. Microstructure and mechanical properties of Mo-Mo$_3$Si-Mo$_5$SiB$_2$ silicides. *Materials Science and Engineering A*, 261:78–83, 1999.

[43] J.H. Schneibel, R.O. Ritchie, J.J. Kruzic, and P.F. Tortorelli. Optimizaton of Mo-Si-B Intermetallic Alloys. *Metallurgical and Materials Transactions A*, 36A:525–531, 2005.

[44] J. Becker and M. Krüger. Impact of Phase Distribution on the Fracture Toughness of High Temperature Resistant Mo-Si-B Alloys. *Practical Metallography*, 52(6):295–313, 2015.

[45] J.H. Schneibel, J.J. Kruzic, and R.O. Ritchie. Mo-Si-B Alloy Development. *Proceedings of the 17th Annual Conference on Fossil Energy Materials 2003 (Baltimore, Maryland)*, 2003.

[46] P. Jéhanno, M. Heilmaier, and H. Kestler. Characterization of an industrially processed Mo-based silicide alloy. *Intermetallics*, 12:1005–1009, 2004.

[47] K. Ito, K. Ihara, K. Tanaka, M. Fujikura, and M. Yamaguchi. Physical and mechanical properties of single crystals of the T$_2$ phase in the Mo-Si-B system. *Intermetallics*, 9:591–602, 2001.

[48] H. Choe, D. Chen, J.H. Schneibel, and R.O. Ritchie. Ambient to high temperature fracture toughness and fatigue-crack propagation behavior in a Mo-12Si-8.5B (at.%) intermetallic. *Intermetallics*, 9:319–329, 2001.

[49] I. Rosales and J.H. Schneibel. Stoichiometry and mechanical properties of Mo$_3$Si. *Intermetallics*, 8:885–889, 2000.

[50] K. Ihara, K. Ito, K. Tanaka, and M. Yamaguchi. Mechanical properties of Mo$_5$SiB$_2$ single crystals. *Materials Science and Engineering A*, 329–331:222–227, 2002.

[51] D.M. Dimiduk and J.H. Perepezko. Mo-Si-B Alloys: Developing a Revolutionary Turbine-Engine Material. *MRS Bulletin*, 28:639–645, 2003.

[52] P. Jéhanno, M. Heilmaier, H. Kestler, M. Böning, A. Venskutonis, B. Bewlay, and M. Jackson. Assessment of a powder metallurgical processing route for refractory metal silicide alloys. *Metallurgical and Materials Transactions A*, 36(3):515–523, 2005.

[53] Edmund Bühler GmbH. Kompakter Lichtbogenofen MAM-1. https://www.edmund-buehler.de/de/materialtechnik/lichtbogenschmelzen/kompakter-lichtbogenofen-mam-1/, april 2019.

[54] J.H. Schneibel. High temperature strength of Mo-Mo$_3$Si-Mo$_5$SiB$_2$ molybdenum silicides. *Intermetallics*, 11(7):625–632, 2003.

[55] J.H. Schneibel, M.J. Kramer, Ö. Ünal, and R.N. Wright. Processing and mechanical properties of a molybdenum silicide with the composition Mo-12Si-8.5B (at.%). *Intermetallics*, 9:25–31, 2001.

[56] G. Hasemann, D. Kaplunenko, I. Bogomol, and M. Krüger. Near-Eutectic Ternary Mo-Si-B Alloys: Microstructures and Creep Properties. *JOM*, 68(11):2847–2853, 2016.

[57] M. Krüger, S. Franz, H. Saage, M. Heilmaier, J.H. Schneibel, P. Jéhanno, M. Böning, and H. Kestler. Mechanically alloyed Mo-Si-B alloys with a continuous α-Mo matrix and improved mechanical properties. *Intermetallics*, 16(7):933–941, 2008.

[58] J. Schmelzer, S.-K. Rittinghaus, A. Weisheit, M. Stobik, J. Paulus, K. Gruber, E. Wessel, C. Heinze, and M. Krüger. Printability of gas atomized Mo-Si-B powders by laser metal deposition. *International Journal of Refractory Metals and Hard Materials*, 78:123–126, 2019.

[59] D.P. Manson, D.C. Van Aken, and J.F. Mansfield. On the microstructure and crystallography of directionally solidified MoSi$_2$-Mo$_5$Si$_3$ eutectics. *Acta Metallurgica et Materialia*, 43(3):1189–1199, 1995.

[60] D.P. Manson and D.C. Van Aken. On the creep of directionally solidified MoSi$_2$-Mo$_5$Si$_3$ eutectics. *Acta Metallurgica et Materialia*, 43(3):1201–1210, 1995.

[61] K. Ito, M. Kumagai, T. Hayashi, and M. Yamaguchi. Room temperature fracture toughness and high temperature strength of T2/Mo$_{ss}$ and (Mo,Nb)$_{ss}$/T1/T2 eutectic alloys in the Mo-Si-B system. *Scripta Materialia*, 49(4):285–290, 2003.

[62] F. Wang, A. Shan, X. Dong, and J. Wu. Microstructure and oxidation behavior of directionally solidified Mo-Mo$_5$SiB$_2$ (T2)-Mo$_3$Si alloys. *Journal of Alloys and Compounds*, 462(1):436–441, 2008.

[63] M. Krüger, H. Saage, M. Heilmaier, P. Jéhanno, M. Böning, H. Kestler, V. Shyrska, A. Dudka, and P. Loboda. Influence of Processing on the Microstructure and Mechan-

ical Properties of Mo-Si-B Alloys. *Proceedings 17th Plansee Seminar*, 4(RM80):1–9, 2009.

[64] M. Krüger, G. Hasemann, I. Bogomol, and P.I. Loboda. Multiphase Mo-Si-B alloys processed by diractional soldification. *Materials Research Society Symposium Proceeding*, 1516:303–308, 2012.

[65] W. Schatt, K.-P. Wieters, and B. Kieback. *Pulvermetallurgie: Technologien und Werkstoffe.* Springer-Verlag Berlin, Heidelberg, 2007.

[66] O. Hassomeris, G. Schumacher, M. Krüger, M. Heilmaier, and J. Banhart. Phase Continuity in High Temperature Mo-Si-B Alloys: A FIB-Tomography Study. *Intermetallics*, 19(4):470–475, 2011.

[67] M. Heilmaier, M. Krüger, H. Saage, J. Rösler, D. Mukherji, U. Glatzel, R. Völkl, R. Hüttner, G. Eggeler, Ch. Somsen, T. Depka, H. Christ, B. Gorr, and S. Burk. Metallic Materials for Structural Applications Beyond Nickel-based Superalloys. *JOM*, 61(7):61–67, 2009.

[68] J.H. Schneibel, M.J. Kramer, and D.S. Easton. A Mo-Si-B intermetallic alloy with a continuous α-Mo matrix. *Scripta Materialia*, 46:217–221, 2002.

[69] J.J. Kruzic, J.H. Schneibel, and R.O. Ritchie. Fracture and fatigue resistance of Mo-Si-B alloys for ultrahigh-temperature structural applications. *JOM*, 50(4):459–464, 2004.

[70] M. Krüger, D. Schliephake, P. Jain, K.S. Kumar, G. Schumacher, and M. Heilmaier. Effects of Zr Additions on the Microstructure and the Mechanical Behavior of PM Mo-Si-B Alloys. *JOM*, 65(2):301–306, 2013.

[71] A. Kumar, B.L. Eyre, and J.W. Christian. Grain boundary segregation and intergranular fracture in molybdenum. *Proceedings of the Royal Society A: Mathematical, Physical and Engineering Sciences*, 370(1743):431–458, 1980.

[72] K. Hagihara, T. Nakano, M. Suzuki, T. Ishimoto, Suyalatu, and S.-H. Sun. Successful additive manufacturing of $MoSi_2$ including crystallographic texture and shape control. *Journal of Alloys and Compounds*, 696:67–72, 2017.

[73] S.K. Makineni, A.R. Kini, E.A. Jägle, H. Springer, D. Raabe, and B. Gault. Synthesis and stabilization of a new phase regime in a Mo-Si-B based alloy by laser-based additive manufacturing. *Acta Materialia*, 151:31–40, 2018.

[74] L. Northcott. *Metallurgy of the rarer Metals - 5: Molybdenum.* Academic Press Incorporation, New York, 1956.

[75] P.G. Gonzales-Ormeño, H.M. Petrilli, and C.G. Schön. Ab initio calculation of the

bcc Mo-Al (molybdenum-aluminium) phase diagram: Implications for the nature of the ζ_2-MoAl phase. *Scripta Materialia*, 53:751–756, 2005.

[76] N. Sodré, P.G. Gonzales-Ormeño, H.M. Petrilli, and C.G. Schön. Ab initio calculation of the BCC Fe-Al-Mo (Iron-Aluminum-Molybdenum) phase diagram: Implications for the nature of the tau(2) phase. *CALPHAD*, 33:576–583, 2009.

[77] H. Czichos. *Hütte: Die Grundlagen der Ingenieurwissenschaften.* Springer-Verlag Berlin Heidelberg, 1996.

[78] B. Predel. *Landolt-Börnstein - Group IV Physical Chemistry (Numerical Data and Functional Relationships in Science and Technology).* Springer-Verlag Berlin, Heidelberg, 1994.

[79] ASM Iinternational. *ASM Handbook Volume 3: Alloy Phase Diagrams.* Materials Park, 1992.

[80] J. Rösler, H. Harders, and M. Bäker. *Mechanisches Verhalten der Werkstoffe.* Vieweg+Teubner GWV Fachverlage GmbH, Wiesbaden, 2008.

[81] C.B. Geller, R.W. Smith, J.E. Hack, P. Saxe, and E. Wimmer. A computational search for ductilizing additives to Mo. *Scripta Materialia*, 52:205–210, 2005.

[82] O. Lenchuk, J. Rohrer, and K. Albe. Atomistic modelling of zirconium and silicon segregation at twist and tilt grain boundaries in molybdenum. *Journal of Materials Science*, 51:1873–1881, 2016.

[83] M. Mousa, N. Wanderka, M. Timpel, S. Singh, M. Krüger, M. Heilmaier, and J. Banhart. Modification of Mo-Si alloy microstructure by small additions of Zr. *Ultramicroscopy*, 111:706–710, 2011.

[84] C. Cui, Y. Gao, S. Wei, G. Zhang, Y. Zhou, and X. Zhu. Microstructure and high temperature deformation behavior of the Mo-ZrO$_2$ alloys. *Journal of Alloys and Compounds*, 716:321–329, 2017.

[85] O. Lenchuk, J. Rohrer, and K. Albe. Cohesive strength of zirconia/molybdenum interfaces and grain boundaries in molybdenum: A comparative study. *Acta Materialia*, 135:150–157, 2017.

[86] FactSage 7.2: Documentation - summary of databases - SGTE(2017) alloy database - Calculated Phase Diagrams: Mo-V. http://www.crct.polymtl.ca/fact/documentation/, august 2019.

[87] J. Fan, M. Lu, H. Cheng, J. Tian, and B. Huang. Effect of alloying elements Ti, Zr on the property and microstructure of molybdenum. *International Journal of Refractory Metals and Hard Materials*, 27:78–82, 2009.

[88] L.E. Olds and G.W.P. Rengstorff. Effect of small amounts of alloying elements on the ductility of cast molybdenum. *JOM*, 9(4):468–471, 1957.

[89] Y. Hiraoka, S. Yoshimura, and K. Takebe. Effects of complex additions of Re or Ti with C on the strength and ductility of recrystallized molybdenum. *International Journal of Refractory Metals and Hard Materials*, 12:261–268, 1993.

[90] Y. Hiraoka, S. Yoshimura, and K. Takebe. Low-temperature tensile behavior of powder-metallurgy Mo-Ti alloys. *International Journal of Refractory Metals and Hard Materials*, 12:211–216, 1994.

[91] T. Inoue, Y. Hiraoka, E. Sukedai, M. Nagae, and J. Takada. Hardening behavior of dilute Mo-Ti alloys by two-step heat-treatment. *International Journal of Refractory Metals and Hard Materials*, 25:138–143, 2007.

[92] Y. Hiraoka, M. Okada, and H. Irie. Alloying to improve the properties of welded molybdenum. *Journal of Nuclear Materials*, 155–157:381–385, 1988.

[93] G. Hasemann, C. Müller, D. Grüner, E. Wessel, and M. Krüger. Room temperature plastic deformability in V-rich V-Si-B alloys. *Acta Materialia*, 175:140–147, 2019.

[94] J.H. Schneibel. Mo-Si-B Alloy Development. *Oak Ridge National Laboratory, Metals and Ceramics Division*, 2003.

[95] V. Behrani, A.J. Thom, M.J. Kramer, and M. Akinc. Microstructure and oxidation behavior of Nb-Mo-Si-B alloys. *Intermetallics*, 14:24–32, 2006.

[96] D. Schliephake, M. Azim, K. v. Klinski-Wetzel, B. Gorr, H.-J. Christ, H. Bei, E.P. George, and M. Heilmaier. High-Temperature Creep and Oxidation Behavior of Mo-Si-B Alloys with High Ti Contents. *Metallurgical and Materials Transactions A*, 45A:1102–1111, 2014.

[97] S. Burk, B. Gorr, M. Krüger, M. Heilmaier, and H.-J. Christ. Oxidation Behavior of Mo-Si-B-(X) Alloys: Macro- and Microalloying (X = Cr, Zr, La$_2$O$_3$). *JOM*, 63(12):32–36, 2011.

[98] R. Sakidja and J.H. Perepezko. Alloying and microstructure stability in the high-temperature Mo-Si-B system. *Journal of Nuclear Materials*, 366:407–416, 2007.

[99] J. Becker, U. Betke, M. Hoffmeister, and M. Krüger. Density Reduction of Mo-Si-B Alloys by Vanadium Alloying. *JOM*, 70:2574–2581, 2018.

[100] C. Hochmuth, D. Schliephake, R. Völkl, M. Heilmaier, and U. Glatzel. Influence of zirconium content on microstructure and creep properties of Mo-9Si-8B alloys. *Intermetallics*, 48:3–9, 2014.

[101] M. Krüger, H. Saage, M. Heilmaier, P. Jain, and K.S. Kumar. Effect of Zr additions on the deformation and fracture behaviour of three phase Mo-Si-B alloys. *Non-linear response of conventional and advanced materials, and multi-scale modeling*, pages 268–270, 2012.

[102] Y. Yang, H. Bei, S. Chen, E.P. George, J. Tiley, and Y.A. Chang. Effects of Ti, Zr, and Hf on the phase stability of $Mo_{ss} + Mo_3Si + Mo_5SiB_2$ alloys at 1600 °C. *Acta Materialia*, 58(2):541–548, 2010.

[103] M. Krüger, O. Kauss, K. Naumenko, C. Burmeister, E. Wessel, and J. Schmelzer. The potential of mechanical alloying to improve the strength and ductility of Mo-9Si-8B-1Zr alloys - experiments and simulation. *Intermetallics*, 113:106558, 2019.

[104] S. Burk, B. Gorr, H.J. Christ, D. Schliephake, M. Heilmaier, C. Hochmuth, and U. Glatzel. High-temperature oxidation behaviour of a single-phase $(Mo,Ti)_5Si_3$ (Mo-Si-Ti) alloy. *Scripta Materialia*, 66:223–226, 2012.

[105] M.A. Azim, D. Schliephake, C. Hochmuth, B. Gorr, H.-J. Christ, U. Glatzel, and M. Heilmaier. Creep Resistance and Oxidation Behavior of Novel Mo-Si-B-Ti Alloys. *JOM*, 67:2621–2628, 2015.

[106] D. Schliephake, M. Heilmaier, M. Azim, B. Gorr, and H.-J. Christ. Neuartige Mo-Si-B-Ti Legierungen für den Hochtemperatureinsatz. *Werkstoffkolloquium 2013 - Leichtbauwerkstoffe für das Triebwerk von Morgen DLR Köln*, 2014.

[107] G. Gottstein. *Physikalische Grundlagen der Materialkunde, 3. Auflage*. Springer-Verlag Berlin, Heidelberg, 2007.

[108] J.B. Brosse, R. Fillit, and M. Biscondi. Intrinsic intergranular brittleness of molybdenum. *Scripta Metallurgica*, 15(6):619–623, 1981.

[109] H.-J. Bargel. *Werkstoffkunde, 10. Auflage*. Springer-Verlag Berlin, Heidelberg, 2008.

[110] W. Cai and W.D. Nix. *Imperfections in Crystalline Solids*. Cambridge University Press, 2016.

[111] M. Krüger, J. Schmelzer, and M. Helmecke. Similarities and Differences in Mechanical Alloying Processes of V-Si-B and Mo-Si-B Powders. *Metals*, 241(6):1–16, 2016.

[112] M. Krüger, P. Jain, K.S. Kumar, and M. Heilmaier. Correlation between microstructure and properties of fine grained $Mo-Mo_3Si-Mo_5SiB_2$ alloys. *Intermetallics*, 48:10–18, 2014.

[113] T. Takida, H. Kurishita, M. Mabuchi, T. Igarashi, Y. Doi, and T. Nagae. Mechanical Properties of Fine-Grained, Sintered Molybdenum Alloys with Dispersed Particles Developed by Mechanical Alloying. *Materials Transactions*, 45:143–148, 2004.

[114] L. Liu, C. Sun, C. Zhang, P.M. Voyles, J. Fournelle, A. Handt, and J.H. Perepezko. Examination of B in the Mo solid solution (Mo_{ss}) in Mo_{ss} + Mo_5SiB_2 + Mo_2B alloys. *Scripta Materialia*, 163:62–65, 2019.

[115] R.L. Fleischer. Substitutional solution hardening. *Acta Metallurgica*, 11(3):203–209, 1963.

[116] R. Labusch. A Statistical Theory of Solid Solution Hardening. *Physica Status Solidi (b)*, 41:659–669, 1970.

[117] O. Vöhringer. *Die strukturmechanischen Grundlagen der plastischen Verformung von vielkristallinen α-Kupfer-Legierungen.* Habilitationsschrift an der Universität Karlsruhe, 1972.

[118] C. Woodward and S.I. Rao. Flexible Ab Initio Boundary Conditions: Simulating Isolated Dislocations in bcc Mo and Ta. *Physical Review Letters*, 88(21):216402–1–216402–4, 2002.

[119] W. Xu and J.A. Moriarty. Accurate atomstic simulations of the Peierls barrier and kink-pair formation energy for $\langle 111 \rangle$ screw dislocations in bcc Mo. *Computational Materials Science*, 9:348–356, 1998.

[120] S. Ismail-Beigi and T.A. Arias. Ab Initio Study of Screw Dislocations in Mo and Ta: A New Picture of Plasticity in bcc Transition Metals. *Physical Review Letters*, 84(7):1499–1502, 2000.

[121] E.O. Hall. The Deformation and Ageing of Mild Steel: III Discussion of Results. *Proceedings of the Physical Society - Section B*, 64(9):747–753, 1951.

[122] N.J. Petch. The Cleavage Strength of Polycrystals. *Journal of the Iron and Steel Institute*, 174:25–28, 1953.

[123] H. Stroppe. *Physik - für Studierende der Natur- und Ingenieurwissenschaften.* Carl Hanser Verlag München, 2008.

[124] P. Jain and K.S. Kumar. Tensile creep of Mo-Si-B alloys. *Acta Materialia*, 58:2124–2142, 2010.

[125] V. Bolbut. *Dissertation: Development of Mo-Hf-B and Mo-Zr-B alloys for high-temperature application.* Magdeburg, 2018.

[126] K. Yoshimi, S. Nakatani, T. Suda, S. Hanada, and H. Habazaki. Oxidation behavior of Mo_5SiB_2-based alloy at elevated temperatures. *Intermetallics*, 10:407–414, 2002.

[127] M.R. Middlemas. *Dissertation: Fabrication, Strength and Oxidation of Molybdenum-Silicon-Boron Alloys from Reaction Synthesis.* Proquest, 2011.

[128] J.H. Perepezko and R. Sakidja. Oxidation Resistant Coatings for Ultrahigh Temperature Refractory Mo-Base Alloys. *Advanced Engineering Materials*, 11(11):892–897, 2009.

[129] G. Bauer, V. Güther, H. Hess, A. Otto, O. Roidl, H. Roller, S. Sattelberger, S. Köther-Becker, and Th. Beyer. *Ullmann's Encyclopedia of Industrial Chemistry - Vanadium and Vanadium Compounds*. Wiley-VCH Verlag GmbH & Co. KGaA, Weinheim, 2016.

[130] A. Mekki, G.D. Khattak, D. Holland, M. Chinkhota, and L.E. Wenger. Structure and magnetic properties of vanadium-sodium silicate glasses. *Journal of Non-Crystalline Solids*, 318(1):193–201, 2003.

[131] N.S. Vedeanu, I.B. Cozar, R. Stanescu, R. Stefan, D. Vodnar, and O. Cozar. Structural investigation of V_2O_5-P_2O_5-K_2O glass system with antibacterial potential. *Bulletin of Materials Science*, 39(3):697–702, 2016.

[132] J. Williams and M. Akinc. Oxidation behavior of V_5Si_3 based materials. *Intermetallics*, 6(4):269–275, 1998.

[133] M.F. Pércio, S.D. de Campos, R. Schneider, and E.A. de Campos. Effect of the addition of TiO_2, ZrO_2, V_2O_5 and Nb_2O_5 on the stability parameters of the Li_2O-BaO-SiO_2 glass. *Journal of Non-Crystalline Solids*, 411:125–131, 2015.

[134] T. Sossaman and J.H. Perepezko. Viscosity control of borosilica by Fe doping in Mo-Si-B environmentally resistant alloys. *Corrosion Science*, 98:406–416, 2015.

[135] N.K. Kumar, B. Roy, R. Mitra, and J. Das. Improvement of oxidation resistance of arc-melted $Mo_{76}Si_{14}B_{10}$ by microstructure control upon minor Fe addition. *Intermetallics*, 88:28–30, 2017.

[136] E. Riedel. *Anorganische Chemie*. Berlin; New York: W. de Gruyter, 2004.

[137] M. Stieß. *Mechanische Verfahrenstechnik 2*. Springer-Verlag Berlin Heidelberg, New York, 1997.

[138] O. Guillon, J. Gonzalez-Julian, B. Dargatz, T. Kessel, G. Schierning, J. Räthel, and M. Herrmann. Field-assisted sintering technology/spark plasma sintering: Mechanisms, materials, and technology developments. *Advanced Engineering Materials*, 16(7):830–849, 2014.

[139] J.P. Eberhart. *Structural and Chemical Analysis of Materials*. John Wiley & Sons Ltd., Chichester, 1991.

[140] J.I. Goldstein, D.E. Newbury, J.R. Michael, N.W.M. Ritchie, J.H.J. Scott, and D.C.

Joy. *Scanning Electron Microscopy and X-Ray Microanalysis*, volume 4. Springer, New York, NY, 2003.

[141] A.J. Schwartz, M. Kumar, B.L. Adams, and D.P. Field. *Electron Backscatter Diffraction in Materials Science.* Springer US, 2009.

[142] DIN EN ISO 643: Stahl - Mikrophotographische Bestimmung der scheinbaren Korngröße, 2017.

[143] L. Spieß, G. Teichert, R. Schwarzer, H. Behnken, and C. Genzel. *Moderne Röntgenbeugung.* Springer Verlag, Wiesbaden, 2014.

[144] E. Engel and R.M. Dreizler. *Density Functional Theory.* Springer Verlag Berlin Heidelberg, 2011.

[145] J. VandeVondele, M. Krack, F. Mohamed, M. Parrinello, T. Chassaing, and J. Hutter. Quickstep: Fast and accurate density functional calculations using a mixed Gaussian and plane waves approach. *Computer Physics Communications*, 167:103–128, 2005.

[146] J. Hutter, M. Iannuzzi, F. Schiffmann, and J. VandeVondele. CP2K: atomistic simulations of condensed matter systems. *Wiley Interdisciplinary Reviews: Computational Molecular Science*, 4(1):15–25, 2014.

[147] G. Lippert, J. Hutter, and M. Parrinello. A hybrid Gaussian and plane wave density functional scheme. *Molecular Physics*, 92(3):477–488, 1997.

[148] J. VandeVondele and J. Hutter. Gaussian basis sets for accurate calculations on molecular systems in gas and condensed phases. *The Journal of Chemical Physics*, 127(11):114105, 2007.

[149] S. Goedecker, M. Teter, and J. Hutter. Separable dual-space Gaussian pseudopotentials. *Physical Review B*, 54(3):1703–1710, 1996.

[150] C. Hartwigsen, S. Goedecker, and J. Hutter. Relativistic separable dual-space Gaussian pseudopotentials from H to Rn. *Physical Review B*, 58(7):3641–3662, 1998.

[151] M. Krack. Pseudopotentials for H to Kr optimized for gradient-corrected exchange-correlation functionals. *Theoretical Chemistry Accounts*, 114(1):145–152, 2005.

[152] J.P. Perdew, K. Burke, and M. Ernzerhof. Generalized Gradient Approximation Made Simple. *Physical Review Letters*, 77(18):3865–3868, 1996.

[153] O.K. Andersen, H.L. Skriver, H. Nohl, and B. Johansson. Electronic structure of transition metal compounds; ground-state properties of the 3d-monoxides in the atomic sphere approximation. *Pure and Applied Chemistry*, 52(1):93–118, 1980.

[154] O.K. Andersen and O. Jepsen. Explicit, First-Principles Tight-Binding Theory. *Physical Review Letters*, 53(27):2571–2574, 1984.

[155] J.P. Perdew, J.A. Chevary, S.H. Vosko, K.A. Jackson, M.R. Pederson, D.J. Singh, and C. Fiolhais. Atoms, molecules, solids, and surfaces: Applications of the generalized gradient approximation for exchange and correlation. *Physical Review B*, 46(11):6671–6687, 1992.

[156] DIN EN ISO 6507 - 1: Metallische Werkstoffe - Härteprüfung nach Vickers - Teil 1: Prüfverfahren, 2018.

[157] D. Gross and Th. Seelig. *Bruchmechanik - Mit einer Einführung in die Mikromechanik.* Springer-Verlag Berlin Heidelberg, 2011.

[158] DIN EN ISO 23146: Hochleistungskeramik - Prüfverfahren zur Bestimmung der Bruchzähigkeit monolithischer Keramik - Verfahren für Biegeproben mit V-Kerb (SEVNB-Verfahren), 2012.

[159] H. Blumenauer. *Werkstoffprüfung.* VEB Deutscher Verlag für Grundstoffindustrie, Leipzig, 1977.

[160] DIN EN ISO 178: Kunststoffe - Bestimmung der Biegeeigenschaften, 2013.

[161] J. Becker, U. Betke, E. Wessel, and M. Krüger. Alloying effects in Mo-5X $(X = Zr, Ti, V)$ - microstructural modifications and mechanical properties. *Materials Today Communications*, 15:314–321, 2018.

[162] L. Vegard. Die Konstitution der Mischkristalle und die Raumfüllung der Atome. *Zeitschrift für Physik*, 5(1):17–26, 1921.

[163] Ž. Blažina, R. Trojko, and Z. Ban. Metal-metalloid exchange in the $Zr_{1-x}M_xMo_2$ (M $\equiv$; Ge, Si, Al) system. *Journal of the Less Common Metals*, 97:91–98, 1984.

[164] Ž. Blažina, R. Trojko, and Z. Ban. High temperature equilibria in the $Zr_{1-x}Hf_xM_2$, $Zr_{1-x}Ti_xM_2$ and $Hf_{1-x}Ti_xM_2$ (m $\equiv$ MoorW) systems. *Journal of the Less Common Metals*, 83(2):175–183, 1982.

[165] J. Becker, H.F. Siems, and M. Krüger. Effects of Second Phases in Mo-Zr Alloys - A Study on Phase Evolution and Mechanical Properties. *Naumenko, K. and Krüger, M. (eds):Advances in Mechanics of High-Temperature Materials - Advanced Structured Materials*, 117:93–105, 2019.

[166] T. Mrotzek, A. Hoffmann, and U. Martin. Hardening mechanisms and recrystallization behaviour of several molybdenum alloys. *International Journal of Refractory Metals and Hard Materials*, 24(4):298–305, 2006.

[167] C. Colinet and J.-C. Tedenac. First principles calculations of the stability of the T2 and D8$_8$ phases in the V-Si-B system. *Intermetallics*, 50:108–116, 2014.

[168] Diamond - Crystal and Molecular Structure Visualization. http://www.crystalimpact.com/diamond, august 2019.

[169] R.St. Touzani, J. Becker, and M. Krüger. Site preference of V and its influence on the elastic properties in the boride series V$_x$Mo$_{5-x}$SiB$_2$ as studied by first principles density functional theory. *Journal of Alloys and Compounds*, In Press DOI 10.1016/j.jallcom.2019.153041, 11/2019.

[170] J. Nakamura, T. Kaneko, T. Hara, K. Yoshimi, K. Maruyama, H. Katsui, and T. Goto. Site-occupation behavior and solid-solution hardening effect of rhenium in mo$_5$sib$_2$. *Intermetallics*, 53:85–91, 2014.

[171] S. Aryal, M.C. Gao, L. Ouyang, P. Rulis, and W.Y. Ching. Ab initio studies of Mo-based alloys: Mechanical, elastic, and vibrational properties. *Intermetallics*, 38:116–125, 2013.

[172] L. Zhang, K. Pan, W. Du, M. Wang, J. Lin, X. Ni, H. Shang, and J. Sun. Intrinsic brittleness of Mo$_5$SiB$_2$ and alloying effect on ductility studied by first-principles calculations. *Intermetallics*, 50:79–85, 2014.

[173] S. Hütter, G. Hasemann, J. Al-Karawi, M. Krüger, and T. Halle. Prediction of Thermodynamic Properties of Mo-Si-B Alloys from First-Principles Calculations. *Metallurgical and Materials Transactions A*, 49(12):6075–6083, 2018.

[174] H. Kudielka, H. Nowotny, and G. Findeisen. Untersuchungen in den Systemen: V-B, Nb-B, V-B-Si und Ta-B-Si. *Monatshefte für Chemie und verwandte Teile anderer Wissenschaften*, 88(6):1048–1055, 1957.

[175] F. Bertaut and P. Blum. Étude des borures de chrome. *C.R. hebd. Séances Acad. Sci*, 236:1055, 1953.

[176] C.J Rawn, J.H Schneibel, C.M Hoffmann, and C.R Hubbard. The crystal structure and thermal expansion of Mo$_5$SiB$_2$. *Intermetallics*, 9(3):209–216, 2001.

[177] V.L. Deringer, C. Goerens, M. Esters, R. Dronskowski, and B.P.T. Fokwa. Chemical Modeling of Mixed Occupations and Site Preferences in Anisotropic Crystal Structures: Case of Complex Intermetallic Borides. *Inorganic Chemistry*, 51(10):5677–5685, 2012.

[178] C.A. Nunes, R. Sakidja, Z. Dong, and J.H. Perepezko. Liquidus projection for the Mo-rich portion of the Mo-Si-B ternary system. *Intermetallics*, 8(4):327–337, 2000.

[179] R.A. Gaisin, V.M. Imayev, R.A. Shaimardanov, and R.M. Imayev. Structure and

Properties of Mo-9Si-8B Alloy Fabricated by Casting. *Inorganic Materials: Applied Research*, 8(5):750–754, 2017.

[180] A. Lasalmonie. Intermetallics: Why is it so difficult to introduce them in gas turbine engines? *Intermetallics*, 14:1123–1129, 2006.

[181] H. Choe, J.H. Schneibel, and R.O. Ritchie. On the Fracture and Fatigue Properties of Mo-Mo$_3$Si-Mo$_5$SiB$_2$ Refractory Intermetallic Alloys at Ambient to Elevated Temperatures (25 °C to 1300 °C). *Metallurgical and Materials Transactions A*, 34(A):225–239, 2003.

[182] T. Moriyama, K. Yoshimi, M. Zhao, T. Masnou, T. Yokoyama, J. Nakamura, H. Katsui, and T. Goto. Room-temperature fracture toughness of MoSiBTiC alloys. *Intermetallics*, 84:92–102, 2017.

[183] R. Li, B. Li, T. Wang, S. Ren, X. Chen, J. Wang, and G. Zhang. Improved fracture toughness of a Mo-12Si-8.5B-3Zr alloy by grain coarsening and its multiple toughening mechanisms. *Journal of Alloys and Compounds*, 743:716–727, 2018.

[184] S. Nakayama, N. Sekido, S. Uemura, S. Tsurekawa, and K. Yoshimi. Effect of Microstructural Continuity on Room-Temperature Fracture Toughness of ZrC-Added Mo-Si-B Alloys. *Materials Transactions*, 59(4):518–527, 2018.

[185] A. Krug, P. Jéhanno, and H. Kestler. MoSib - Ein intermetallischer Hochtemperatur-in-situ-Komposit für Strukturbauteile. *Plansee Bericht*, 2001.

[186] H.J. Frost and M.F. Ashby. *Deformation mechanism maps: the plasticity and creep of metals and ceramics.* Pergamon Press, Oxford, 1982.

[187] G. Hasemann. *Dissertation: Microstructure and Properties of Near-eutectic Mo-Si-B Alloys for High Temperature Applications.* Shaker Verlag, Aachen, 2017.

[188] M. Heilmaier, M. Krüger, and H. Saage. Recent Advances in the Development of Mechanically Alloyed Mo Silicide Alloys. *Materials Science Forum*, 633–634:549–558, 2010.

[189] S.Y. Kamata, D. Kanekon, Y. Lu, N. Sekido, K. Maruyama, G. Eggeler, and K. Yoshimi. Ultrahigh-temperature tensile creep of TiC-reinforced Mo-Si-B-based alloy. *Scientific Reports*, 8(10487):1–14, 2018.

[190] K. Yoshimi, J. Nakamura, D. Kanekon, S. Yamamoto, K. Maruyama, H. Katsui, and T. Goto. High-Temperature Compressive Properties of TiC-Added Mo-Si-B Alloys. *JOM*, 66(9):1930–1938, 2014.

[191] S. Majumdar, B. Gorr, H.-J. Christ, D. Schliephake, and M. Heilmaier. Oxidation mechanisms of lanthanum-alloyed Mo-Si-B. *Corrosion Science*, 88:360–371, 2014.

[192] R. Karell, J. Kraxner, and M. Chromčíková. Properties of selected zirconia containing silicate glasses. *Ceramics Silikáty*, 50(2):78–82, 2006.

[193] R. Sakidja, F. Rioult, J. Werner, and J.H. Perepezko. Aluminum pack cementation of Mo-Si-B alloys. *Scripta Materialia*, 55(10):903–906, 2006.

[194] D. Schliephake, C. Gombola, A. Kauffmann, M. Heilmaier, and J.H. Perepezko. Enhanced Oxidation Resistance of Mo-Si-B-Ti Alloys by Pack Cementation. *Oxidation of Metals*, 88(3):267–277, 2017.

[195] A. Lange and R. Braun. Magnetron-sputtered oxidation protection coatings for Mo-Si-B alloys. *Corrosion Science*, 84:74–84, 2014.

[196] N. Nomura, T. Suzuki, K. Yoshimi, and S. Hanada. Microstructure and oxidation resistance of a plasma sprayed Mo-Si-B multiphase alloy coating. *Intermetallics*, 11(7):735–742, 2003.

[197] I. Smokovych and M. Scheffler. Polysilazane-Type Coatings on Mo-Si-B Alloys: A Thermodynamic Assessment of the Phase Composition. *Advanced Engineering Materials*, 20(5):1700936, 2018.

[198] I. Smokovych, G. Hasemann, M. Krüger, and M. Scheffler. Polymer derived oxidation barrier coatings for Mo-Si-B alloys. *Journal of the European Ceramic Society*, 37(15):4559–4565, 2017.